Degenerate Fermi gases in higher Bloch bands of a bipartite optical square lattice

Dissertation
zur Erlangung des Doktorgrades
an der Fakultät für Mathematik, Informatik und Naturwissenschaften
Fachbereich Physik
der Universität Hamburg

vorgelegt von
Max Hachmann

Hamburg
2022

Gutachter/innen der Dissertation:	Prof. Dr. Andreas Hemmerich Prof. Dr. Henning Moritz
Datum der Disputation:	03.06.2022
Zusammensetzung der Prüfungskommission:	Prof. Dr. Andreas Hemmerich Prof. Dr. Henning Moritz Prof. Dr. Ludwig Mathey Prof. Dr. Daniela Pfannkuche Dr. Juliette Simonet
Vorsitzender der Prüfungskommission:	Prof. Dr. Ludwig Mathey
Vorsitzender Fach-Promotionsausschusses Physik:	Prof. Dr. Wolfgang J. Parak
Leiter des Fachbereichs Physik:	Prof. Dr. Günter H. W. Sigl
Dekan der Fakultät MIN:	Prof. Dr. Heinrich Graener

Publications

[Hac+21] M. Hachmann et al. "Quantum Degenerate Fermi Gas in an Orbital Optical Lattice". In: *Physical Review Letters* 127.3 (July 2021), p. 033201.

[Nus+20] M. Nuske et al. "Metastable order protected by destructive many-body interference". In: *Physical Review Research* 2.4 (Nov. 2020), p. 043210.

Abstract

Optical lattices present a powerful toolbox for simulating a variety of condensed-matter problems in which neutral atoms moving in periodic light potentials emulate the role of electrons moving in a solid. Since it is possible to tune almost every system parameter over a broad range, this gives rise to approach yet unsolved questions experimentally. An example of this is the ground state phase diagram of the fermionic Hubbard model and its possible significance for high Tc superconductivity. A new aspect explored in this thesis is the combination of using fermionic atoms in an optical lattice with accessible orbital degree of freedom.

This thesis presents the experimental results from the first successful excitation of degenerate Fermi gases into selected higher Bloch bands of a bipartite optical square lattice. After adiabatically loading a degenerate Fermi gas with an initial temperature as low as $0.18\,\mathrm{T_F}$ into a shallow optical lattice, the atoms occupy the fermionic many-body ground state of the system and fill the entire first Bloch band. Extending the established technique, referred to as *population swapping*, to the case of fermionic ensembles enables the successful loading of higher Bloch bands, namely the 2^{nd}, 4^{th} and 7^{th}. Band populations and momentum distributions were recovered using standard methods referred to as band mapping and time-of-flight imaging. The broken rotational symmetry of the momentum distribution thereby directly reveals the orbital character of higher bands.

The lifetime of fermionic samples prepared in the second Bloch band is observed and band index changing processes are identified. In the case of spin polarised and thus non-interacting Fermi gases a lifetime of up to 21 s in the second band is observed. Preparing an interacting two spin component mixture instead yielded lifetimes of 2.6 s and gave valuable insights into interband relaxation processes associated with collisions and heating.

Zusammenfassung

Optische Gitter stellen einen vielseitigen Werkzeugkasten zur Simulation einer Vielzahl von Festkörperproblemen dar, indem sich durch ein periodisches Lichtpotential bewegende neutrale Atome die Rolle von Elektronen in realen Festkörpern imitieren. Die Möglichkeit fast jeden relevanten Systemparameter über einen weiten Bereich verändern und präzise einstellen zu können ermöglicht somit sich bisher unbeantworteten Fragestellungen, wie der Ursache der Hochtemperatursupraleitung, experimentell nähern zu können. Einer dieser veränderbaren Parameter ist der orbitale Freiheitsgrad.

Diese Dissertation präsentiert experimentelle Ergebnisse der erstmalig gelungenen selektiven Anregung von entarteten Fermigasen in höhere Bloch Bänder eines quadratischen optischen Gitters mit zweiatomiger Basis. Nachdem ein entartetes Fermigas mit einer Initialtemperatur von bis zu $0.18\,\mathrm{T_F}$ in ein flaches optisches Gitter geladen wurde besetzen die Atome den fermionischen Mehrteilchengrundzustand und füllen das gesamte erste Bloch band auf. Eine *Populations Transfer* genannte Technik zunächst entwickelt um bosonische Ensemble in höhere Bänder anzuregen konnte dabei erfolgreich auf fermionische Ensemble erweitert werden, sodass ein entartetes Fermigas effizient in das zweite, vierte und siebte Bloch band angeregt werden konnte. Mittels Bandkartografie wird anschließend die Bandbesetzung aufgelöst. Abbildung des atomaren Ensembles nach ballistischer Expansion ermöglicht den orbitalen Freiheitsgrad der präparierten Zustände direkt aufzulösen, welcher sich in der gebrochenen Rotationssymmetrie zeigt.

Die Lebensdauern von fermionischen Ensembles, welche zunächst in das zweite Bloch-Band angeregt wurden, werden vermessen und die relevanten Band-Index verändernden Prozesse identifiziert. Im Fall von spinpolarisierten und daher nichtwechselwirkenden Fermigasen ergab sich eine Lebensdauer von 21 s. Wird stattdessen ein Gemisch von wechselwirkenden Zeeman Subzuständen bestehendes Fermigas im zweiten Band präpariert, ergibt sich eine Lebensdauer von 2.6 s. Mittels dieser Untersuchung konnten stoßinduzierte Zerfallsprozesse sowie Heizprozesse identifiziert und quantifiziert werden.

Contents

Introduction

Ultracold quantum gases are robust and resourceful systems for probing and understanding fundamental phenomena ranging from condensed-matter physics problems to high energy and astroparticle physics. After its prediction in 1925[Ein25], the first experimental observation of Bose-Einstein-condensation in 1995[And+95, Dav+95a] revolutionised research with cold quantum gases[Gre+02, BDZ08, Mad+00]. This was the first time that the important role of the underlying quantum statistics revealed itself in a collective macroscopic behaviour of a gaseous sample[And+95]. Particles with integer spin (Bosons) are allowed to occupy the same quantum state, which results in a macroscopic occupation of the system's ground state at very low but finite temperatures T. The phase transition from a thermal gas to a Bose-Einstein-Condensate occurs when the thermal deBroglie wavelength $\propto \sqrt{1/T}$ exceeds the mean inter-particle distance. Unique features of these degenerate Bose gases include long-range coherence[BHE00] and superfluidity[Mat+99, Abo+01].

On the other hand, particles of half-integer spin (Fermions) obey a different quantum statistics, prohibiting the simultaneous occupation of the same quantum state[Pau40], and therefore also Bose-Einstein-condensation. In contrast to Bosons, Fermions gradually fill up the available energy states of the system up to the Fermi energy, producing a drastically different many-body ground state. However, some effects of Bose-Einstein-condensation translate to degenerate fermionic gases. Although long-range coherence does not exist and Fermions can only interfere with themselves, effects such as superfluidity can still be observed, which is demonstrated by the emergence of a vortex lattice in an interacting degenerate Fermi gas[Zwi+05].

The combination of degenerate quantum gases of neutral atoms with periodic optical potentials gives rise to the formation of an optical lattice[HH93, Blo05]. These optical lattices are powerful systems to simulate many challenging condensed-matter problems including phase transitions[Jak+98]. In contrast to crystalline matter, optical lattices offer astonishing tunability, flexibility and controllability of a wide range of lattice parameters, enabling the precise engineering of diverse model Hamiltonians[Aid+13, Jot+14, Str+13,

Dut+15]. As an example, the many-body behaviour in a bosonic optical lattice can be well described by the famous Bose-Hubbard-Hamiltonian, where the onsite interaction U and tunnelling amplitude J between neighbouring lattice sites can be tuned by simply changing the intensity of the laser creating the periodic light potential. In 2002 this approach led to the first observation of the quantum phase transition from the superfluid phase to the Mott insulator phase[Fis+89] in a system of bosonic particles with repulsive interactions[Gre+02].

Modelling more sophisticated Hamiltonians can be achieved by applying a periodic external drive to the system, which introduces the emergence of a new equilibrium ground state. This technique, usually referred to as Floquet engineering, is widely used for the implementation of artificial gauge fields[Eck17, WS21]. This approach paved the way for the creation of artificial magnetic fields[Aid+11, Str+12], the realisation of topological band structures[Aid+14, Jot+14, GBZ16] and the implementation of kinetic frustration[Str+11]. Most of these examples only consider the lowest energy band of the optical lattice, although it has been shown that contributions of higher bands can play a significant role in the behaviour of these systems.

An alternative approach towards the simulation of Hamiltonians beyond conventional s-band Hubbard physics with optical lattices is the integration of orbital degrees of freedom by making use of higher Bloch bands. This technique has been pioneered with bosonic samples excited to higher bands and interesting new multi-orbital quantum phases have been realised[WÖH10, ÖWH11, Öls+13] and investigated theoretically[ML12, PT13, LL15, Jin+21]. For example the existence of a chiral metastable ground state at the minima of the second band of an orbital optical square lattice has been shown and has triggered interest in quantum phases with orbital degree of freedom[Koc+16, Slo+19]. Using similar techniques in different lattice geometries led to the first evidence of an atomic chiral superfluid with a topological excitation band structure and global angular momentum[Wan+21].

The usefulness of optical lattices in the context of quantum simulation of electronic crystalline matter requires in particular the use of fermionic particles[Köh+05, TS18], which assume the role of the electrons tunnelling and interacting in a lattice of ionic cores. A common model to describe electronic properties of solids is the Fermi-Hubbard-Model, which assumes a single static band and contact interaction between the particles. There has therefore been an increase in efforts to study the interaction of two-component Fermi gases in periodic optical potentials, which led to the first experimental observation of a fermionic Mott insulator transition in 2008[Jör+08].

This thesis for the first time realises the targeted population of higher Bloch bands with quantum degenerate fermionic atoms. An essential functionality of the bipartite optical square lattice used in this experiment is the ability to efficiently populate selected higher Bloch bands by dynamically changing the potential difference of neighbouring lattice sites. A central achievement of this thesis is the direct demonstration of orbital Bloch bands with quantum degenerate fermions in absorption images recorded after ballistic expansion, shown in Figure 0.1.

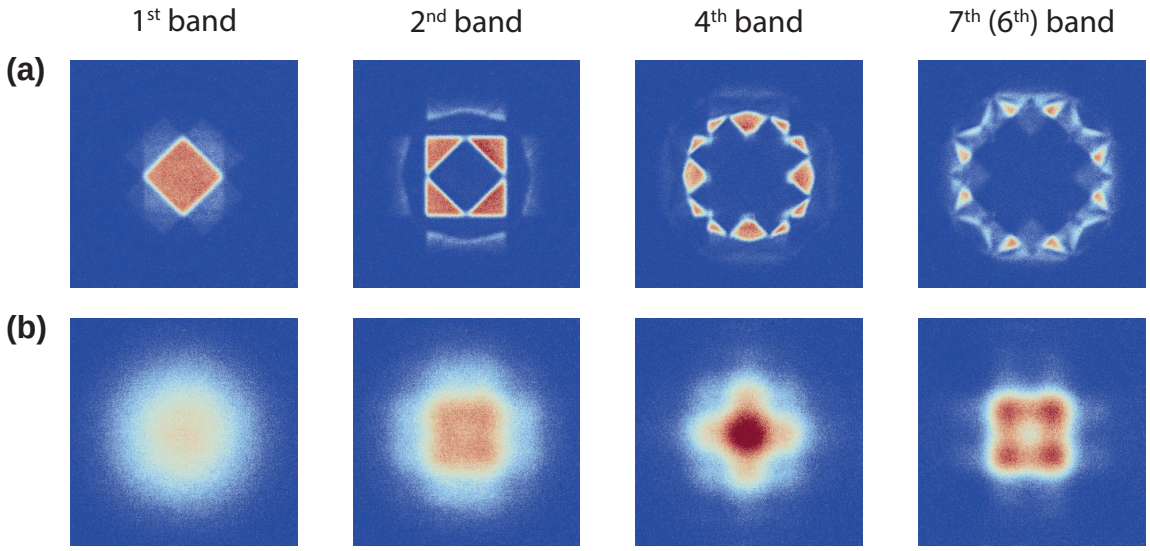

Figure 0.1: **Band populations and momentum distributions in the orbital optical lattice:** **(a)** shows the band population extracted with a commonly used technique called band mapping, where the quasi-momentum of each atom from the n^{th} band is mapped onto the n^{th} Brillouin zone. In **(b)** the momentum distribution of the particles directly reveals the orbital character of the optical lattice manifesting itself in the non-isotropic density distribution.

Furthermore, this thesis examines the band relaxation via binary collisions and heating for interacting fermionic spin mixtures and non-interacting spin polarised fermions, prepared in the second Bloch band. In the case of a spin polarised Fermi gas, interatomic s-wave collisions are forbidden by Paulis exclusion principle resulting in band lifetimes exceeding 10 s. Loading an interacting Fermi gas composed of a balanced mixture of two Zeeman sublevels into the second Bloch band results in the interaction induced band decay to the lower-lying first Bloch band. A minimal model was developed to identify the relevant relaxation mechanisms in good quantitative agreement with experimental data.

General outline of this thesis:

Chapter 1: Creating a degenerate Fermi gas: The hardware of the experimental apparatus is described in great detail. The laser system and magnetic field architecture used for standard cooling techniques are described. Moreover the experimental sequence is outlined and explained in chronological order. The dependence of experimental parameters of the degenerate Fermi gas is investigated and state preparation methods using radio frequency techniques are benchmarked.

Chapter 2: Fermions in higher bands of an optical lattice: The bipartite optical lattice potential created by orthogonally interfering standing optical waves in a Michelson-Sagnac-interferometer configuration is introduced. Furthermore, previously established methods for selective population of higher Bloch bands are explained and applied to degenerate fermionic gases. A characterisation of accessible states of the orbital optical lattice with fermionic atoms is presented.

Chapter 3: Band relaxation from the 2^{nd} Bloch band: The lifetime measurement of interacting and non-interacting Fermi gases excited to the second Bloch Band of the orbital optical lattice is detailed. Band changing relaxation processes are identified and a rate equation model is developed to describe the time-dependent behaviour for both cases.

Chapter 4: Experiment control, absorption imaging and data analysis: The newly developed software control architecture used in the laboratory is explained in detail and the interplay with experimental devices is outlined. In addition, data analysis methods are explained including an image defringing algorithm.

Chapter 5: Conclusion and outlook: The main results of the thesis are summarised and an outlook on further research perspectives are given.

1 Creating a degenerate Fermi gas

The basis for research with ultracold atoms in optical lattices is the reproducible generation of degenerate quantum gases. This chapter describes an experimental apparatus that is capable of cooling fermionic potassium-40 beyond quantum degeneracy and, due to the high reproducibility of the experimental conditions, guarantees good framework conditions for research with these samples in optical lattices.

The first section 1.1 presents a brief overview of the experimental sequence used to create atomic clouds beyond quantum degeneracy. After describing the vacuum system in section 1.2, section 1.3 focuses on the laser cooling mechanisms used in the apparatus presented here and decribes their experimental realisation. The transfer of the atoms to a magnetic trap is described in section 1.4 and the following section 1.5 explains the radio-frequency evaporation used to cool the atoms after the transport. Section 1.6 presents an empirically optimised procedure to subsequently load the atoms into an optical dipole trap, results of the forced evaporative cooling in the optical dipole trap are shown. In the last section 1.7, a characterisation of the degenerate Fermi gas is given. The chapter is summarised in section 1.9.

The first version of the experimental apparatus described here, has been built by Arne Everbeck[Eve16], Robert Büchner[Büc17] and Raphael Eichberger[Eic18]. In its initial stage the focus was on the formation of a Bose-Einstein condensate of rubidium-87 atoms. In-depth discussions of this stage of the experiment are found in [Eve16, Büc17, Eic18]. In the following treatment, I will constrain myself to the experimental infrastructure added to enable the formation of a degenerate quantum gas of fermionic potassium-40 atoms, which has been achieved in June 2020.

1.1 Experimental sequence

Cooling atoms to quantum degeneracy requires the combination of several different methods, as all currently available methods are limited by various reasons throughout the

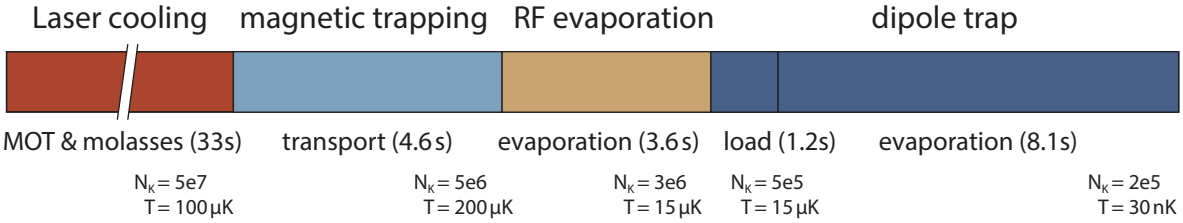

Figure 1.1: **Scheme of the experimental sequence:** To scale scheme of the experiment cycle used to cool potassium-40 atoms to quantum degeneracy. Four different experimental methods are combined consecutively: Laser cooling, magnetic trapping and transport, RF-evaporation and trapping and evaporation in an optical dipole trap. A schematic view including more detailed information can be found in the corresponding sections.

experimental sequence. This section gives an overview of the experimental sequence used in this experimental apparatus and the methods used to cool potassium-40 atoms to $0.18\,\mathrm{T_F}$.

In Figure 1.1 a to-scale timeline of the experimental sequence is plotted. The longest time step ($\approx$30 s) of the sequence marks the beginning with trapping and cooling of potassium atoms inside a three-dimensional magneto-optical trap (abbr.: MOT). With their two key features, namely trapping in momentum - and real space, they often present the first step in experiments with ultra cold atoms. After loading both species in a superimposed MOT, a short molasses phase is implemented to increase the phase-space density. Subsequently, the atoms are transferred into a magnetic trap, allowing magnetically transporting the atoms into the science environment with better optical access. As soon as the atoms are transported into this region, we perform radio-frequency evaporation to lower the temperature until capturing the atoms in a crossed optical dipole trap is possible. The last step is then forced evaporation inside the dipole trap to either produce a Bose-Einstein condensate of rubidium-87 atoms or to sympathetically cool potassium-40 atoms and create a degenerate Fermi gas.

1.2 Vacuum system

To reach quantum degeneracy in dilute quantum gases it is necessary to prevent thermalisation of the atomic ensemble with the environment and avoid thermal contact with the atmosphere. Therefore an ultra-high vacuum (abbr.: UHV) setup is used with pressures on the order of 10^{-11} mbar inside the science cell. The vacuum system was first built by Arne Everbeck, Robert Büchner and Hannes Winter and extensive descriptions are given in [Eve16, Büc13, Win13] as well as in [Büc17, Eic18]. Therefore, the following is just a

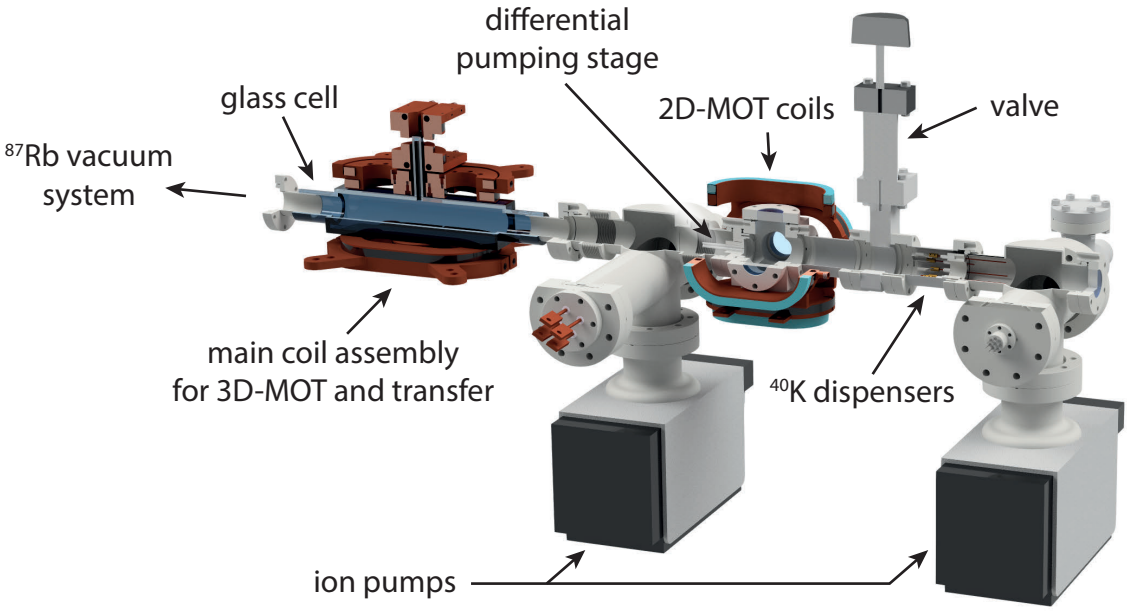

Figure 1.2: **Cross section through the vacuum system:** Cross section through the scientific main chamber (glass cell) and potassium source region, the rubidium source region is installed on the left of the glass cell and not shown here.

short introduction and covers the basics of the design built prior to this thesis and the adjustments made to the system in more detail.

Figure 1.2 shows a vertical cross-section through the vacuum system along the long axis. The setup basically consists of three major parts: a science chamber made of glass and two source regions enclosing this cell from both sides. The science cell itself is a $235 \times 50 \times 50\,\text{mm}$ glass cell with an $75 \times 12 \times 12\,\text{mm}$ appendix attached to it. The main chamber is connected to two almost symmetrical source regions via differential pumping stages(only one side is shown in figure 1.2). In total four ion pumps[1] are used to sustain a pressure of $7 \times 10^{-12}\,\text{mbar}$ in the main chamber and $2 \times 10^{-9}\,\text{mbar}$ in both source regions.

As a starting point of cooling atoms, one needs to choose an appropriate atomic source. Most atomic samples or alloys used in quantum gas experiments nowadays are in a solid-state at room temperature and UHV pressures. Therefore one has to heat them and evaporate the atoms into the volume of the vacuum system. In order to do so, there are two options almost exclusively used, namely heating small quantities of the desired material with an oven or by using dispensers. In this experiment, dispensers were chosen and integrated into the vacuum system. A dispenser is basically a small metal tube filled with the desired atomic species or an alloy containing it, flooded with Argon and sealed

1 VacIon Plus 55 StarCell from Agilent

with a droplet of Indium in our case. By applying a variable current to the dispensers, one is able to heat the metal pipe. After the initial activation (which is done by applying a larger current than in operational use), one can tune the evaporation of atoms by adjusting the current accordingly.

For both atomic species dispensers are used as an atomic source. Due to the very low natural abundance of potassium-40, we use enriched samples (5 % abundance instead of the natural 0.012 %) of potassium, which is bound in a potassium chloride alloy. Inside of the potassium source region, we integrated two enriched potassium dispensers[2], which are wired individually to ensure they can be operated independently from each other. In addition to those two, one pair of rubidium dispensers[3] is inserted inside the potassium source region. Inside the rubidium source region, three pairs of pure rubidium dispensers[3] are installed and are operated one pair at a time.

During the first assembly of the vacuum system, six potassium dispensers (all filled with enriched samples) were used and wired in pairs of two. After a partial failure of the dispensers, which led to the evaporation of unidentified metallic vapour, the transmission of the windows in the source region was reduced to roughly 70 %. Thus the vacuum chamber had to be opened in order to clean the windows. With this in mind, the decision was made to include a valve into the vacuum setup to separate the source region itself from the region with the dispensers. Figure 1.2 shows the location of the dispensers behind the valve inside the potassium source region after the insertion of the valve[4].

After cleaning of the windows, the first and only activated pair of potassium dispensers was oxidised, and the others were no longer able to be activated. Hence, at the beginning of this thesis, the vacuum chamber had to be opened again, and the dispensers had to be replaced. After an unsuccessful attempt to separate the source region from the dispenser region with the valve included for this purpose, it was found to be leaking. Therefore the whole vacuum system had to be flooded with Argon, and the exchange of the dispensers had to performed quickly in the way described above while replacing the valve. A short analysis of the valve afterwards indicated that the exposure to chemical reactive potassium atoms over an extended period of time might have damaged the seal. A similar phenomenon was observed by other institute employees of the group of Henning Moritz[5]. Therefore, the replacement valve to separate the source region and the dispenser has to be assembled such that the seals are not directly exposed to the atomic beam.

2 AS-K40-30-3F_0.05 from AlfaVakuo e.U.
3 RB/NF/7/25 FT 10+10 from SAES Getters
4 5GVM-40CF-MV-S from Vacom
5 Alexandra Mozdzen and Martin Schlederer gave valuable insights and reported the same problem

1.3 Laser cooling

The development of different and more versatile sources of laser light led to the rapid expansion of various research fields, one of them being the field of ultracold atoms. Equipped with these tools, new techniques were developed for cooling single atomic species, namely laser cooling, superseding conventional cryogenic cooling by roughly two orders of magnitude[HS75]. Thus to this day, laser cooling is the typical starting point of most cold atom experiments.

The basic principle of laser cooling consists in reducing the kinetic energy of individual atoms by scattering photons of a counter-propagating laser beam. A large number of scattering processes leads to an effective momentum transfer in the propagation direction of the laser and, therefore, a slowdown of the atoms. During this deceleration, the resonance frequency changes due to the diminishing Doppler shift. Choosing an appropriate detuning one is able to enhance the deceleration of fast atoms compared to the acceleration of resting atoms. Using three pairs of counter-propagating laser beams, one for each spatial dimension, one is able to capture atoms in momentum space, which is called optical molasses. Adding an inhomogeneous magnetic field to optical molasses to enhance the scattering rate for atoms in the outer regions of the trapping volume creates a force pointing towards the trap centre, leading to trapping in real space as well. This combination of optical melasses and an inhomogeneous magnetic field is called a magneto-optical trap[Chu+85] (abbr.: MOT).

In this section, a short description of the laser cooling methods used in this experimental apparatus are presented; for a comprehensive theoretical description of laser cooling mechanisms, see [Met99]. After presenting the level scheme (subsection 1.3.1), a short technical description of the laser system is given (subsection 1.3.2), and frequency stabilisation methods are explained. Afterwards, the laser cooling sequence is introduced, and a characterisation of the potassium MOT is given (subsection 1.3.4). The last subsection (1.3.5) closes the section with an explanation of the subsequent molasses phase.

1.3.1 Level scheme

In order to successfully perform laser cooling of atoms, one has to establish a closed cycling transition scheme between their internal electronic states. As most alkali atoms do, potassium and rubidium offer almost closed cycling transition on both D-lines, and either of them can be closed by just driving one additional transition. The former is often referred to as the 'cooling laser'. The latter is repumping atoms into the almost closed cooling transition, which is why this laser is called 'repumping laser'.

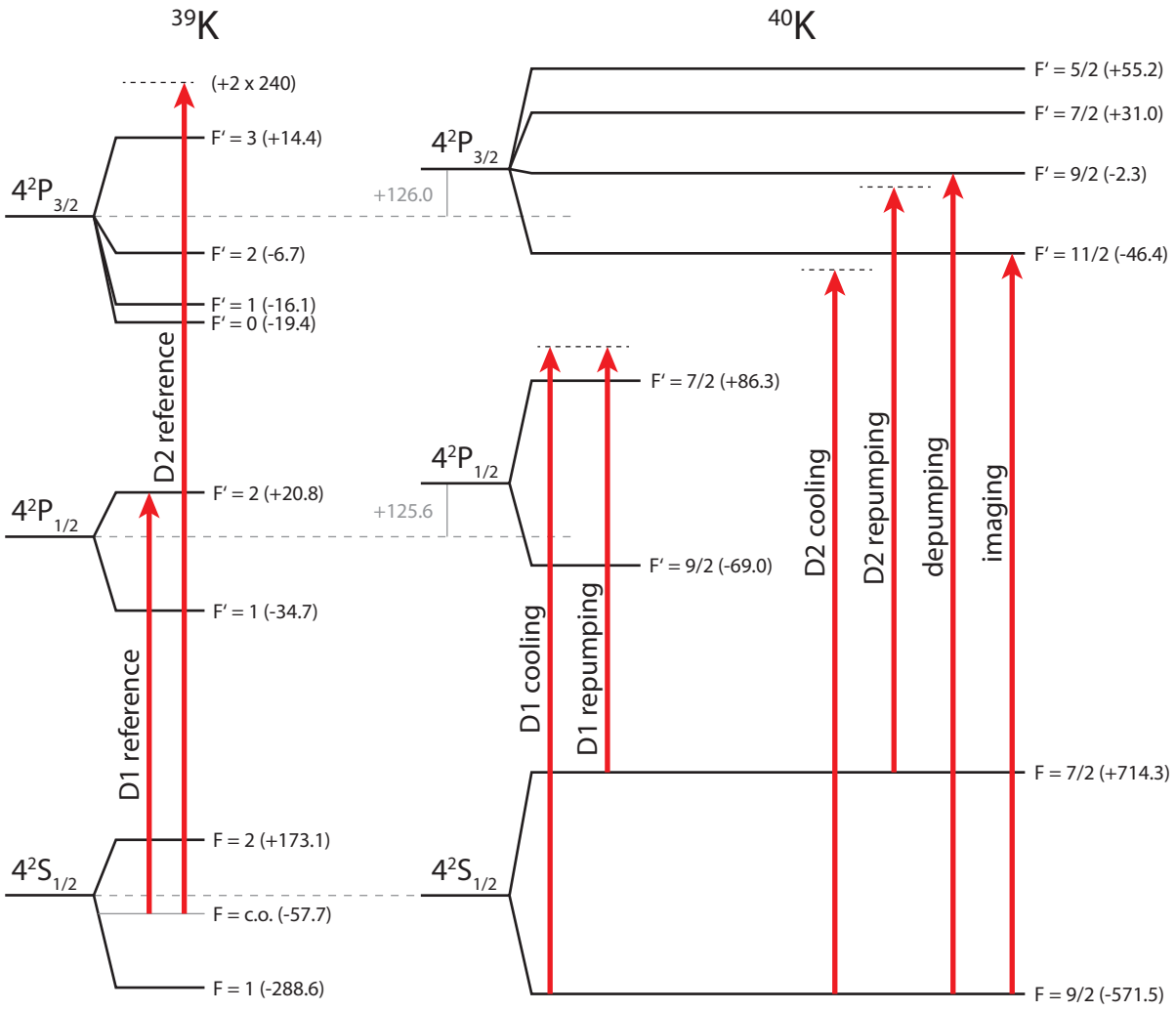

Figure 1.3: **Level scheme for laser cooling potassium-40:** All driven transitions for laser cooling are shown, their respective detuning can be found in the main text.

Figure 1.3 shows the chosen level scheme for laser cooling potassium in this experimental setup. This is done by driving transitions on the D2 line (between Zeeman sub-levels of $\left|4^2S_{1/2}\right\rangle$ and $\left|4^2P_{3/2}\right\rangle$, $\lambda_{D2} = 766.701\,\mathrm{nm}$). Furthermore the D1-transitions (between Zeeman sub-levels of $\left|4^2S_{1/2}\right\rangle$ and $\left|4^2P_{1/2}\right\rangle$, $\lambda_{D1} = 770.108\,\mathrm{nm}$) are driven in a combined two-color MOT operation and are driven solely in the subsequent grey molasses phase (see section 1.3.5).

1.3.2 Laser system

This subsection describes the laser system used for cooling potassium-40. The laser system for cooling rubidium-87 is almost unchanged since 2017, and one can find an extensive description in [Eic18, Büc17].

Either of the laser systems consists of typical optomechanical components and use commercial lasers as their backbone. One key feature of choosing them over most self-build designs is the increased stability and reliability as well as access to fast technical support from the manufacturer. Both laser systems are built on one separate optical table in order to reduce mutual disturbances between the laser system and the experimental apparatus. By doing so, one is able to decouple the experiment from many noise sources from the laser system, like stray photons and radio-frequency (from the AOMs/EOMs) and vice versa, shield the laser system from the experiment (i.e. reduce the effect of altering magnetic fields onto the spectroscopy setups). All laser beams used are then transferred via individual polarization-maintaining single-mode fibres[6] to the experiment table, and in addition, each of them features one mechanical shutter in front of the fibre.

The potassium laser system consists of five lasers, two reference lasers (on the D1 and D2 transition), the D2 cooling laser, the D2 repumper laser, and the D1 tapered amplifier. Figure 1.4 shows a schematic overview of the implemented laser system, which is capable of generating all laser frequencies for cooling, state-selective optical pumping as well as low-field imaging of potassium-40 atoms.

Potassium D2 reference laser

The potassium D2 reference laser is used as a frequency reference for all other laser sources operating on the D2 line of potassium-40. As a light source, an external-cavity diode laser[7] (ECDL) is used as a light source that offers up to 40 mW, which is enough to support two reference beams as well as beams for state-selective optical pumping and absorption imaging.

The frequency stabilisation is done via Doppler-free saturation spectroscopy on the $F = (1, 2) \rightarrow F' = c.o.$ transition in potassium-39. Because of the lack of potassium-40 in the natural abundance one is forced to perform spectroscopy on potassium-39 and shift the laser frequencies by AOMs to overcome the isotope line shift of these two species. This is done by using a $+2 \times 240$ MHz double-pass AOM setup[Don+05] before entering the

6 P3-780PM-FC-5 from Thorlabs
7 DLPro from Toptica Photonics

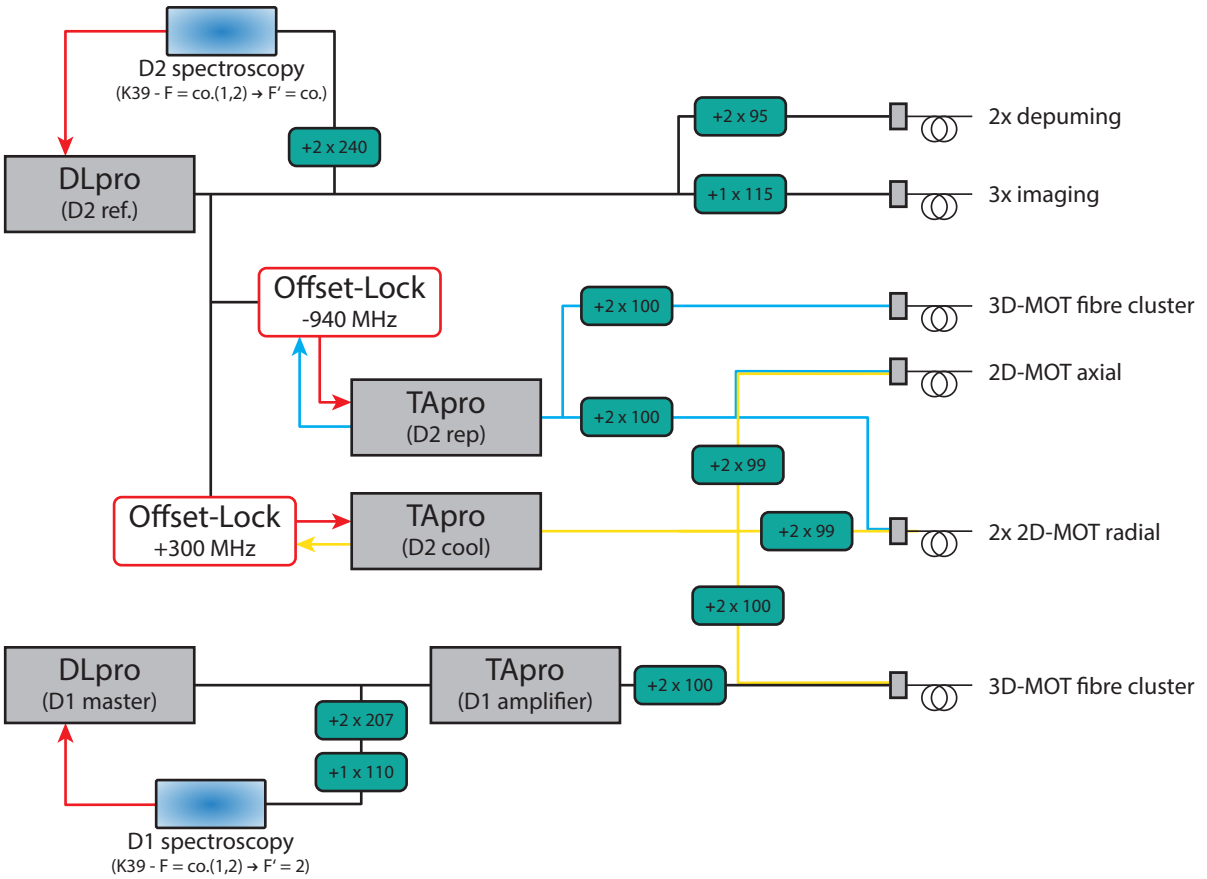

Figure 1.4: **Schematic view of the laser system:** Grey boxes represent commercial laser sources, red arrows visualise frequency locking dependencies. Small boxes with round edges sketch single- or double-pass AOM configurations with their operating frequencies given in MHz. For a better visibility, the D2 repumper is shown in light blue, the D2 cooler in yellow. Further details can be found in the main text.

spectroscopy setup, which is depicted in figure 1.5. For further remarks on the frequency locking see below.

The main beam is then split into four beams via polarising beam splitters, two reference beams acting as a frequency reference later on, one beam for state-selective optical pumping and one beam for the absorption imaging. The beam for the state-selective pumping, also called 'depump laser', is therefore frequency shifted by a double-pass AOM ($+2 \times 78\,\mathrm{MHz}$) to be resonant with the $F = |9/2\rangle \rightarrow F' = |7/2\rangle$ transition of potassium-40. Afterwards, this beam is overlapped with the rubidium depumper laser, split into two separate beams, coupled into optical fibres and transferred to the experiment. The imaging beam is passed through a single pass AOM ($+1 \times 115\,\mathrm{MHz}$) and is therefore resonant to the $F = |9/2\rangle \rightarrow F' = |11/2\rangle$ transition. Subsequently, the beam is overlapped with the imaging beam for rubidium, split into three beams and coupled into separate fibres to

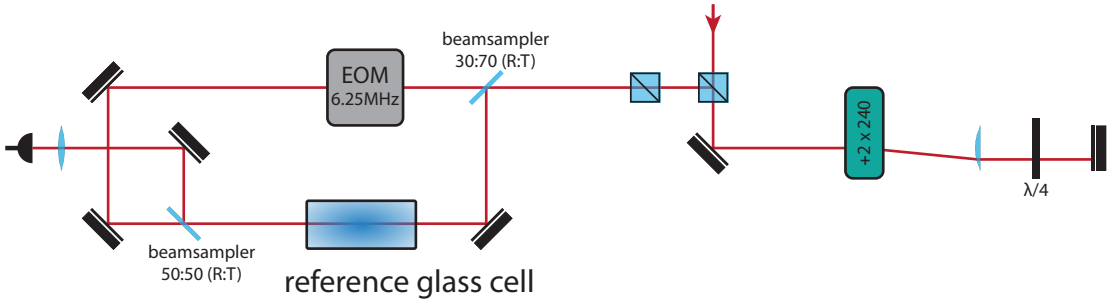

Figure 1.5: **D2 reference laser spectroscopy setup:** The spectroscopy beam enters the setup from the top and is frequency shifted with a double-pass AOM configuration. Afterwards, the beam is divided into a pump and probe beam and samples the reference glass cell in a modulation transfer spectroscopy setup.

enable imaging at different locations in the experimental apparatus. The reference beams are then used for stabilisation of the potassium cooling and repumping laser.

Potassium cooling laser

The entire cooling light for potassium-40 on the D2 transition is taken from a single tapered amplifier system[8], which consists of an ECDL master laser and a tapered amplifier semiconductor chip (abbr.: TA) in a master-oscillator power amplifier setup (abbr.: MOPA). After an upgrade of the TA chip, the total output power of ≈2.4 W is sufficient to deliver enough cooling light on the D2 transition for operating a 2D and 3D-MOT.

The potassium cooling laser is frequency stabilised via a difference frequency stabilisation with a frequency offset of +300 MHz relative to the reference beam from the potassium reference laser. For further remarks on the frequency stabilisation, see below.

The main output beam of the TA system is split into two separate beams, which are further frequency shifted and finally used to deliver enough power on the cooling transitions to operate the 2D- and 3D-MOT. The beam for the 2D-MOT is separated into two beams, and frequency shifted with two separate double pass AOMs in cateye configuration[Don+05]. This enables us to detune the cooling frequency for the two radial cooling beams (shifted by -2×100 MHz) and the axial cooling/pushing beam (shifted by -2×100 MHz) independently. Afterwards, each beam is overlapped with the respective repumping beam, coupled into a fibre and transferred to the experiment table (the radial cooling beam is split before and coupled into two individual fibres for each radial direction).

8 TAPro from Toptica Photonics

The beam used for the 3D-MOT is frequency shifted with a double pass AOM ($+2 \times 100$ MHz) and is therefore slightly red-detuned to the $F = |9/2\rangle \rightarrow F' = |11/2\rangle$ transition. The beam is then superimposed with the D1 laser beam via a line filter[9] and fibre coupled. Together they are transferred to a self-build fibre cluster, overlapped with the rubidium lasers for the 3D-MOT and split into six beams with a tunable power balance (for technical details, see Figure 1.7 in [Eic18]).

In a previous, yet no longer in use, configuration of the laser system, the cooling light for the 3D-MOT was produced by an additional TA system[10] with a total output power of ≈1.8 W. As a seed beam, a 26 mW beam taken from the TAPro system was overlapped with a 4 mW beam taken from the repumping laser and used as an injection beam into this additional TA. Using two double-pass AOMs, one was able to switch between this combined frequency D2 seed beam or another seed beam operating on the D1 line (the corresponding repumper on the D1 line was produced as a sideband of the seed beam with an EOM). This allowed us to switch between creating enough light on the D2 line during the MOT phase and afterwards amplifying the D1 seed beam to effectively operate a grey molasses (for further design considerations, see [Hac17]).

This previous setup relied on the simultaneous amplification of two laser frequencies ω and $\omega + \delta$ in one TA chip. We found that in the case of a small frequency difference δ additional sidebands appear (at $\omega + 2\delta$, $\omega + 3\delta$,...) and therefore reduce the total power of the carrier ω and the sideband $\omega + \delta$. This behaviour is also described in [Fer+99], and a lower limit for the frequency difference δ of ≈2 GHz was found, above which this effect is diminishing. In [MLF18] a theoretical model is given and numerical calculations were performed. Therefore amplifying a combined frequency seed beam with cooling and repumping light for potassium-40 on either transition unavoidably resulted in the creation of additional sidebands due to the small hyperfine splitting of the ground state of potassium-40 ($f_{HFS} = 1.2855$ GHz) and thus in the reduction of total power available for cooling. Additionally, this setup was limited to amplify light on either the D1 or D2 transition at a time and it was found beneficial to use both transitions during the MOT phase(see section 1.3.4), which is not possible in the case of switching between seed beams. Because of the two reasons mentioned above the laser system was redesigned to meet the new requirements of simultaneous use of D1 and D2 cooling and repumping light with sufficient power.

9 780nm MaxLine laser clean-up filter, LL01-780-12.5 from Semrock
10 TEC-400-0770-2000 from Sacher Lasertechnik

Potassium repumping laser

The entire repumping light for potassium-40 on the D2 transition is taken from a single tapered amplifier system[11], which consists of an ECDL and a TA chip. The total output power behind the included optical isolator is around 1.1 W and is used for 2D- and 3D-MOT.

The technical implementation of the potassium repumping laser frequency stabilisation is identical to the frequency stabilisation of the potassium cooling laser. In this case, the relative frequency offset relative to the second reference beam supplied from the potassium reference laser is $-940\,\mathrm{MHz}$.

At first, the main output beam is split into two parts and further frequency-shifted via AOMs to be used in either the 2D- and 3D-MOT. Figure 1.4 shows a schematic view of the laser system and visualises the interplay between all light sources. The beam for the 3D-MOT is frequency shifted with a double pass AOM setup ($-2 \times 93.6\,\mathrm{MHz}$) and therefore slightly red-detuned to the $F = |7/2\rangle \rightarrow F' = |= 9/2\rangle$ transition. The beam is then fibre coupled and transferred to the fibre cluster, where it is overlapped with the cooling beam and split into six individual fibres for the 3D-MOT. The beam for the 2D-MOT is frequency shifted with a double pass AOM ($-2 \times 90\,\mathrm{MHz}$) and split into two beams, which are overlapped with the cooling beams for the 2D-MOT and fibre coupled, to be transferred to the experiment optical table.

Potassium D1 master laser

The potassium D1 master laser is used as a frequency reference for the D1 light used for laser cooling in the experimental sequence. As a light source an ECDL[12] with a total output power of up to 52 mW. This laser is solely used to offer a seed beam for the D1 power amplifier and thus results in a MOPA setup for creating light on the D1 transition.

The frequency stabilisation is performed via an Doppler-free saturation spectroscopy on the $F = (1, 2) \rightarrow F' = |2\rangle$ transition of potassium-39. To compensate the isotope line shift between potassium-39 and potassium-40 the spectroscopy beam is frequency shifted before entering the spectroscopy setup by a double-pass AOM ($+2 \times 207\,\mathrm{MHz}$) and subsequently a single pass AOM ($+1 \times 110\,\mathrm{MHz}$). The spectroscopy setup chosen is optically identical to the setup used to stabilise the potassium D2 reference laser but uses direct current modulation of the diode laser current ($\omega_{mod} = 150\,\mathrm{kHz}$) rather than an EOM to create sidebands necessary for frequency modulation spectroscopy.

11 TAPro from Toptica Photonics
12 DLPro from Toptica Photonics

The main output beam is then frequency modulated with an EOM[13] to create the D1 repumping laser as a sideband of the D1 cooling laser. This ensures phase coherence between the cooling and repumping beam, which is necessary for a lambda-pumping scheme to use a D1 molasses efficiently (see subsection 1.3.5). Afterwards, this multi-frequency beam with ≈35 mW is used as a seed beam for the potassium D1 power amplifier.

Potassium D1 power amplifier

The potassium D1 power amplifier is used to amplify a seed beam offered by the potassium D1 master laser to supply enough power on the D1 transition for efficient laser cooling of potassium-40. A commercial tapered amplifier[14] is used as a light source and amplifies a seed beam of ≈30 mW to ≈2.4 W of light available for laser cooling.

Afterwards, this laser is fed into a double-pass AOM setup ($+2 \times 100$ MHz) to overcome the remaining frequency difference and is thus resonant to the $F = |9/2\rangle \rightarrow F' = |7/2\rangle$ transition. The laser is then overlapped with D2 cooling laser with a line filter[9] (see description above) and coupled into a fibre. Together they are then transferred to the fibre cluster.

One drawback of this implementation with a dual-frequency seed beam is the multi-frequency mixing processes involved inside the TA semiconductor chip for frequency differences smaller than ≈2 GHz. This solution was still chosen because it allowed an easy implementation in the existing experimental setup and provided a solution for a pumping scheme with simultaneously driven transitions on the D1 and D2 line during the MOT phase. The favourable solution to implement would have been to modulate the sidebands after the amplification, rather than using a dual-frequency seed beam but the amplifier output power exceeds the damage threshold of the EOM[13].

Frequency locking schemes

At first, the frequency stabilisations of the potassium laser system were a constant source of instability and made it impossible to find a long-term stable operating point for laser cooling. As a result, one was left with large particle number drifts on the order of 50 % after the MOT phase and a few changes to the frequency stabilisation, described in the following, resolved this issue.

13 EO-K40M3 from Qubig
14 BoosTA Pro from Toptica Photonics

Initially, we observed severe frequency drifts of the two reference beams on the order of several MHz over the course of a few hours. A few design changes compared to the prior build ([Win13, Eic18, Büc17]) improved the long term stability of the frequency reference beam and therefore the absolute frequencies of the potassium D2 cooling and repumping laser. The frequency stabilisation of the potassium D2 reference laser is done via frequency modulation spectroscopy [Bjo+83] onto a potassium reference cell as an absolute frequency reference. The old implementation used a Doppler-free saturation spectroscopy scheme in a retro-reflected setup, which was then replaced by a setup with two counter-propagating beams (pump and probe beam). By choosing this implementation one is able to set up a modulation transfer spectroscopy[Bjo+83, ES07] by modulating the pump beam and by four-wave mixing creating a modulation in the probe beam, which is then sensed by a beat signal on a fast photodiode. This new setup (shown in Figure 1.5) basically eliminated offset drifts in the error signal caused by changes in the absorption signal e.g. due to changing magnetic stray fields. A second advantage of choosing an EOM for frequency modulation rather than directly modulating the laser diode current is, that one is left with a reference beam with just one frequency component. This improved the stability of the difference frequency stabilisations as well. Another change made to the setup is replacing most polarisation dependent optics (mainly polarising beam splitters) by polarisation independent beam samplers[15], which reduced offset drifts in the error signal caused by polarization effects. The last change made to the setup was a separated demodulation circuit for the photodiode signal via standard RF components[16] instead of using the internal demodulation feature of the PID controllers[17] employed. With proper lowpass filtering of the error signal produced by this self-build demodulation circuit one was able to obtain an error signal with a zero-crossing on the line centre with reduced offset drifts caused by changing electronic potentials. By implementing these adjustments, we were able to achieve a frequency locking sufficient to ensure stable operation of the MOT system on a day-to-day basis.

The potassium D2 cooling and repumping laser are stabilised with a frequency difference stabilisation relative to the D2 reference beams provided by the potassium D2 reference laser. This is done by superimposing an ≈3 mW auxiliary beam taken from the side output port of the tapered amplifier systems with the corresponding reference beam and stabilising the oscillation frequency of the beat signal observed on a fast photo diode[18] with sufficient

15 BSS10 and BSW10 from Thorlabs
16 ZFSC-2-4-S+, ZP-3+ and ZFL-500+ from Mini-Circuits
17 DigiLock 110 from Toptica Photonics
18 G4176-03 from Hamamatsu

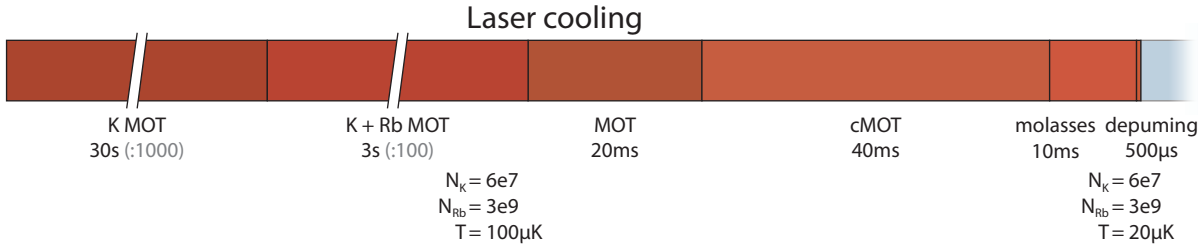

Figure 1.6: **Sequence overview of the laser cooling steps:** To scale visualisation of the laser cooling sequence used in the experiment cycle. Due to the long duration of the K(K + Rb) MOT loading phase the depicted scale is reduced by 1000(100). Detailed information for particle numbers and temperatures can be found in the main text.

bandwidth. This beat frequency is then compared to a constant frequency supplied by a frequency generator[19] with a high-frequency divider/PLL synthesiser[20], which provides a TTL signal as an error signal. The slope of this signal (and therefore the bandwidth of the PID control loop) can be tuned by choosing appropriate settings for the phase lock loop inside this PLL synthesiser. With the improvements made to the spectroscopy setup, the reference beam now consists of only one frequency component and thus the beat signal of the reference beam and the auxiliary beam only features one frequency component as well, which in turn resulted in improved stability once the frequency stabilisation engaged its setpoint.

1.3.3 Laser cooling sequence

Figure 1.6 visualises the experimental sequence for laser cooling used as a starting point in our experimental sequence (see also 1.1). In the following, the single steps involved are explained, their purpose is pointed out, and respective time scales are given. An in-depth characterisation of each step can be found in the respective sections (1.3.4 - 1.3.5).

Loading the magneto-optical traps - $30 + 2.5\,\mathrm{s}$

To load the maximal number of atoms in the potassium 3D-MOT, the potassium 2D-MOT is operated for 30 s solely. Typically around 6×10^7 potassium are captured in the 3D-MOT at a temperature of 75 µK. Directly afterwards, the rubidium 2D-MOT is switched on and a rubidium 3D-MOT is loaded superimposed to the potassium 3D-MOT. During this 2.5 s loading period of the rubidium 3D-MOT, both 2D-MOTs are operated, and potassium is further loaded. Typically 3×10^9 rubidium atoms are captured by this procedure in the

19 Agilent 33522A from Keysight Technologies
20 Eval-ADF4007 from Analog Devices

3D-MOT at a temperature of around 100 µK. Both 2D-MOTs are then switched off, and the combined 3D-MOT is operated for another 20 ms.

Compressed MOT - 40 ms

Subsequently the magnetic field gradients are linearly increased from 5.5 G/cm to 40 G/cm in 20 ms and held for another 20 ms. This compression of the MOT is called compressed MOT phase (abbr.: cMOT) and results in tighter spatial confinement and increases the atom density.

Molasses - 10 ms

In order to increase the phase space density, a 10 ms molasses phase is implemented. This leads to the reduction in temperature by utilising sub-Doppler cooling mechanisms. The grey molasses scheme for potassium-40 is operated on the $F = |9/7\rangle \rightarrow F' = |7/2\rangle$ transition of the D1 line and uses a Λ-scheme, while the rubidium-87 molasses is operated on the $F = |2\rangle \rightarrow F' = |2\rangle$ transition of the D2 line. The final temperatures reached after the molasses phase are 18 µK for potassium and 16 µK for rubidium respectively.

State-selective optical pumping - 700 µs

To magnetically trap neutral atoms, one has to transfer the atoms into magnetically trappable Zeeman sub-levels. For this purpose, a pair of two balanced counter-propagating laser beams is used, which are $\sigma+$-polarised relative to a quantisation axis provided by a weak magnetic offset field. After 700 µs of simultaneous optical pumping for both atom species, more than 90 % of all atoms are transferred to their respective 'low-field-seeking' state ($|9/2, 9/2\rangle$ for potassium-40 and $|2, 2\rangle$ for rubidium-87) and thus magnetically trappable.

1.3.4 Magneto-optical trap

The experimental apparatus utilises a typical 2D+3D-MOT setup for laser cooling both atomic species. In such a double MOT configuration, a 2D-MOT is used to produce a cold atomic beam, which is then used to load atoms into a 3D-MOT setup. Therefore the vacuum setup features two spatial separated regions to operate these 2D-MOTs, which are connected via differential pumping stages to the main chamber (glass cell), where a combined 3D-MOT for both species is operated.

parameter potassium 2D-MOT	transversal	axial
magnetic gradient	17.5 G/cm	
beam diameter	26.9 mm	14.4 mm
cooler intensity (per beam)	22 I_{sat} (110 mW)	63 I_{sat} (90 mW)
cooler detuning	-5 Γ (-30 MHz)	-5 Γ (-30 MHz)
repumper intensity (per beam)	27.2 I_{sat} (135 mW)	7.0 I_{sat} (10 mW)
repumper detuning	-5 Γ (-30 MHz)	-5 Γ (-30 MHz)

Table 1.1: Optimised parameters for the potassium 2D-MOT

In the first design of the experimental apparatus, two spatial separated 3D-MOTs for both species were planned to avoid particle losses caused by light-induced heteronuclear collisions. The subsequent combination of both atomic samples by merging the magnetic traps holding these ensembles led to substantial heating and thus had to be circumvented. As a result, the setup was changed to its present state, which can operate a combined overlapped two species 3D-MOT. A full description of the rubidium 2D and 3D-MOT, as well as the optimized parameters for exclusive operation of the rubidium MOT, can be found in [Eic18, Büc17]. Therefore the description and characterisation of the MOT setup provided here just present adjustments made to the sequence and setup in order to successfully achieve an optimised and balanced performance for the combined two species MOT.

2D-MOT

Inside the source region, a 2D-MOT is operated, which captures atoms from the thermal background gas provided by the dispensers (see section 1.2 as well as Figure 1.2). Using multiple UV-light LEDs, the background gas pressure in the 2D-MOT region is further increased due to light-induced atomic desorption of potassium atoms previously adsorbed on the vacuum chamber walls. This technique has been proven to be an inexpensive method to substantially increase the loading rate of the 2D-MOT for alkali atoms [Kle+06, Goz+93]. Two pairs of counter-propagating laser beams in a retro-reflected arrangement serve as cooling beams in the 2D-MOT to provide cooling in the transversal direction. One additional axial cooling/pushing beam, which is partially retro-reflected on a reflective substrate placed inside the vacuum system, provides additional cooling along the transversal direction and acts as a pushing beam to transfer the atoms through the differential pumping stage. The 2D-MOT operates solely on the D2-line of potassium-40 and drives

parameter potassium 3D-MOT	D2 lasers	D1 lasers
magnetic gradient	5.5 G/cm	
beam diameter	25 mm	25 mm
cooler intensity (per beam)	5.7 I_{sat} (25 mW)	0.8 I_{sat} (3.4 mW)
cooler detuning	-1 Γ (-6 MHz)	$+1.02$ Γ ($+6.1$ MHz)
repumper intensity (per beam)	1.2 I_{sat} (5 mW)	0.15 I_{sat} (0.6 mW)
repumper detuning	0 Γ (0 MHz)	$+0.92$ Γ ($+5.5$ MHz)

Table 1.2: Optimised parameters for the potassium 3D-MOT

the transitions $F = |9/2\rangle \rightarrow F' = |11/2\rangle$ (cooler) and $F = |7/2\rangle \rightarrow F' = |9/2\rangle$ transition. The magnetic quadrupole field is provided by two pairs of coils, which are placed outside the vacuum system and one pair of coils for either radial direction to compensate static stray fields. This water-cooled coil arrangement allows for magnetic field gradients in the range of 0 – 20 G/cm as well as magnetic offset fields up to several G.

The optimised parameters for operating the potassium 2D-MOT are summarised in Table 1.1 as well as diagrammed in Figure 1.7. Since the 3D-MOT performance is dependent on the atomic flux and velocity classes provided by the 2D-MOT, the parameters found for the 2D-MOT are highly coupled to the parameters found for the 3D-MOT (see table 1.2)

3D-MOT

The precooled atomic beam provided by the 2D-MOT is transferred from the 2D-MOT vacuum region, through the differential pumping stage, into the glass cell, where a 3D-MOT is operated. The magnetic field gradient is produced by the MOT coils as shown in Figure 1.10. In addition a total of five coils can be used to compensate magnetic stray fields in all spatial directions. The laser light is brought to the experiment table via six individual optical fibres and collimated via self-build couplers[21] and circular polarised by $\lambda/4$-waveplates.

The 3D-MOT for potassium is operated on the D1- and D2-line simultaneously, and thus a complex multi-level system is driven. The D2-lasers drive the $F = |9/2\rangle \rightarrow F' = |11/2\rangle$ (cooler) and $F = |7/2\rangle \rightarrow F' = |9/2\rangle$ (repumper) transitions, while the lasers operating on the D1-line drive transitions between $F = |9/2\rangle \rightarrow F' = |7/2\rangle$ (cooler) and $F = |7/2\rangle \rightarrow F' = |7/2\rangle$ (repumper). This simultaneous dual-line operation of the MOT

21 Thorlabs 60 mm cage system with a +150 mm lens, fibre NA: 0.12

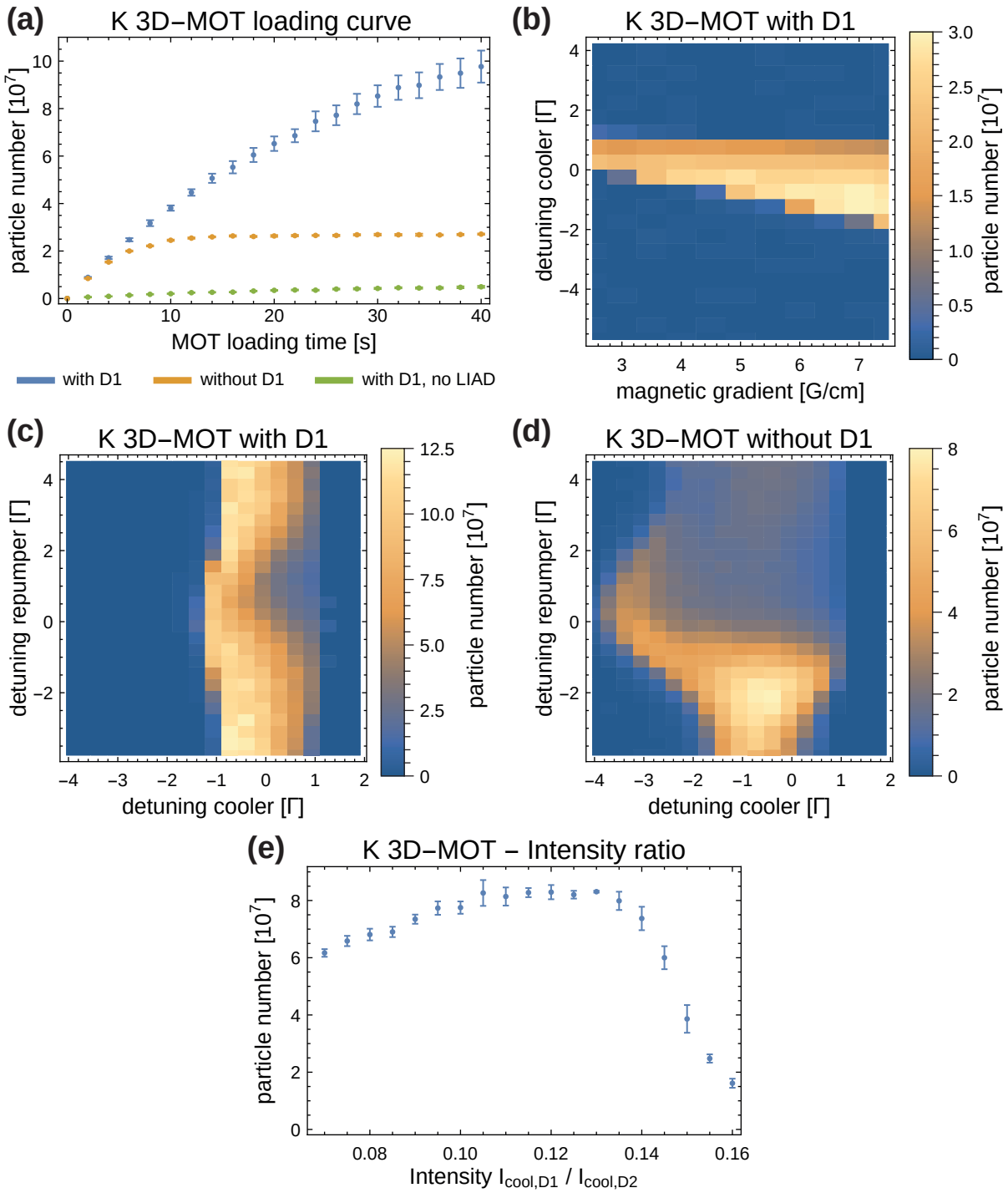

Figure 1.7: **Characterisation of the potassium-40 MOT:**
(a) loading curve of the 3D MOT with and without LIAD boost. Plots (b) - (e) show particle numbers after 30 s of loading the 3D-MOT.
Note: The particle numbers seen in plot (d) seem to disagree with the loading curve shown in plot (a). The reason for this discrepancy is that the loading curves are taken for the same detuning δ_{cool} and δ_{rep}, which are not optimal for the sole operation of the D2-MOT.

showed a significant increase of the saturation point of the particle number captured in the MOT and has been successfully used in [Wie19]. The highest phase space densities in the upcoming stages of the experimental sequence were achieved by utilising the dual-colour operation. Further investigations suggested the following working principle: Using lasers slightly red-detuned to the D2-transition, one provides trapping in momentum space and atoms are captured in a standard 3D-MOT setup. With the addition of the blue-detuned D1-light the spatial confinement is reduced and loss channels due to homonuclear collisions between potassium atoms are suppressed. The simultaneous D1- and D2-light operation of the 3D-MOT thus increased the particle number after a saturation time of around $20-25\,\mathrm{s}$ by roughly a factor of 4 (as shown in the loading curves in figure 1.7 (a)). This effect of reduced collision rates due to lowered densities and fewer losses becomes even more important for the suppression of light-induced heteronuclear collisions during the combined dual-species MOT for rubidium and potassium atoms applied in this experimental setup. The relative intensity of the D1-lasers compared to the D2-lasers has been proven to be very sensitive and plays a dominant role in optimising the performance of the 3D-MOT. Typically 6×10^7 potassium atoms are captured within $30\,\mathrm{s}$ at a temperature of $75\,\mu\mathrm{K}$. Extensive characterisation and optimisation measurements of the MOT parameters and their mutual dependencies were performed and diagrammed in Figure 1.7. The chosen parameters for the operation of the potassium 3D-MOT are presented in Table 1.2.

1.3.5 Molasses and state-selective optical pumping

After the MOT loading phase for both species and a $20\,\mathrm{ms}$ operation of the MOT without loading, a compressed MOT (cMOT) phase is used to increase the spatial confinement of the atoms. Temperatures of atomic samples reached in a MOT are typically on the order of the Doppler-temperature $T_D = \hbar\Gamma/(2k_\mathrm{B})$ and can be further decreased by implementing optical molasses schemes. For this purpose, an optical molasses utilises polarisation gradient cooling as a sub-Doppler cooling mechanism in the absence of magnetic fields to lower the temperature of an atomic ensemble[DC89, Let+88]. Including the extensive use of dark states in such molasses schemes and thus creating a grey molasses setup has been a leap in laser cooling made in the last decade. This section describes the Λ-enhanced grey molasses scheme used for cooling potassium atoms and characterises the newly implemented grey molasses used for rubidium. Further details regarding laser cooling rubidium atoms in this experimental setup can be found in [Büc13, Eic18].

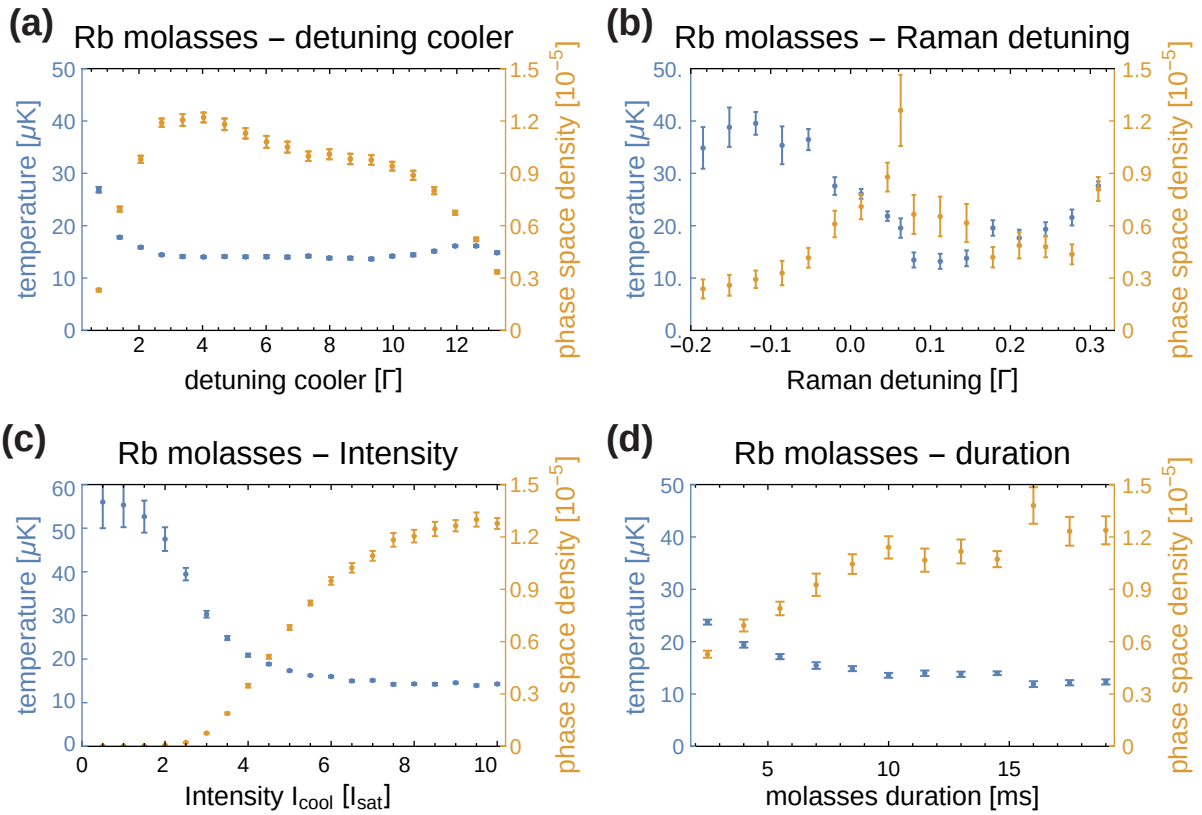

Figure 1.8: **Rubidium grey molasses performance:** temperature and phase space densities are measured and plotted against different varied experimental quantities. (a) shows the dependency against $\delta_{cool,Rb}$. The repumper detuning $\delta_{Rep,Rb}$ is linked via the relation for the Raman detuning (b). (c) cooler power I_{cool} is varied for a 10 ms molasses phase, (d) visualises the behaviour for different molasses durations.

Rubidium-87 grey molasses scheme

The laser cooling scheme used for the MOT and (former) bright molasses used in this apparatus involved optical pumping on the $F = |2\rangle \rightarrow F' = |3\rangle$ transition. Sub-Doppler cooling mechanisms like polarisation gradient cooling reduced the temperature after the cMOT from ≈100 µK to 45 µK. To effectively reduce the temperature of the potassium atoms via grey molasses scheme on the D1 transition, one has to cool rubidium atoms as well, because both ensembles are trapped in the same potential and thus thermalise via heteronuclear collisions.

By replacing the former bright molasses stage for cooling rubidium with a Λ-enhanced grey molasses scheme presented in [Ros+17], it was possible to reduce the final temperature after the molasses phase to 15 µK. This grey molasses scheme is based on driving the $F = |2\rangle \rightarrow F' = |2\rangle$ transition (detuning $\delta_{cool,Rb} \approx +4\Gamma$) on the D2 line as well as providing a phase-coherent repumper on the $F = |1\rangle \rightarrow F' = |2\rangle$ transition (detuning

$\delta_{rep,Rb}$). Choosing the detuning $\delta_{raman,Rb} = \delta_{cool,Rb} - \delta_{rep,Rb}$ precisely (on the order of $\Gamma/30$) allows to implement an efficient grey molasses scheme. Figure 1.8 characterises the performance of the rubidium grey molasses in this experimental apparatus. The final temperature achieved after the grey molasses stage is larger than similar setups already achieved with this molasses scheme for rubidium-87. Lowering the temperature even further is avoided because the following magnetic trapping and transport of the ensemble inside magnetic quadrupole traps is prone to losses due to Majorana spin-flips, which increase at lower temperatures. Therefore fine-tuning of the molasses parameters is done by observing the particle numbers found in the optical dipole trap or the BEC.

To provide the necessary laser frequencies, the laser light has to be detuned by roughly 170 MHz relative to the transition driven during the MOT stage. To avoid unwanted acceleration of the atoms during the switch-off of the magnetic field from the MOT stage, the laser light is switched off for 500 µs. During this time, the laser frequency is changed by tuning the setpoint of the frequency difference stabilisation of the laser via a frequency generator[22]. The phase-coherent repumper is provided by an EOM operating detuned by $\delta_{raman,Rb}$ relative to the ground state manifold energy splitting of rubidium-87 ($E_{HFS,Rb}/(2\pi) = 6.834683\,\mathrm{GHz}$). With the addition of this grey molasses phase, the final temperature after a 10 ms lasting molasses phase was decreased to 16 µK with a PSD of 1.2×10^{-5}.

Potassium-40 molasses scheme

After the first sub-Doppler cooling mechanisms for cooling potassium-40 atoms have been reported in [Mod+99], more evolved molasses schemes have been developed. Although a quite efficient sub-Doppler cooling mechanism on the D2-line was demonstrated[Bru+17], the prospect of using sub-Doppler cooling on the D1 line is expected to be more efficient due to the increased hyperfine splitting of the excited state. In [Fer+12, Sie+15, Tar15] Λ-enhanced grey molasses schemes on the D1-line of potassium-40 have been used to reach temperatures as low as $(5.7 \pm 0.2)\,\mu\mathrm{K}$, which is a factor of 25 lower than the Doppler-temperature T_D =145 µK for potassium-40.

The potassium-40 grey molasses scheme drives the $\left|4^2S_{1/2}, F = 9/2\right\rangle \rightarrow \left|4^2P_{1/2}, F = 7/2\right\rangle$ optical transition (detuning δ_{cool}) and closes the cycling transition with an additional phase-coherent repumping laser on the $\left|4^2S_{1/2}, F = 7/2\right\rangle \rightarrow \left|4^2P_{1/2}, F = 7/2\right\rangle$ optical transition (detuning $\delta_{rep,K}$). When the detuning $\delta_{cool,K}$ is chosen to the blue side of the resonance, dark states in the ground state manifold arise, and the coupling to the

22 Agilent 33522A from Keysight Technologies

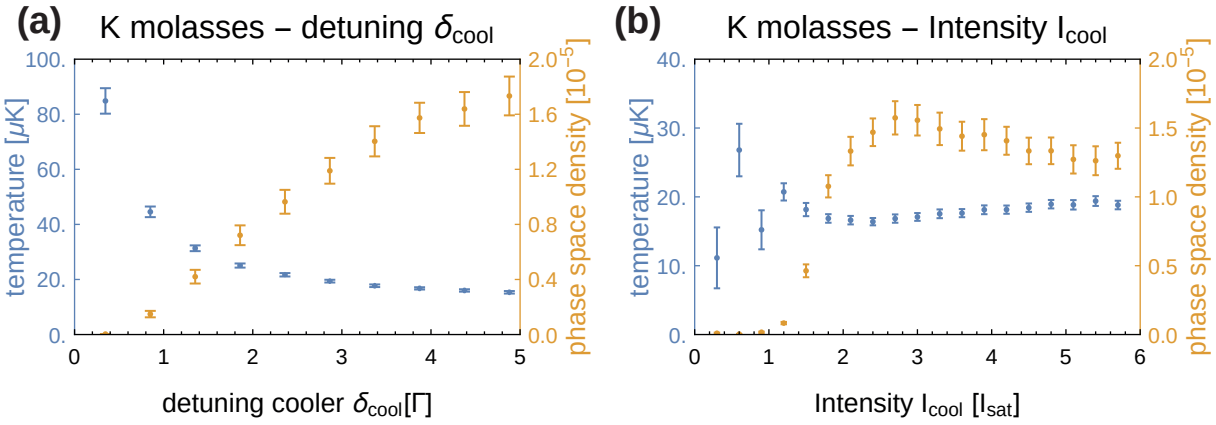

Figure 1.9: **Λ-enhanced grey molasses for laser cooling potassium-40:**(a) diagrams the dependency of the temperature and PSD after a 10 ms molasses phase against the detuning δ_{cool}. (b) visualises the dependency against the intensity $I_{cool,K}$ for the same molasses sequence.

light field is reduced[Fer+12]. This effect is enhanced by choosing the Raman-detuning $\delta_{raman,K} = \delta_{cool,K} - \delta_{rep,K}$ close to zero, as it gives rise to another mechanism to create a dark state. Phase coherent population trapping in a VSCPT-like dark state created at the two-photon resonance leads to a reduced coupling to the light field, and only residual motion couples the atoms to the cooling light provided[Gri+13]. This leads to an effective Sisyphus cooling mechanism in the presence of polarization gradient light fields as provided in our apparatus. Further details on molasses theory can be found in [Met99, Fer+12].

Like in the case of the operation of the rubidium grey molasses, the cooling light is switched off for 500 µs after the cMOT phase to avoid unwanted acceleration of the atoms during the decay of the magnetic fields. Afterwards the D1 light detuning is increased to $\delta_{cool} = 4\Gamma$ and subsequently switched on with an intensity of $4\,I_{sat}$. Since the rubidium-87 and potassium-40 molasses schemes operate simultaneously, the duration of both molasses phases has to be the same, and a 10 ms lasting molasses phase yielded sufficient cooling for both molasses schemes to achieve good transfer into the magnetic trap. The phase-coherent repumper for potassium-40 is created via phase modulation of the cooling light with an EOM[13], which operates at a relative detuning of $\delta_{raman,Rb} = +0.10\Gamma$ to the ground state manifold energy splitting of potassium-40 ($E_{HFS,K}/(2\pi) = 1.2858\,\mathrm{GHz}$).

Figure 1.9 (a) shows the dependency of the temperature and phase space density (abbr.: PSD) achieved in the molasses after 10 ms of operation against the detuning δ_{cool}. Phase space densities of 1.8×10^{-5} are achieved, which is comparable to values reached in [Fer+12] and is expected to allow for efficient evaporative cooling in the next steps of the experimental sequence. Figure 1.9 (b) shows the dependency of the temperature and PSD

against the intensity $I_{cool,K}$ during the 10 ms lasting molasses phase. Due to experimental reasons the Raman-detuning $\delta_{Raman,K}$ can not be tuned during the experimental sequence at the moment, such that it is not possible to determine the molasses performance against this sensitive parameter independently of the MOT loading behaviour. It has been observed that the saturation point of the particle number captured in the MOT is also dependent on the Raman-detuning of the D1 light provided, such that $\delta_{Raman,K}$ is chosen to maximise the PSD after the molasses phase. With the implementation of the Λ-enhanced grey molasses scheme into our experimental sequence, the temperature after a 10 ms long molasses phase was decreased to 18 µK and a phase space density of 1.5×10^{-5} was achieved.

State-selective optical pumping

After the molasses phase, the atoms occupy all Zeeman sub-levels and have to be pumped into low-field seeking states to be magnetically trappable. To perform this state-selective optical pumping the depumper lasers are used in two pairs, together with a pair of coils to provide a weak quantisation axis. By using two intensity balanced counter-propagating laser beams for each atomic species, the heating of the respective atomic cloud is minimised while obtaining effective optical pumping into the $|9/2, 9/2\rangle$-state (potassium-40) and $|2, 2\rangle$-state (rubidium-87). The optimal transfer of potassium atoms into the magnetic quadrupole trap was achieved with 700 µs optical pumping with a detuning of $+5\Gamma$ and an intensity of $0.07 I_{sat}$. The optimised parameters for rubidium were found to be -9Γ and $0.1 I_{sat}$.

1.4 Magnetic trap and transport

With various useful features for handling cold atomic ensembles, magnetic traps[Mig+85] are a standard technique used in most quantum gas experiments nowadays. Relatively large trap depths, magnetic transportation of the trapped ensemble, low heating rates and the possibility to perform radio-frequency evaporation (see section 1.5) are the main features of use in this apparatus. In a first step, the atoms are transferred into a magnetic quadrupole trap and afterwards transported to the science environment in the appendix of the glass cell (see Figure 1.2) via magnetic transportation. This section presents a brief overview of the sequence, which is discussed in detail in [Büc17, Eic18], and introduces the coil assembly used in all further steps of the experimental sequence.

Magnetic trapping of neutral atoms relies on converting the kinetic energy of the atoms into potential energy stored in the internal state. This can be achieved by creating

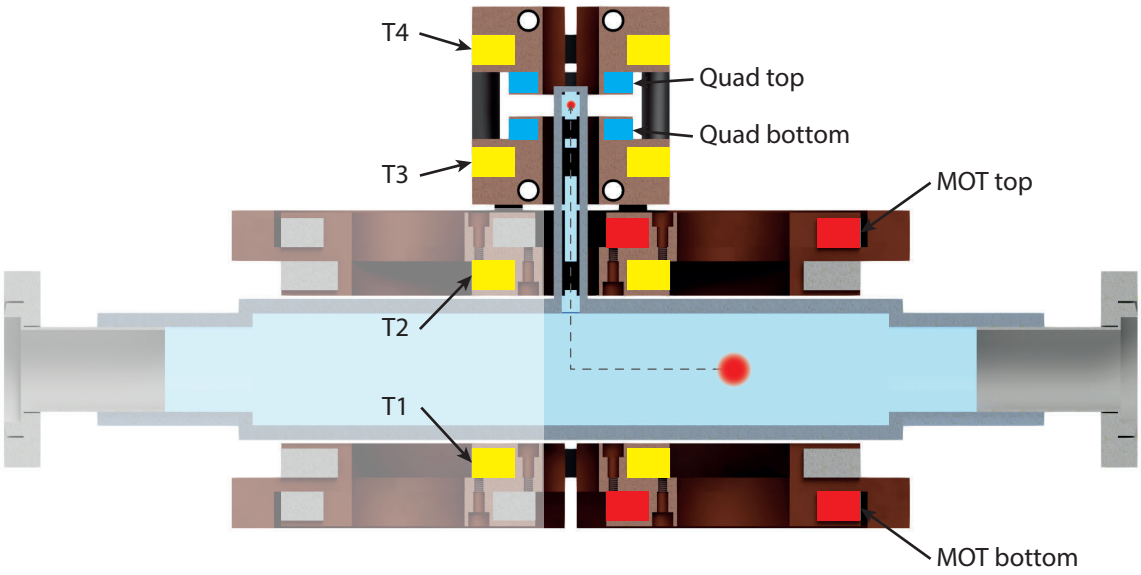

Figure 1.10: **Cross-section of the Coil setup** used for operating the magneto-optical trap, the magnetic transport as well as the magnetic trap for radio-frequency evaporation

inhomogeneous magnetic fields, which interacts with the magnetic moment μ of the atom. For an atom occupying the groundstate with principal quantum number F the potential energy inside a magnetic field $\mathbf{B}$ reduces in first order to

$$U_{\text{mag}}(\mathbf{r}) = m_F g_F \mu_B |\mathbf{B}|, \tag{1.1}$$

where m_F denotes the Zeeman sublevel quantum number, g_F the Landé factor of the hyperfine level F and μ_B the Bohr magneton. Thus different magnetic fields enable a variety of different trapping scenarios as well as transport of atoms trapped magnetically by adjusting the magnetic fields applied over time.

Figure 1.10 visualises the coil assembly used in the apparatus. One pair of coils in anti-Helmholtz configuration is used to create a magnetic quadrupole field for operating a MOT and subsequently trapping the atoms in the magnetic trap. Four additional coils (transfer coils 1-4, also referred to as T1-T4) are later used to transfer the atoms into the appendix. Another pair of smaller coils can be used to apply strong (19.8 G/A) homogeneous magnetic fields to utilise magnetic Feshbach-resonances to tune the interaction between the atoms.

The state-selective optical pumping (see subsection 1.3.5) transfers the atoms into low-field seeking states and thus can be trapped magnetically. After the optical pumping, the magnetic field of the quadrupole trap is switched on rapidly (<100 µs) via a quick start configuration, as described in [Büc17, Wir13]. For both atomic species ≈80 % of

the atoms are transferred from the optical molasses into the magnetic trap by using this experimental sequence. To allow for relaxation of residual motion of the atoms in the magnetic trap caused by the switching protocol, the atoms are held for ≈50 ms. Typically 2×10^9 rubidium atoms at 40 µK and 4×10^7 potassium atoms at 40 µK are trapped that way and can be transported into the science environment into the appendix.

The transport protocol (schematically shown in Figure 1.11) is divided into two steps, where a horizontal translation of the atoms to the centre of the glass cell is followed by a vertical transport into the appendix. For the horizontal transfer, the current through the quadrupole/MOT coils is ramped down while simultaneously increasing the current in both transfer coils T1 and T2, leading to a horizontal translation of the atoms directly below the appendix in 1.6 s. By choosing appropriate current ramp patterns for all four transfer coils T1-T4 the atoms can be moved vertically into the science environment in 2.5 s. Around 1×10^9 rubidium atoms and 2×10^7 potassium are transported in 3.5 s into the science region and held in a magnetic quadrupole trap realised by T3 and T4 with this sequence.

Because the magnetic field gradient is not constant during this transport procedure, the atomic ensembles are heated quite significantly (starting temperature ≈40 µK, end temperature ≈250 µK). Simulations showed that the existing coil setup unavoidably leads to compression and decompression phases during the transport and is thus prone to heating the atomic ensembles. Radio-frequency evaporation techniques described in section 1.5 allow reducing the temperature after the transport, such that the atoms can be trapped in an optical dipole trap. With this implemented magnetic transport sequence, a sufficient number of atoms can be transferred into the science environment. However, improving the transport efficiency and reducing the heating is suspected to significantly increase the particle number in the following steps. Further details on the magnetic traps as well as the transport procedure and coil electronics can be found in [Büc13, Eic18, Eve16].

1.5 Radio-frequency evaporation

Due to their limited efficiency at high spatial densities, laser cooling mechanisms alone are not sufficient to reach quantum degeneracy and have to be complemented with other cooling mechanisms like evaporative cooling as proposed in [Hes86]. The main idea behind evaporative cooling is to introduce an energy dependent loss channel, which removes the most energetic atoms from a trapping potential and allows for thermalisation of the remaining atoms. Such an evaporation mechanism can be used to increase the phase

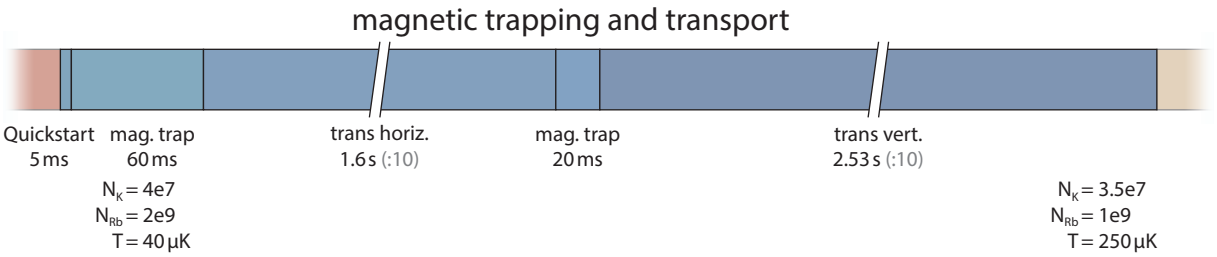

Figure 1.11: **Schema of the magnetic transport sequence:** In the first step, the atoms are loaded into the magnetic trap with a quickstart setup for the magnetic fields. After a short holding time, the atoms are then transported in the horizontal and subsequently moved vertically into the appendix.

space density (abbr.: PSD) of an ensemble if the loss of particles is overcompensated by the decrease in temperature. The experimental implementation of evaporation cooling mechanisms led to the first Bose-Einstein-Condensation in 1995 [And+95, Dav+95a] and until today constitutes a crucial technique in order to reach quantum degeneracy. Theory for different evaporation processes can be found in [Wal96].

Radio-frequency evaporation (abbr.: RF-evaporation) in magnetic traps is an evaporation method, where high-energetic atoms from a spin-polarized ensemble are transferred into untrapped high-field seeking states[Dav+95b]. Energy selectivity is achieved by combining two effects in the magnetic trap. The field gradient in a magnetic trap leads to a spatially dependent energy splitting of the hyperfine states due to the Zeeman effect, which is larger in the outer regions of the trap. By tuning an externally applied radio-frequency (also called RF-knife) in resonance to a transition depopulating the prepared low-field seeking state, one is able to transfer the atoms into untrapped high-field seeking states. Due to the fact that the likelihood of finding an atom in the outer region of the trap is increased for high-energetic atoms, the evaporation predominantly removes the hot tail of the energy distribution. After thermalisation of the ensemble via collisions, the mean kinetic energy of the ensemble is reduced, which leads to a decreased temperature. If one reduces the radio-frequency, this process can be repeated, and the temperature is reduced even further as long as thermalisation via collisions can occur. Further details on evaporative cooling as well as a simple theoretical treatment can be found in [Met99, Wal96, KDS99].

The apparatus presented here uses RF-evaporation in order to reduce the temperature in the magnetic trap after the atoms are transferred into the appendix (see section 1.4). Figure 1.12 (a) visualises the RF-frequency sweep pattern, as well as the magnetic gradient ramp, applied plotted against experiment cycle time. Due to the lower particle numbers of potassium-40 ($\approx 2 \times 10^7$), it is advantageous to cool rubidium-87 ($\approx 8 \times 10^8$) atoms via

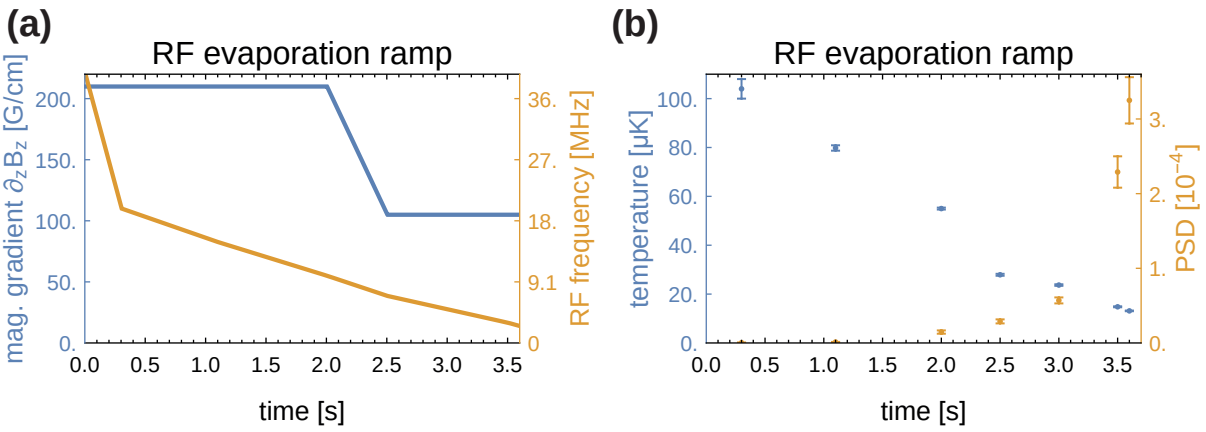

Figure 1.12: **RF-evaporation sweep pattern and RF-evaporation characterisation:** (a) plots the RF-evaporation sweep pattern as well as magnetic gradients versus sequence time. (b) shows the temperature and PSD for selected endpoints of the evaporation ramp pattern for rubidium-87

RF-evaporation and ensure thermalisation between both atomic species to sympathetically cool potassium-40 as presented in [Roa+02]. Therefore the evaporation process has to be atom species selective, such that only rubidium-87 atoms are removed from the trap via the RF-knife and potassium-40 atoms are unaffected by the evaporation process. This selectivity of the evaporation process is possible due to the difference in the gyromagnetic factors of fine structure levels involved, which reduces the level spacing of neighbouring m_F-states of potassium-40 by a factor of 4/9 relative to the spacing found in rubidium-87. Thus the RF-knife predominantly drives the $|F = 2, m_F = 2\rangle \rightarrow |F = 2, m_F = 1\rangle$ transition in rubidium-87 and causes a transfer into untrapped states, while keeping the potassium atom number unaffected[Gol05]. To ensure optimal thermalisation of rubidium atoms in the evaporation process as well as proper thermalisation of the potassium ensemble via heteronuclear collisions, the involved collision rates have to be chosen appropriate to the evaporation rates. This can be done by choosing a frequency sweep pattern for the RF-knife[23] and adapting the magnetic field gradients of the magnetic trap accordingly, which changes the spatial confinement and thus the collision rates. In our case, a decompression of the magnetic field gradient from 220 G/cm to 110 G/cm was found to be optimal to achieve the highest PSD for potassium-40 after the sympathetic cooling. Figure 1.12 (b) plots the temperature as well as PSD for both atomic species for selected endpoints of the RF-frequency sweep pattern, while the temporal evolution of the ramp was kept identical.

23 VFG-150 from Photonics Technologies Ltd serves as a frequency generator, which output is then amplified with a high power amplifier LZY-22+ from Mini-Circuits.

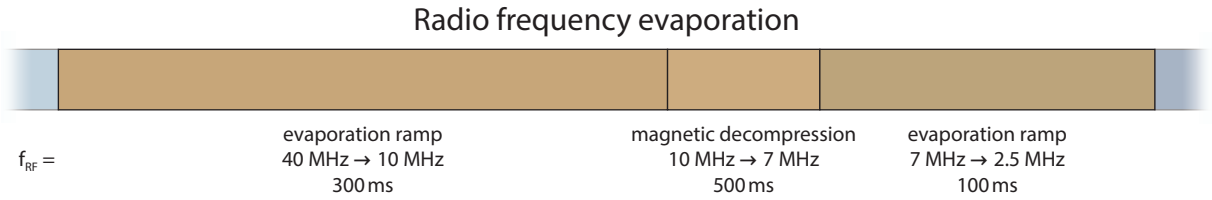

Figure 1.13: **Schematic sequence view of the RF-evaporation:** Schematic visualisation of the radio-frequency evaporation of rubidium to sympathetically cool potassium

In a magnetic trap formed by quadrupole coil configurations as used in this apparatus, an important loss channel is introduced due to the vanishing magnetic field strength in the centre of the trap. Atoms passing through the trap centre potentially undergo a Majorana-spinflip and might be transferred to a magnetically untrappable hyperfine state, which in turn causes the removal of these atoms from the trap. The reduced kinetic energy of the cold portion of the ensemble leads to an increased probability of finding these atoms close to the trap centre and thus an increased chance to undergo Majorana spin-flips. The probability of these Majorana spin-flips is dependent on the velocity of the atoms in the trap centre, which in turn depends on the magnetic field gradient applied. If one reduces the field gradient, the probability of Majorana spin-flips is reduced, which correspond to our finding of reduced field gradients to be optimal. To circumvent this loss channel, which dominates at lower temperatures and prevents an increase of the PSD, the atoms are loaded into an optical dipole trap (see subsection 1.6.2) which allows for further evaporation in the following (see subsection 1.6.3).

1.6 Dipole trap

Magnetic traps, as well as traps using radiation pressure, rely on the internal electronic state, which limits the possibility of realising various model systems with cold atoms. Therefore optical dipole traps (abbr.: ODT) are a common choice to trap ultracold ensembles of neutral atoms regardless of their internal state. If one is able to use this internal degree of freedom, more diverse physical phenomena are accessible. One example is to realise an incoherent spin mixture and tune the interaction between particles by addressing a Feshbach-resonance, while all spin components are subject to the same trapping potential.

In the apparatus presented here, a far-detuned crossed optical dipole trap is used to cool atoms to quantum degeneracy via evaporation and provides the trapping potential for

subsequent studies inside the optical lattice. This enables us to prepare spinor condensates of rubidium-87 or spin mixtures of potassium-40 and to investigate many body physics in higher Bloch bands of an optical lattice with spin degree of freedom as reviewed in [Li+18] and [ZZL15]. Another purely experimental reason requires the usage of an optical dipole trap in this apparatus: The magnetic quadrupole trap configuration used for RF-evaporation does not allow for an increase in phase space density once the loss channel via Majorana spinflips becomes dominant and removes the cold atoms from the trap. Therefore reaching quantum degeneracy in the quadrupole trap is impossible and requires the addition of an optical dipole trap.

In this section, the optical dipole trap used in the experimental apparatus is presented. The first subsection (1.6.1) focuses on a theoretical description and discusses trapping potentials formed by the ODT, the influence of gravitation and combined hybrid trap geometries formed by magnetic and optical forces. Subsection 1.6.2 presents the optimised loading procedure of the dipole trap, which maximises particle number and PSD after the transfer. The subsequent evaporation in the ODT is described in subsection 1.6.3 and improved protocols for the evaporation by tilting the trapping potentials are shown. A full characterisation of the dipole trap as well as measurements and descriptions of the beam parameters, electronics used for intensity control and stabilisation, as well as further technical details can be found in [Eic18, Büc17]. As these theses focus solely on the trapping of rubidium-87 atoms inside the optical trap this section is dedicated to pointing out problems and features of trapping two atomic species with different masses in the dipole trap presented here.

1.6.1 Optical dipole traps

An extensive description of optical dipole traps for capturing ensembles of neutral atoms can be found in [GWO99], therefore just a brief introduction is given.

Neutral atoms in light fields

Optical dipole traps rely on the dipole force, which is a result of the AC Stark shift of the Zeeman-sublevels of the atoms inside an external light field. Depending on the complex polarisability α of the atom a dipole moment is induced, which interacts with the light field and results in a force given by $F = -\nabla U_{\mathrm{dip}}(\mathbf{r})$, where $U_{\mathrm{dip}}(\mathbf{r})$ describes the dipole potential (Equation 1.2)

$$U_{\mathrm{dip}}(\mathbf{r}) = -\frac{3\pi c^2}{2\omega_0^3}\left(\frac{\Gamma}{\omega_0-\omega}+\frac{\Gamma}{\omega_0+\omega}\right) I(\mathbf{r}) \tag{1.2}$$

$$\Gamma_{\mathrm{sc}}(\mathbf{r}) = \frac{3\pi c^2}{2\hbar\omega_0^3}\left(\frac{\omega}{\omega_0}\right)^3\left(\frac{\Gamma}{\omega_0-\omega}+\frac{\Gamma}{\omega_0+\omega}\right)^2 I(\mathbf{r}) \tag{1.3}$$

Here c denotes the vacuum speed of light, ω_0 the angular frequency between the coupled electronic transitions, Γ the natural linewidth of the transition. ω labels the oscillation frequency of the light field with intensity $I(\mathbf{r})$. The scattering rate Γ_{sc} is then given by Equation 1.3. The different scaling behaviour for the potential depth and the scattering rate with respect to the detuning $\Delta = \omega - \omega_0$, therefore, allows a reduction of the heating rate caused by photon scattering for a given trap depth. For alkali atoms, the potential U_{dip} can be expanded into

$$U_{\mathrm{dip}}(\mathbf{r}) = \underbrace{\frac{\pi c^2\Gamma}{2\omega_0^3}\left(\frac{2+\mathcal{P}g_F m_F}{\Delta_{2,F}}+\frac{1-\mathcal{P}g_F m_F}{\Delta_{1,F}}\right)}_{:=\widetilde{\alpha}} I(\mathbf{r}) \tag{1.4}$$

where $\mathcal{P}$ characterises the laser polarisation ($\mathcal{P} = 0, \pm 1$ for linear and $\sigma^{\pm}$ polarised light), g_F the Landé factor of the ground state and m_F the magnetic quantum number of the Zeeman-sublevel. If linear polarised light is used the trapping potential is therefore independent of the internal spin state and thus different spin states can be trapped in the same trapping potential. $\widetilde{\alpha}$ is connected to the complex-valued polarisability α by $\widetilde{\alpha} = 1/(2\epsilon_0 c)\,\mathrm{Re}(\alpha)$.

Focussed laser beams

If focused laser beams are used to create an optical dipole trap, the potential can be easily obtained by calculating the intensity distribution $I_{\mathbf{r}}$, which can be decomposed in terms of TEM modes. The leading order in this expansion is the TEM_{00}-mode and is also referred to as a Gaussian beam, which in general can be elliptical. The intensity profile of an elliptical beam with beam waists $w_{i,0}, i \in \{x, y\}$ and Power P propagating in z-direction is then given by

$$I_z(\mathbf{r}, P) = \frac{2P}{\pi w_x(z) w_y(z)} e^{-\frac{2x^2}{w_x(z)^2}-\frac{2y^2}{w_y(z)^2}} \tag{1.5}$$

where the beam radii at position z are calculated via $w_i(z) = w_{i,0}(1 + (z/z_{R,i})^2)^{1/2}$ with $z_{R,i} = (\pi w_{i,0}^2/\lambda)$ denoting the Rayleigh range and λ being the wavelength of the laser

beam. The fact that the intensity gradient along the propagation direction of the laser beam is far smaller than in the radial direction leads to very elongated trapping potentials, which can be circumvented by forming a trapping potential with more than one laser beam. If two focussed elliptical laser beams are crossed perpendicularly, the resulting intensity profile $I_{\mathrm{ODT}}(r)$ can be calculated via summation of two intensity profiles given by Equation 1.5 and relabelling coordinates according to their propagation direction. This only holds for linear polarized laser beams with orthogonal polarisation, such that the interference term between both electrical fields vanish and no intensity grating is created. The optical trapping potential U_{ODT} for two non-interfering laser beams is then given by the direct sum of the intensity profiles and reduces to

$$U_{\mathrm{ODT}}(\mathbf{r}) = \widetilde{\alpha} \cdot (I_x(\mathbf{r}, P) + I_y(\mathbf{r}, P)) \tag{1.6}$$

Harmonic approximation of the trapping potential

It is often useful to expand the trapping potential landscape in terms of a 3-dimensional harmonic oscillator. Therefore the potential

$$U_{\mathrm{HO}}(\mathbf{r}) = \frac{1}{2} m \left(\omega_x^2 x^2 + \omega_y^2 y^2 + \omega_z^2 z^2\right) \tag{1.7}$$

is chosen as an approximation, which can be determined by calculating the Taylor series of the potential around its local minimum. The trap frequencies $\omega_x, \omega_y, \omega_z$ are a useful quantity to compare different trapping scenarios, as they grasp the inner trap dynamics on an elementary level. Although for low kinetic energy compared to the trap depth, the orbiting angular frequency is in good agreement with the trap frequency calculated, the dynamics of higher energetic atoms have to be treated with care, as their orbits are larger and due to the anharmonicity of the potential their orbiting frequencies might differ from the trap frequencies obtained in the harmonic approximation[Met99]. For low kinetic energies, the harmonic approximation is a good approximation, and the calculated trap frequencies are suitable for describing the trap potential.

Influence of gravity

In any real system subject to the gravitational potential U_{grav} one has to incorporate this potential into all calculations because the effective trapping potential is tilted in the

direction of gravity. The potential for a particle of mass m subject to the gravitational acceleration g is given by Equation 1.8

$$U_{\mathrm{grav}}(z) = mgz \tag{1.8}$$

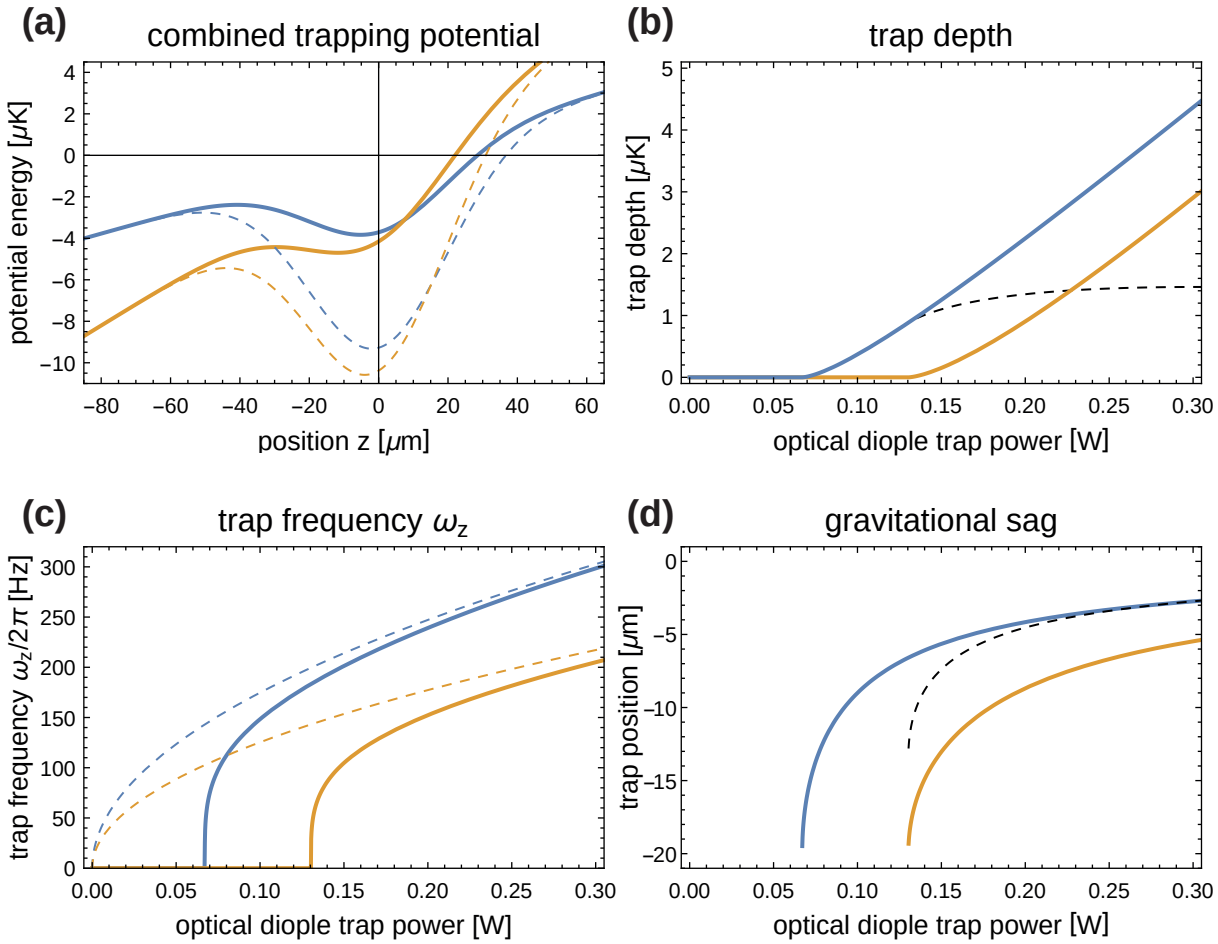

Figure 1.14: **Trapping potential properties for an ODT subject to gravity:** properties for potassium-40 are shown in blue, for rubidium-87 in yellow.
(a) total trapping potential for different optical powers $P = 160\,\mathrm{mW}$ (solid) per beam and $P = 400\,\mathrm{mW}$(dashed)
(b) trap depth (colored respectively) as well as their difference (black, dashed)
(c) trap frequencies ω_z observed in the direction of gravity with the influence of gravitation (solid) and without the influence of gravitation (dashed)
(d) trap centre position plotted against optical power for both atomic species (colored) as well as the relative shift of both trap minima (black, dashed). Special coordinate is given relative to the trap centre position without the influence of gravity

The tilt of the potential due to gravity leads to a reduction of the effective trap depth and a distortion of the trapping potentials shape, which is without the influence of gravitation directly given by the Gaussian envelope of the trapping laser beam. This can be seen in Figure 1.14 (a), where the trapping potential subject to gravity is plotted for two different powers of the dipole trap. The inclination of the potential also leads to a severe reduction of the total trap depth for small optical powers as plotted in Figure 1.14 (b). If one calculates the trap frequencies, this effect manifests itself in a trap frequency ω_z, which vanishes below a certain threshold P_{thres}, as there is no local minimum and trapping inside the potential landscape formed is no longer possible (shown in Figure 1.14 (c)). An additional effect caused by the tilt of the potential is the shift of the trap minimum in the direction of gravity. This effect is called gravitational sag and is different for different masses. Therefore the trap minimum for potassium-40 and rubidium-87 is shifted with respect to each other and has to be accounted for (see subsection 1.6.3). In Figure 1.14 (d), the position of the trap minimum is plotted relative to the trap minimum position without the influence of gravity.

Optical dipole trap in the apparatus

In this experimental apparatus, a crossed dipole trap is used with two horizontal along the x and y direction as schematically shown in Figure 1.15. A full characterisation of the dipole trap assembly, the laser source used, measurements of the beam characteristics as well as a description of the electronics and technical details can be found in [Eic18, Büc17]. Therefore just a brief summary is given.

In order to gain optical access required for implementing an optical lattice, a crossed optical dipole trap as well as imaging systems from different spatial directions at the same location, the atoms were transported magnetically into the science environment inside the appendix, as the 3D-MOT optics otherwise block too much optical access. Therefore an additional 15 mm thick aluminium breadboard placed 150 mm above the breadboard for the MOT-optics is used to create an additional layer, where optomechanical components can be mounted with 25 mm beam height. This additional breadboard is referred to as *lattice board*, and the implementation can be seen in a 3D rendering in [Eic18], figure 2.10.

The *lattice board* realised in the experimental apparatus and optomechanical setup, as well as beam paths, are shown in Figure 1.15. Two vertically placed cage system towers

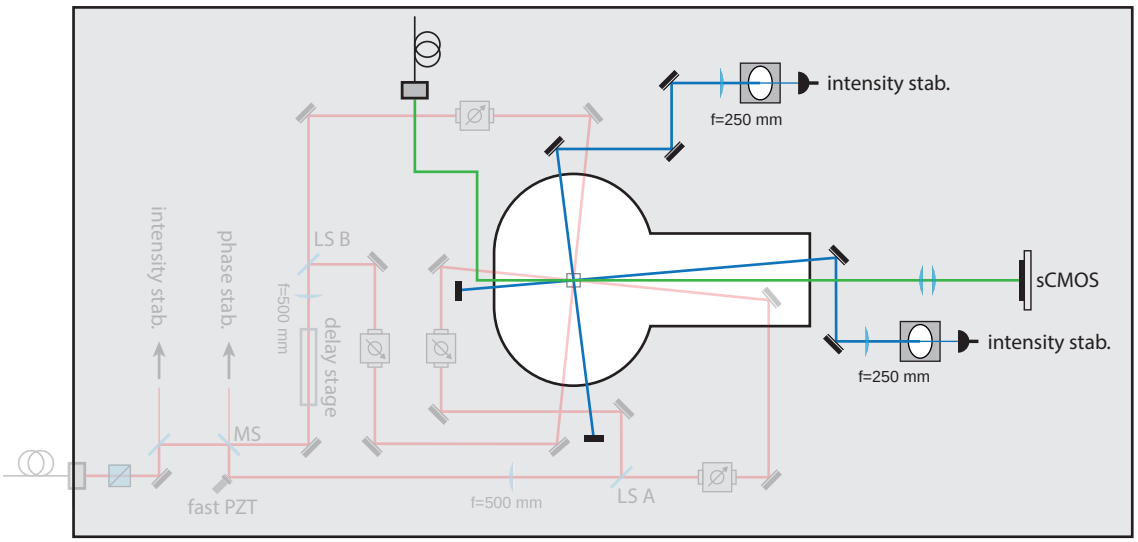

Figure 1.15: **simplified scheme of the *lattice board* - ODT:**
(top view) Both arms of the crossed optical dipole trap are brought to the lattice plate via optical high power fibres, expanded to elliptical beams with self-build couplers and focussed into the appendix. Further details can be found in [Eic18]. Components of the horizontal imaging system are shown in green. The optomechanical assembly for providing the lattice potential is greyed out, for details see Figure 2.2.

are used as couplers to collimate the laser beams provided by the laser system[24] and shape the spherically symmetrical Gaussian beam into an elliptical beam with an aspect ratio of 1:3.9. Both beams beams are then focussed using a plano-convex lens with +250 mm focal length, such that the beam radii for both beams are $\omega_{x,y} = 155\,\mu\text{m}$ in the horizontal and $\omega_z = 40\,\mu\text{m}$.

Both beams are reflected into the appendix via a beam walk realised with ultra-stable fine threaded mirror mounts. Due to the wedged nature of the appendix walls, one has to incorporate the refraction inside the glass of the appendix, and an angle is chosen, such that both dipole trap beams enclose a 90° angle inside the appendix. In order to suppress interference of the laser beams, which would create an intensity grating in the dipole trap, the polarisation is chosen to be orthogonal as well as their relative frequency is shifted by +220 MHz via two AOMs inside the laser system. In the case of residual suboptimal alignment of the polarisation, any resulting intensity grating in the dipole trap deviating

24 The Mephisto MOPA system cited in [Büc17, Eic18] had to be replaced because of a short circuit in the supply electronics as a result of a power failure and was temporarily replaced by a fibre laser produced by IPG Laser GmbH with an output power of 20 W. The optomechanical setup remained unchanged, and beam shaping before fibre coupling was adjusted accordingly.

from its unperturbed Gaussian envelope is oscillating faster than any relevant time scale in the experiment, such that the time-averaged potential is purely Gaussian.

The following section describes the loading procedure for the optical dipole trap in detail.

1.6.2 Optimized loading procedure

Loading via RF-evaporation precooled atomic ensembles from a magnetic quadrupole trap into an optical dipole trap comes with a few difficulties one has to circumvent. The main challenge is to preserve phase space density obtained in the evaporation and to transfer a sufficient number of atoms into the dipole trap to allow for efficient subsequent evaporation to reach quantum degeneracy (see subsection 1.6.3). This section is dedicated to presenting the empirically optimised experimental procedure to transfer potassium-40 as well as rubidium-87 atoms into the crossed optical dipole trap.

After the RF-evaporation around 1.0×10^8 rubidium-87 and 8×10^6 potassium-40 atoms are held in a magnetic quadrupole trap with a magnetic gradient of around 105 G/cm. To preserve phase space density obtained prior one has to energetically and spatially mode match the optical dipole trap onto the magnetic quadrupole trap or vice versa. The energetic mode match can be tuned by preparing atomic ensembles with different temperature distributions via adjusting the RF-evaporation in the quadrupole trap as described in section 1.5. In order to tune the spatial mode match, the trapping geometry of the magnetic trap and the dipole trap has to be aligned with respect to each other, which can be done by translating either one of them. Both aspects of mode matching are discussed in the following.

Energetic mode match

Loading atoms into trapping potentials with finite trap depth always leads to a truncation of the energy distribution of the atomic clouds captured in these trapping potentials, which leads to evaporation[Wal96]. Varying trap geometries feature different truncation properties dependent on their density of states as well as vastly different total trap depths for typical parameter sets accessible in laboratory environments. The total trap depth for the trap types involved in our experimental sequence are summarised in Table 1.3.

For an optical dipole trap, which is approximated as a 3D-harmonic oscillator one obtains an evaporation parameter of $\eta = 2.9$, which means that the temperature of the ensemble loaded into the dipole trap should be lower than $1/\eta$ of the total trap depth. In

Atomic species	MQT	MQT + gravity	ODT	ODT + gravity
rubidium-87	10 529 µK	8312 µK	137 µK	130 µK
potassium-40	10 529 µK	9483 µK	123 µK	119 µK

Table 1.3: **Comparison of Quadrupole and optical dipole trap trap depths:** Trap depths for the magnetic quadrupole trap (abbr.: MQT) are calculated for $I_{T3} = I_{T4} = 20\,\mathrm{A}$ equal to the magnetic field at the end of the RF-evaporation. Trap depths for the optical dipole trap are calculated with full output power of 4.5 W per beam as used to load the optical dipole trap.

the case of our dipole trap, this means, that the temperature of both atomic ensembles prepared by the RF-evaporation should be lower than 40 µK to prevent severe particle loss via plain evaporation, in which case particles leave the trap due to energetic mismatch. Measurements of the temperature of rubidium-87 after the dipole trap was loaded at full power yielded around $(13.1 \pm 0.1)\,\mu\mathrm{K}$ and $(14.6 \pm 0.3)\,\mu\mathrm{K}$ in the case of potassium-40, which is sufficiently lower than temperatures required and loading the dipole trap is not limited by the energetic mode match. Fine-tuning of the latter can be performed by slightly changing the frequency of the RF-knife on the order of 300 kHz and optimise the particle number loaded into the dipole trap and simultaneously observe the particle number obtained in the BEC or DFG respectively.

Spatial mode match

For loading atoms from one trap geometry into another, one has to spatially mode match both trapping geometries, which means to maximise the overlap of the density profiles obtained in both trapping potentials. In the case of our experimental apparatus, this implies that the spatial confinement of the atoms inside the magnetic quadrupole trap has to match with the dipole trap trapping volume for a given energy distribution.

Loading atoms from a magnetic quadrupole trap into an optical dipole trap comes with an additional problem: the preservation of spin polarisation of the atomic ensemble as well as the reduction of losses due to Majorana spinflips during the last steps of the transfer into the dipole trap. To maintain spin polarisation of the atomic clouds, one has to provide a finite magnetic bias field at the position of the optical dipole trap. As the magnetic quadrupole trap possesses a zero-field crossing at the centre of the trap(irrespective of the presence of an added magnetic offset field), spin polarisation throughout the loading sequence can not be provided if both trap centres are overlapped.

A possible countermeasure is the addition of a blue detuned laser beam, which repels the atoms from a region close to the trap centre and reduces the density around the magnetic zero, which reduces the chance to undergo a Majorana spinflip[Dav+95a, Jer14, Dub+12]. Optical access for guiding a plug beam onto the position of the quadrupole trap was not planned in the beginning, which made this solution infeasible.

Here, we have chosen another possibility to ensure spin polarisation throughout the loading procedure is to offset the magnetic trap and the optical dipole trap with respect to each other and thus obtain a finite magnetic field at the minimum of the optical dipole trap[Hän11]. This approach requires no additional equipment and allows for easy alignment. At any point in time, the total potential observed by the atoms is then given by

$$U_{total}(\mathbf{r}) = U_{\mathrm{mag}}(\mathbf{r}) + U_{\mathrm{ODT}}(\mathbf{r}) + U_{\mathrm{grav}}(\mathbf{r}), \tag{1.9}$$

which is referred to as *hybrid trap* in the following as it combines simultaneous trapping via magnetic and optical forces. The loading protocol used in the experimental apparatus presented here is diagrammed in Figure 1.16 (a) and described in the following: During the final steps of the RF-evaporation, the magnetic quadrupole trap field gradient applied is lowered to 105 G/cm, which is produced by identical currents through the transfer coils T3 and T4 of $I_{T3} = I_{T4} = 20\,\mathrm{A}$. Subsequently the optical dipole trap is ramped up in 100 ms to its maximum power of 4.5 W, immediately after which the magnetic gradient is reduced in 350 ms to 15.3 G/cm. This is done by ramping the current I_{T4} linearly from $I_{T4,inital} = 20\,\mathrm{A}$ to $I_{T4,final} = 3\,\mathrm{A}$. Experimentally, it has been observed that the maximum amount of atoms is transferred to the ODT if the current ramp for T3 is performed, such that the ratio I_{T3}/I_{T4} is not maintained but rather slightly changed during the transfer. A characterisation of this loading ramp is shown in Figure 1.16 (b), where the particle number loaded into the trap is plotted against $I_{T3,inital}$ and $I_{T3,final}$. By plotting the zero magnetic field position against sequence time (see Figure 1.16 (a), dashed plot), one recognises that the applied current ramp moves the magnetic trap zero towards larger displacements.

The magnetic field gradient at the end of the decompression is chosen, such that the slope of the potential caused by the gravitation for rubidium-87 atoms is cancelled, which leads to levitation of the atomic ensemble. For potassium-40, the applied field gradient presents an overcompensation of gravity, and a second local minimum is formed via the magnetic trap, such that the effective trap depth is maximised. Due to the fact that the dipole trap was ramped up in the beginning, the local minimum with the lowest

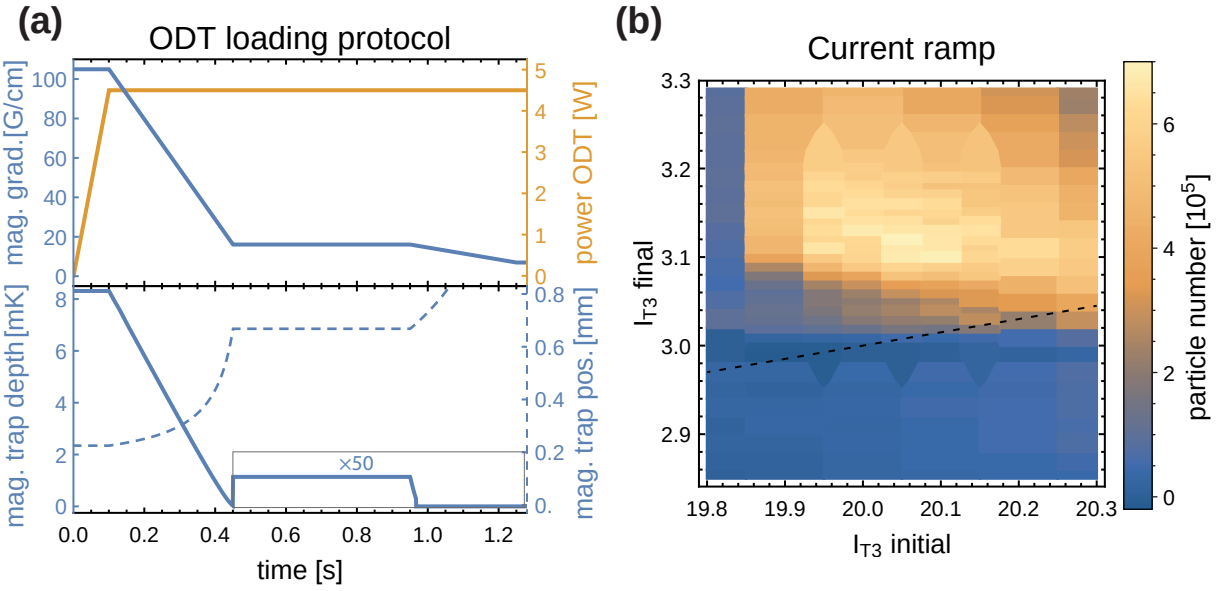

Figure 1.16: **Loading protocol of the ODT:**
(a) in blue magnetic field properties are plotted against time, in yellow the ODT power is visualised. The upper plot shows the magnetic field gradient in the direction of gravity (z-direction) as well as the power ramp of the ODT. The lower plot shows the trapping potential depth calculated for only magnetic trapping and the trap centre position (dashed) relative to the dipole trap position. In the beginning, the magnetic ramp applied drags the minimum position upwards while lowering the total trapping depth until the magnetic gradient applied just compensates gravity and causes levitation for rubidium-87 atoms.
(b) shows the particle number of potassium-40 atoms loaded into the dipole trap vs initial current $I_{T3,initial}$ and $I_{T3,final}$ of the current ramp pattern. The black dashed line indicates pairs of current for fixed ratio I_{T3}/I_{T4} such that the position of the magnetic trap minimum remains unchanged during the ramp protocol, rather than being dragged upwards.

potential energy throughout the loading procedure is given by the optical dipole trap. Dragging the minimum position of the magnetic trap upwards thus gently 'drops' the atoms into the dipole trap. At this point, the *hybrid trap* formed by optical and magnetic forces was lowered to a configuration, where the trap is purely given by the ODT and the magnetic gradient just compensates gravity for rubidium-87. This state of levitation is held for 500 ms, and subsequently, the magnetic field gradient is lowered in 200 ms to 7 G/cm, which compensates gravity and thus maximises the trap depth for potassium-40. Further details for the final magnetic gradient can be found in subsection 1.6.3 as well as Figure 1.17. After the magnetic gradient is lowered to its final value 5×10^5 potassium-40 and 1×10^7 rubidium-87 atoms are loaded into the dipole trap.

1.6.3 Evaporative cooling in a dipole trap

The main idea of evaporation cooling in an optical dipole trap is to truncate the energy distribution of the trapped atomic ensemble at high energies and allow for thermalisation. By continuously lowering the total depth of the optical dipole trap, this evaporation can be forced, and an efficient procedure to enhance phase space density is implemented[Ada+95].

Sympathetic cooling

In the case of spin polarised fermionic ensembles, the Pauli exclusion principle disallows s-wave scattering[Sad+00], and p-wave collisions are suppressed at temperatures below 30 µK for potassium-40[DeM+99, DeM01, Gol05]. Therefore thermalisation of such a spin polarised ensemble is expected to break down below these temperatures, and cooling potassium-40 atoms via plain evaporation is no longer possible. For this reason, other approaches have to be used, namely evaporation via spin mixtures of potassium-40 ($|m_F = -9/2\rangle$ and $|m_F = -7/2\rangle$) or sympathetic cooling via a bosonic species like rubidium-87[Roa+02].

In the apparatus presented here, the approach via sympathetic cooling has been chosen, which comes with benefits as well as drawbacks. One drawback is that one has to prepare cold atomic ensembles of two different atomic species or isotopes, which in turn requires more equipment and comes with complications along the experimental sequence like the simultaneous operation of two spatially overlapped MOTs, different trap frequencies and losses introduced by their mutual interaction. A benefit of cooling sympathetically is that the number of fermionic atoms cooled to quantum degeneracy can be enhanced by using the bosonic species as an effective coolant during evaporative cooling. In order to do so, one has to guarantee thermal contact and thermalisation between both species, which usually comes down to ensuring a sufficient interspecies scattering rate as well as the spatial overlap of both atomic ensembles. As mentioned earlier, two different atomic species or isotopes might observe different trapping potentials, such that either spatial overlap, as well as trapping depth, might differ. In the following, a method successfully employed in our apparatus is described, where rubidium-87 is used as an effective coolant for potassium-40 during evaporation in an optical dipole trap which is assisted by magnetic levitation. An in-depth introduction over different aspects of sympathetic cooling a fermionic species with a bosonic species can be found in [Ono17], where practical feasibility and limits are discussed.

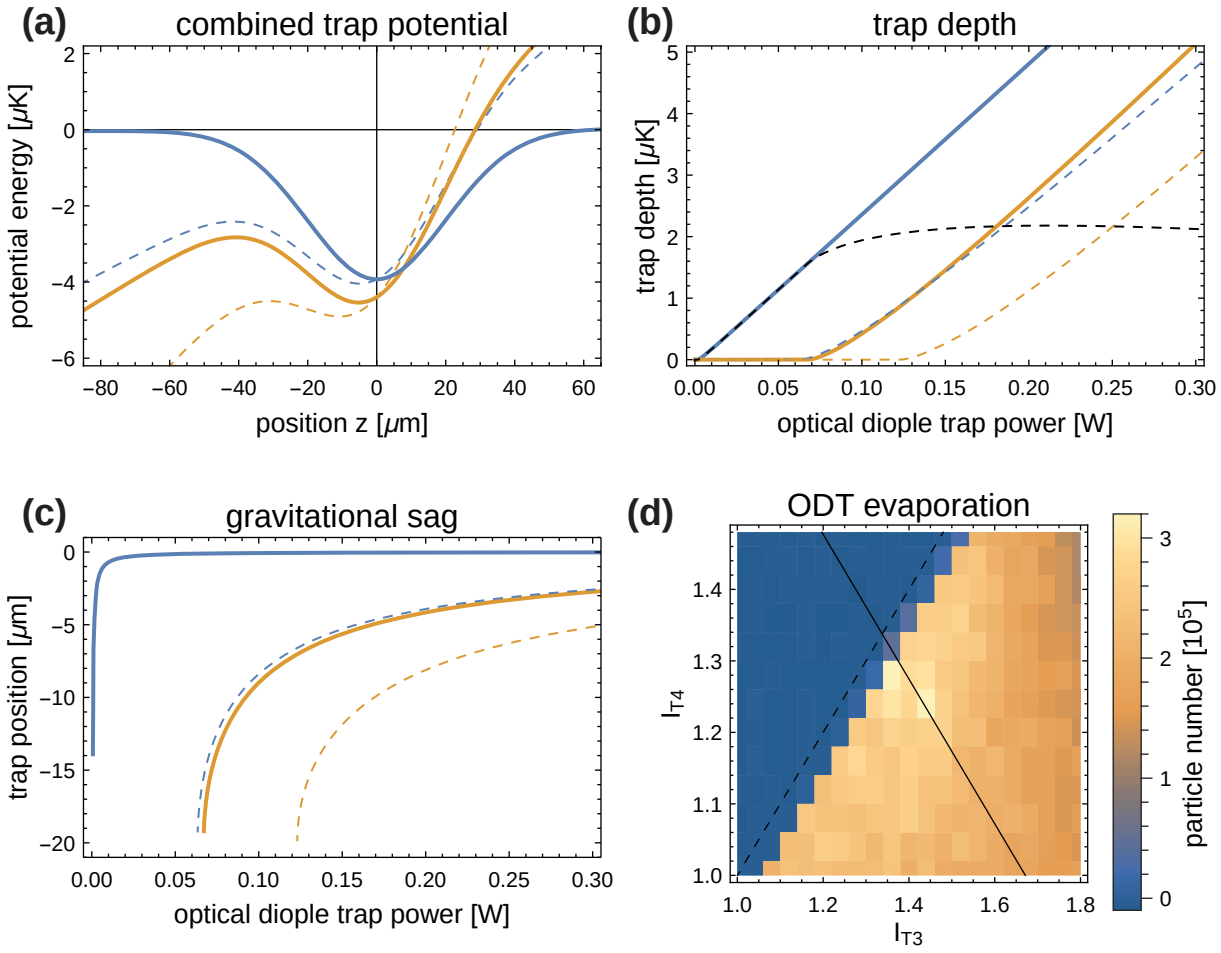

Figure 1.17: **Effects of finite magnetic field gradient during evaporation:**
(a-c) show properties for potassium in blue and rubidium in yellow. Dashed lines indicate results calculated for no magnetic field gradient and are shown for reference (also see Figure 1.14)
(a) shows the trapping potential obtained for 160 mW per ODT beam.
(b) diagrams trap depths obtained with tilt (solid) and without tilt (dashed coloured) as well as the difference of total trap depth for potassium and rubidium with magnetic gradient (black dashed).
(c) plots the gravitational sag for both species against ODT power.
(d) visualises the particle number obtained in the DFG with different magnetic gradients applied, which are produced by currents I_{T3} and I_{T4} in transfer coil T3/T4. The dashed line indicates current pairs, where the magnetic zero is overlapped with the ODT trap centre, to the left of the dashed line the magnetic zero is placed below the ODT. The solid line represents current pairs, which produce magnetic gradients of 7 G/cm and cause perfect levitation for potassium-40.

Enhancement via the *tilt trick*

The main idea behind the *tilt trick* of the trapping potential is to introduce different truncation energies $E_{T,K}$ and $E_{T,Rb}$ for both species and enhance the evaporation of rubidium-87 in turn for reduced evaporation of potassium-40 atoms. As long as thermal contact and proper thermalisation are maintained between both atomic species, the mean energy per particle is distributed and kept equal for both atomic species. Due to the lower truncation energy $E_{T,Rb}$ for rubidium, the evaporation is predominantly removing rubidium atoms, while the potassium atom number is almost unchanged. The difference of the truncation energy is introduced by tilting the total potential (Equation 1.9) with a magnetic field gradient, such that the ODT depth is maximised and gravity is compensated for potassium-40 atoms. Plots (a-c) in Figure 1.17 show the calculated trapping potential properties, including the *tilt trick*, and compares them to the untilted case. An additional effect of this levitation is the reduction of the relative gravitational sag, which maximises overlap and thus allows for more efficient thermalisation throughout the evaporation ramp.

A characterisation of the tilt applied in our experimental apparatus is shown in Figure 1.17 (d), where the currents I_{T3} and I_{T4} have been modified, and the particle number in the DFG has been observed. As one can see, the maximum particle number after the evaporation is obtained, if gravity is completely compensated for potassium (indicated by the solid line), whereas a complete loss of particles is observed, if the magnetic zero is placed below the atomic cloud during the evaporation, which causes the opposite and the trap depth is lowered due to the magnetic gradient. This surprisingly efficient optimisation of the evaporation led to an increase of the particle number in the DFG by a factor of $2-5$, while maintaining the temperatures achieved by evaporative cooling. Different reasons are considered to explain the underlying mechanism of this enhancement achieved by tilting the potential during the evaporation and are discussed in the following.

As seen by calculations, the energetic argument of different truncation energies due to the *tilt trick* only holds for optical powers below 1 W in our trap configuration, when the ratio $E_{T,K}/E_{T,Rb}$ turns larger than one and gets as large as 2.43 for the final evaporation depth of 160 mW with an applied magnetic gradient. The calculated trap depths in this case are 3670 nK for potassium and 1510 nK for rubidium, as compared to calculated trap depths of 1630 nK and 405 nK in the case of an untilted potential. Due to the observation that the dominant evaporation process takes place during the final steps of the evaporation, the energy consideration for the efficiency of the *tilt trick* is considered to be the key aspect here. This is somewhat expected, as the temperature of both ensembles loaded into the dipole trap (see subsection 1.6.2) is already much smaller than the total trap depth

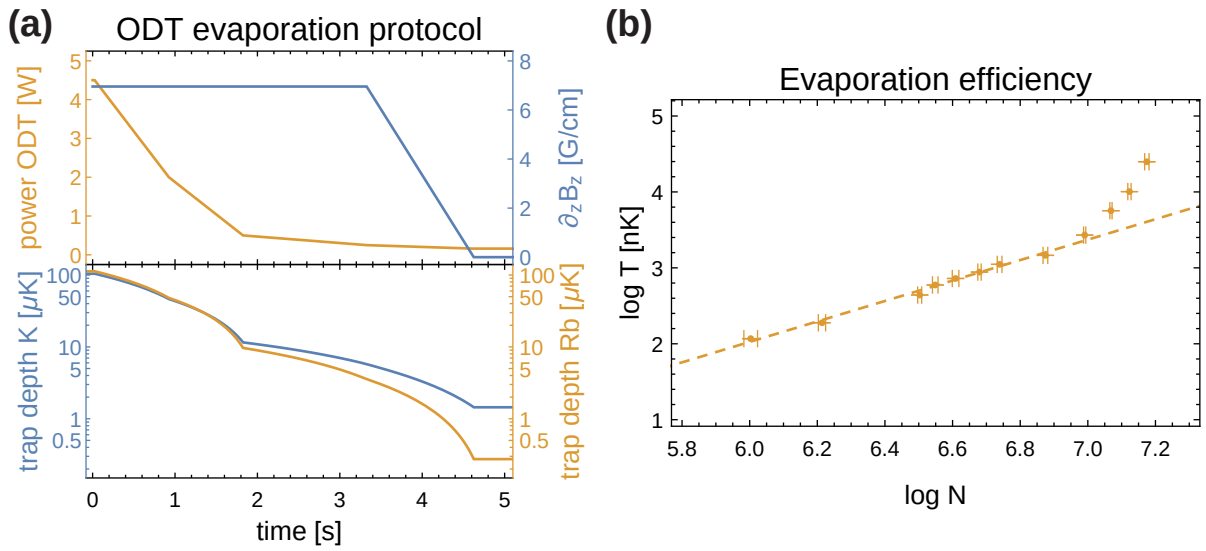

Figure 1.18: **Evaporation in the optical dipole trap:**
(a) The upper plot visualises the ODT power (yellow) and magnetic gradient $\partial_z B_z$ (blue) against sequence time. The lower plot shows calculated trap depths for potassium (blue) and rubidium (yellow) against sequence time. The point of equal trap depth is reached after 1.3 s with a calculated trap depth of 30.8 µK.
(b) plots the logarithm of the rubidium particle number N against the logarithm of the temperature. By fitting a linear function, the evaporation efficiency parameter $\tilde{\alpha}_{Rb}$ can be obtained.

(≈15 µK compared to ≈120 µK). Another reason for the improved evaporation efficiency is expected to be due to the reduced relative gravitational sag and improved overlap[Gol05]. Calculations showed that the relative shift of the trap centre position is as small as 5 µm and the expected cloud sizes for a DFG with 1×10^5 atoms are on the order of 30 µm, such that the overlap should be ensured either way. Additional effects like a finite magnetic quantisation axis provided by the bias field and thus altered scattering properties might play a role here but were not studied in detail.

evaporation ramp

The evaporation ramp used in the ODT is shown in Figure 1.18 (a), which plots the ODT power and calculated trap depths for both species against sequence cycle time. The evaporation efficiency can be extracted from Figure 1.18 (b), where the rubidium particle number and temperature are plotted on a logarithmic scale. Using the relationship $\tilde{\alpha} = (d \ln T)/(d \ln N)$ the evaporation efficiency can be determined and is found to be $\tilde{\alpha}_{Rb} = 1.34$ for rubidium atoms in this case[Wal96]. Due to technical reasons, the temperature of the

potassium sample can not be measured directly at the moment, such that the evaporation efficiency for potassium can not be determined.

At the end of the evaporation 2.5×10^5 potassium atoms are sympathetically cooled to $(30 \pm 3)\,\mathrm{nK}$[25] with a remaining 3×10^5 rubidium atoms at $(15 \pm 1)\,\mathrm{nK}$. Expressed in terms of the characteristic Fermi temperature T_F this yields a temperature for the potassium ensemble of $T/T_F = 0.178 \pm 0.004$. Other experimental setups using sympathetic cooling of potassium-40 atoms via cooling rubidium-87 found similar temperatures[Gol+04, Mod+03, Osp+06]. A discussion of why this temperature arises as a limit in cooling these two species sympathetically is discussed in detail in [Gol05]. Optimisation of the *tilt trick* protocol or more elaborated schemes presented in [Ono17] might enable sympathetic cooling of these two atomic species to even lower temperatures, but further studies were postponed. A characterisation of the degenerate Fermi gas prepared in this experimental apparatus is given in the following (section 1.7).

1.7 Fermigas

Below a characteristic temperature T_F, the Fermi temperature, ultracold ensembles of fermionic atoms at temperature T can no longer be described by the Maxwell-Boltzmann distribution, which is only valid for distinguishable particles. If the thermal de-Broglie wavelength $\Lambda_{dB} = \sqrt{(2\pi\hbar^2)/(mk_\mathrm{B}T)}$ is on the order of the interparticle distance, this is violated, and the ensemble has to be described with their underlying quantum statistics, which is given by the Fermi-Dirac statistic (Equation 1.10) for fermions[Cas06]. Ultracold quantum gases in this regime are also referred to as degenerate Fermi gases (abbr.: DFG).

$$f_{FD} = \frac{1}{\exp((E_n - \mu)\,/\,(k_\mathrm{B}T)) + 1} \tag{1.10}$$

Here f_{FD} denotes the occupation probability of a single-particle energy state n with energy E_n for a given ensemble with chemical potential μ and temperature T. The Fermi-Dirac statistic (abbr.: FD-statistic) is a direct consequence of the antisymmetry of the fermionic many-body wave function under particle permutation[Pau40]. One important implication of this antisymmetry is the *Pauli exclusion principle*, which states that two fermions are prohibited from occupying the same quantum state with respect to every quantum number. Therefore two fermions with the same spin can not be found

25 The absolute temperature was determined by applying the fitting routine given by Equation 1.11 to the DFG and subsequently calculating the temperature from the fit results using measured results of the trap frequencies. For details see [KZ08].

at the same location. This manifests itself in the fact, that the FD-statistic shows a maximum occupation number of 1 for every energy state. In the limiting case of $T \to 0$, every energy state below the Fermi energy $E_F = k_\mathrm{B} T_F$ is occupied exactly once; every state above is unoccupied. This implies that even in the case of $T = 0$, not all atoms occupy the lowest energy state but rather fill the energy states given by the external potential $V(\mathbf{r})$ from the bottom to the Fermi energy E_F. Note that for large temperatures, the Fermi-Dirac statistic is well approximated by the Maxwell-Boltzmann distribution $f_{MB} = \exp(-(E_n - \mu)/(k_\mathrm{B} T))$. An extensive introduction of the theoretical description for Fermi gases can be found in [Cas06, GPS08, KZ08, PS08].

Density distribution and fit model

An extensive description of quantitative analysis methods of absorption images of degenerate Fermi gases can be found in [KZ08]. The 3D density distribution of a degenerate Fermi gas imaged via absorption imaging can not be reconstructed, and only column densities, density profiles integrated along the imaging axis (z-direction), are recorded. For a trapping potential described as a 3D harmonic oscillator, the 2D column density is given by

$$n_{2\mathrm{D}}(x,y) = n_{2\mathrm{D},0} \frac{\mathrm{Li}_2\left(\pm \exp\left[q - \left(\frac{x^2}{R_x^2} + \frac{y^2}{R_y^2}\right) f\left(e^q\right)\right]\right)}{\mathrm{Li}_2\left(\pm e^q\right)}, \tag{1.11}$$

where the peak column density is given by $n_{2\mathrm{D},0}$ and Li_2 labelling the polylogarithm of the second order[KZ08]. The parameter $q = \mu/(k_\mathrm{B} T)$ is the logarithm of the fugacity and determines the shape of the atomic cloud. The function $f(x) = \frac{1+x}{x} \ln(1+x)$ smoothly interpolates between the limiting cases of large temperatures ($q \ll 0$) and the degenerate regime of low temperature ($q \gg 0$). The variable $R_i = \sqrt{2 k_\mathrm{B} T/(m\omega_i^2) \cdot f(\exp(q))}$ interpolates the size of the cloud between the thermal and degenerate regime, reproducing it's limiting cases of the gaussian radius σ_i in the thermal regime and the Fermi radius $R_{F,i} = \sqrt{2E_F/(m\omega_i^2)}$ for a quantum degenerate cloud.

Fermi gas characterisation

After the last steps of the evaporation in the optical dipole trap, an ensemble of 2.5×10^5 fermionic potassium-40 atoms is held in the trap. Applying the fit model given by Equation 1.11 to the column density profiles obtained by absorption imaging after a

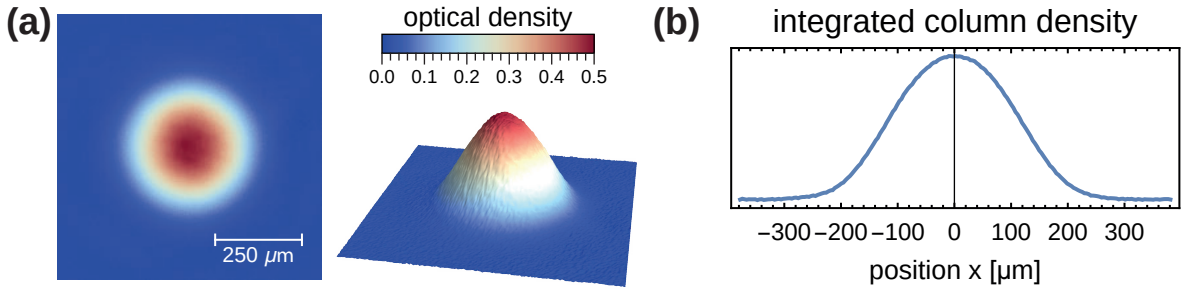

Figure 1.19: **Fermi gas image and density profile:(a)** Image of the DFG obtained after 19 ms of free ballistic expansion, averaged over 207 individual images. 3D representation is derived from the same data set. **(b)** doubly integrated column density $n_{1D}(x)$ of the DFG obtained from the dataset shown in (a) plotted against spatial coordinate x

variable ballistic expansion time t_{TOF} one is able to extract the shape parameter q and the size parameters R_i. Using the relationship

$$\frac{T}{T_F} = \left[-6\mathrm{Li}_3\left(-\exp(q)\right)\right]^{-1/3}, \tag{1.12}$$

the temperature in terms of the Fermi temperature T_F can be extracted and yields $T/T_F = 0.178 \pm 0.004$. From the fit parameters R_i the Fermi-Radius can be determined using $R_{F,i} = R_i/\sqrt{1+\omega_i^2 t_{TOF}^2}$, which gives rise to the physical size of the cloud held in the ODT. The Fermi-Radius in the ODT for a power of 160 mW is $R_{F,x} = R_{F,y} = (51.3 \pm 0.1)$ µm in the horizontal plane and $R_{F,z} = (12.6 \pm 0.1)$ µm in the vertical direction.

Figure 1.19 (a) visualises the Fermi gas held in the dipole trap and imaged after a free expansion time of 19 ms. Figure 1.19 (b) shows the column density profile $n_{1D}(x)$ after integration over the y-axis of the image.

As the particle number in the DFG depends on the initial particle number loaded into the dipole trap and ultimately on the particle number captured during the MOT phase, its dependency is characterised. Figure 1.20 (a) shows the particle number found in the DFG after a variable loading time of the potassium and rubidium MOT. In general, it can be seen that increasing the loading time of the potassium MOT leads to DFGs containing more atoms. With respect to the loading time of the rubidium MOT, two competing processes are observed: If more rubidium atoms are loaded in the beginning by increasing the loading time of the rubidium MOT, losses due to hetero-nuclear collisions throughout the experimental cycle increase. As a result, a slight reduction of the particle number is found if too many rubidium atoms were loaded initially. On the other hand, loading a larger number of rubidium atoms allows for more efficient sympathetic cooling

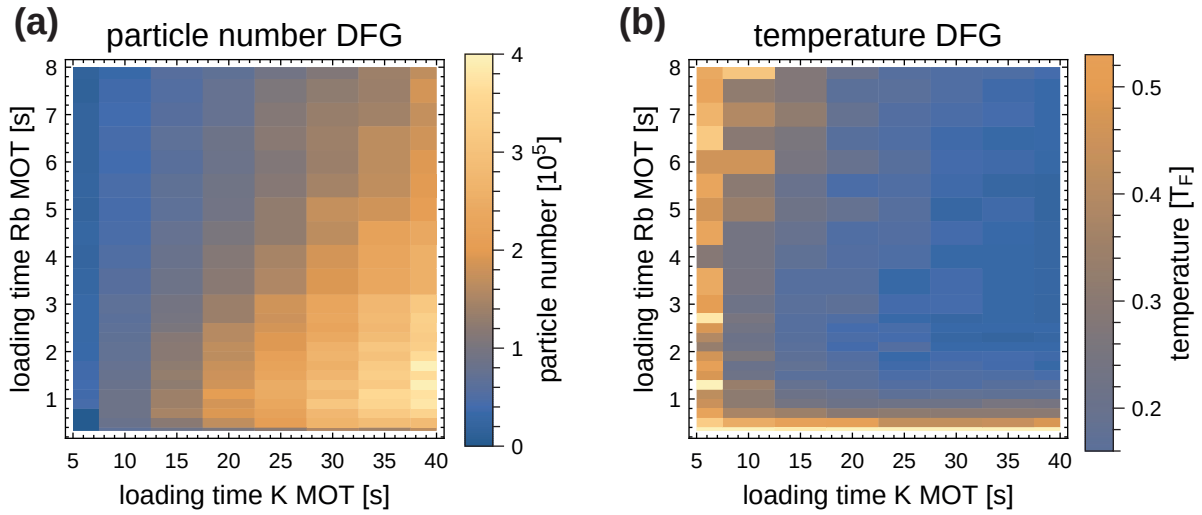

Figure 1.20: **Characterisation of the DFG against MOT loading times:**
(a) shows the particle number in the DFG for different MOT loading times of the potassium and rubidium MOT. The largest particle number of $(3.5 \pm 0.1) \times 10^5$ atoms in the DFG is observed after 40 s + 1.7 s of MOT loading.
(b) visualises the temperature of the DFG against the MOT loading durations. As the sympathetic cooling efficiency depends on the particle numbers, the temperatures after evaporation differ. The lowest temperature of $T/T_f = 0.178 \pm 0.004$ is achieved after 35 s + 2.3 s of MOT loading. Note that the region with the lowest temperatures is quite well aligned with the parameter sets resulting in the largest particle numbers.

enhanced via the *tilt trick*, which in turn determines the particle number left after the evaporation and the final temperature. Figure 1.20 (b) diagrams the temperature in terms of the Fermi temperature with respect to the MOT loading times and similar behaviour is observed. If the rubidium MOT loading time is below ≈1 s, the number of rubidium atoms is not large enough to allow for efficient sympathetic cooling and the final temperature settles around $T/T_F = 0.6$. Increasing the rubidium MOT loading duration above 1.5 s significantly decreases the temperature of the DFG, until it's minimum temperature of $T/T_F = 0.178 \pm 0.004$ is reached at 2.3 s MOT loading time for rubidium and 35 s for potassium respectively. The slight increase in the DFG temperature for rubidium MOT loading times beyond 3 s is not yet understood and needs further investigation. Comparing the particle number and temperature dependency of the DFG against the MOT loading durations side-by-side, one might note that the parameter region producing Fermi gases with the largest particle numbers also leads to the coldest samples produced in this experimental apparatus. Therefore it is not necessary to compromise between temperature or particle number in the DFG with regards to MOT loading times, as both optimal parameter sets align quite well.

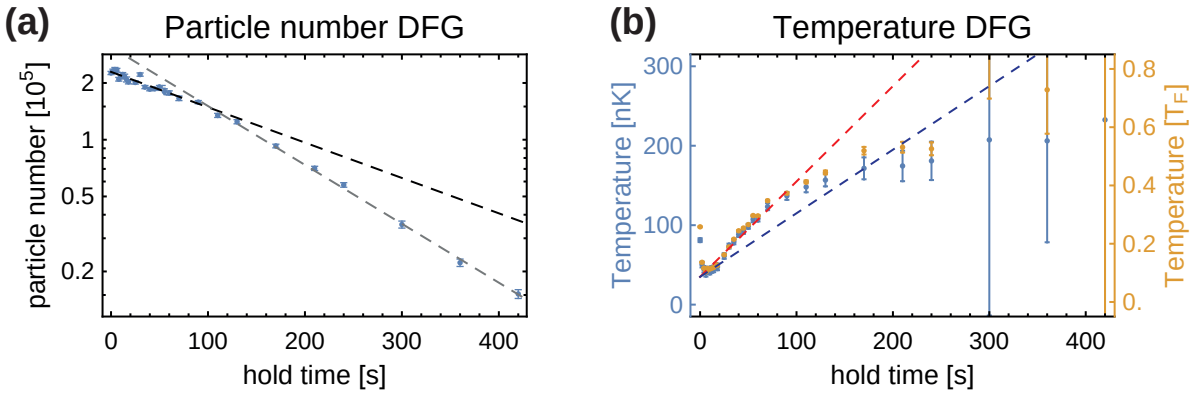

Figure 1.21: **Lifetime of the DFG:(a)** plots the particle number obtained by absorption imaging after a variable hold time in the ODT. The dashed lines indicate two different decay time scales, which are discussed in the main text. The black dashed line is interpreted as a decay due to collisions with the residual background gas; the grey dashed line a combined loss with added evaporation due to heating of the ODT. **(b)** shows the temperature of the DFG against hold time. The dark blue dashed line indicates heating with a calculated heating rate of 0.8 nK/s. Fitting a linear function to data points during the first 100 s a heating rate of 1.2 nK/s is obtained, which is visualised with the red dashed line.

The lifetime of the degenerate Fermi gas is measured by extracting the particle number from absorption images (see section 4.2 and section 4.3) taken after a variable hold time in the ODT. As shown in Figure 1.21 (a), the particle number shows an exponential decay with two different time scales (depicted with dashed grey and black lines), which are explained as follows: The initial slow decay with a time constant of $\tau_{\mathrm{K,DFG,initial}} = (223 \pm 12)\,\mathrm{s}$ (shown as dashed black) stems from collisions with hot background gas atoms and the transfer of kinetic energy onto a potassium atom from the DFG, which ultimately leads to the immediate removal of the atom from the trap. The second, faster decay channel with an exponential decay time of $\tau_{\mathrm{K,DFG,final}} = (139 \pm 3)\,\mathrm{s}$ (shown as dashed grey) is interpreted as an increased particle loss due to heating of the ODT, as discussed in the following paragraph.

Figure 1.21 (b) shows the DFG temperature dependency against holding time in the ODT. For holding times exceeding 20 s a significant increase in temperature is observed, which was studied in more detail. The heating rate $\dot{T}$ for a red-detuned optical dipole trap is calculated from the total trap depth U_{total} using

$$\dot{T} = \frac{2/3}{1+\kappa} T_{\mathrm{rec}} \frac{\Gamma}{\hbar|\Delta|} U_{\mathrm{total}}, \tag{1.13}$$

where $\kappa = 1$ is the scaling factor for a 3D harmonic trap[GWO99]. T_{rec} denotes the recoil temperature, Γ the natural linewidth and Δ the detuning between trapping light and the closest optical transition. For potassium-40 atoms trapped in the ODT, this results in a calculated heating rate of 0.8 nK/s for heating only associated with scattering photons from the trapping potential. Fitting a linear function to the first 100 s yields a heating rate of 1.2 nK/s, which is plausible because in any real experimental systems, parametric heating due to intensity fluctuations of the dipole trap beams occurs. After ≈100 s the absolute temperature of the atomic ensemble no longer increases, which is explained by an additional cooling process counteracting the heating caused by the optical dipole trap. This cooling is understood in terms of an increased evaporation rate of potassium-40 atoms, as the absolute temperature approaches ≈1/8 of the trap depth for potassium, and a significant fraction of the atoms leaves the trap potential. Therefore the additional loss channel seen in the particle number (Figure 1.21 (a)) after 100 s is caused by the onset of the evaporation due to the rising absolute temperature. One additional feature of the temperature curve can be observed during the first $5 - 8$ s, during which the temperature further decreases. This time scale is in good agreement with the lifetime of the BEC ($\tau_{\mathrm{Rb,BEC}} = 9.75$ s, [Eic18]) and is interpreted as continued sympathetic evaporative cooling of potassium via thermal rubidium atoms, which are expelled from the BEC due to heating. When the BEC is entirely evaporated, a constant (fitted) heating rate of 1.2 nK/s is observed. Using the relation $\tau \approx 10^{-8}/P$, where P denoted the vacuum background gas pressure in torr and τ the lifetime in s, it is possible to obtain a rough estimate of the background gas pressure in the appendix, which yields $(6.0 \pm 1.3) \times 10^{-11}$ mbar[Met99].

Creating a degenerate Fermi gas 2.5×10^5 potassium atoms at a temperature of $T/T_F = 0.178 \pm 0.004$ grants access to research with Fermi gases in optical lattices. With a lifetime of $\tau_{\mathrm{K,DFG,initial}} = (223 \pm 12)$ s, phenomena in an optical lattice can be investigated basically unaffected by the finite lifetime of the DFG, as every relevant time scale is exceeded by at least one order of magnitude.

1.8 Spin state preparation

Due to the fact, that a spin polarised ensemble of neutral fermionic atoms becomes non-interacting at very low temperatures[DeM+99, Sad+00], interparticle interaction has to be restored by creating a multi-component Fermi gas consisting of interacting hyperfine spin states or Zeeman sublevels with a finite s-wave scattering amplitude. A common choice for potassium-40 atoms is to create an incoherent mixture of $|F = 9/2, m_F = -9/2\rangle$ and

$|F = 9/2, m_F = -7/2\rangle$, as a technical feasible Feshbach resonance at 202.1 G can be used to tune the interaction over a large parameter space[GRJ03, RGJ04]. This section sketches the procedure used in this experimental apparatus to perform spin state manipulations of the potassium-40 DFG held in the ODT. As the realisation and implementation of these techniques were the key aspect of Jasper Riebesehl's master thesis, an in-depth discussion and characterisation can be found in [Rie21].

The internal spin degree of freedom can be addressed and manipulated using the magnetic dipole interaction, to couple different Zeeman sublevels within a given hyperfine states or by directly coupling different hyperfine states. This is usually done by applying pulses or sweeps of radio-frequency/microwave radiation onto an atomic sample subject to a precisely chosen homogeneous magnetic bias field. By choosing appropriate experimental protocols, the ensemble can either be transferred into a single final Zeeman sublevel, or coherent and incoherent mixtures of states can be created. In this experiment, a rapid adiabatic passage (abbr.: RAP) is used in conjunction with a Rabi pulse to transfer the DFG from its initially spin polarised state ($|F = 9/2, m_F = +9/2\rangle$) into an incoherent mixture of $|F = 9/2, m_F = -9/2\rangle$ and $|F = 9/2, m_F = -7/2\rangle$ as explained in the following.

RAP to invert ensemble into $|m_F = -9/2\rangle$

The working principle of the RAP is depicted in Figure 1.22 (a). After the sympathetic evaporative cooling of potassium-40 atoms in the ODT (see subsection 1.6.3), during which the spin polarisation is ensured with a finite magnetic bias field, all atoms occupy the $|F = 9/2, m_F = +9/2\rangle$ hyperfine spin state. Without a coupling radio-frequency, the gaps between level crossings are closed and the system is in eigenstate denoted by (1). The antenna field is then ramped up in 300 µs, such that neighbouring Zeeman sublevel are coupled. The emerging new eigenstates are shifted with respect to the unperturbed states and a sufficiently slow ramp up of the radio-frequency power ensures adiabaticity, such that the ensemble is smoothly transferred into the new perturbed eigenstate at large negative detuning (2). Subsequently the radio-frequency is adiabatically swept across the resonance in 5 ms to its final value at large positive detuning(3), which decomposition in terms of the unperturbed eigenstates is almost exclusively given by the inverted Zeeman sublevel. Afterwards the radio-frequency power is adiabatically ramped down to transfer the ensemble from the perturbed eigenstate back into the unperturbed pure Zeeman sublevel (4). Instead of changing the radio-frequency over time, it is possible to shift the position of the resonance for a fixed radio-frequency by ramping the magnetic bias

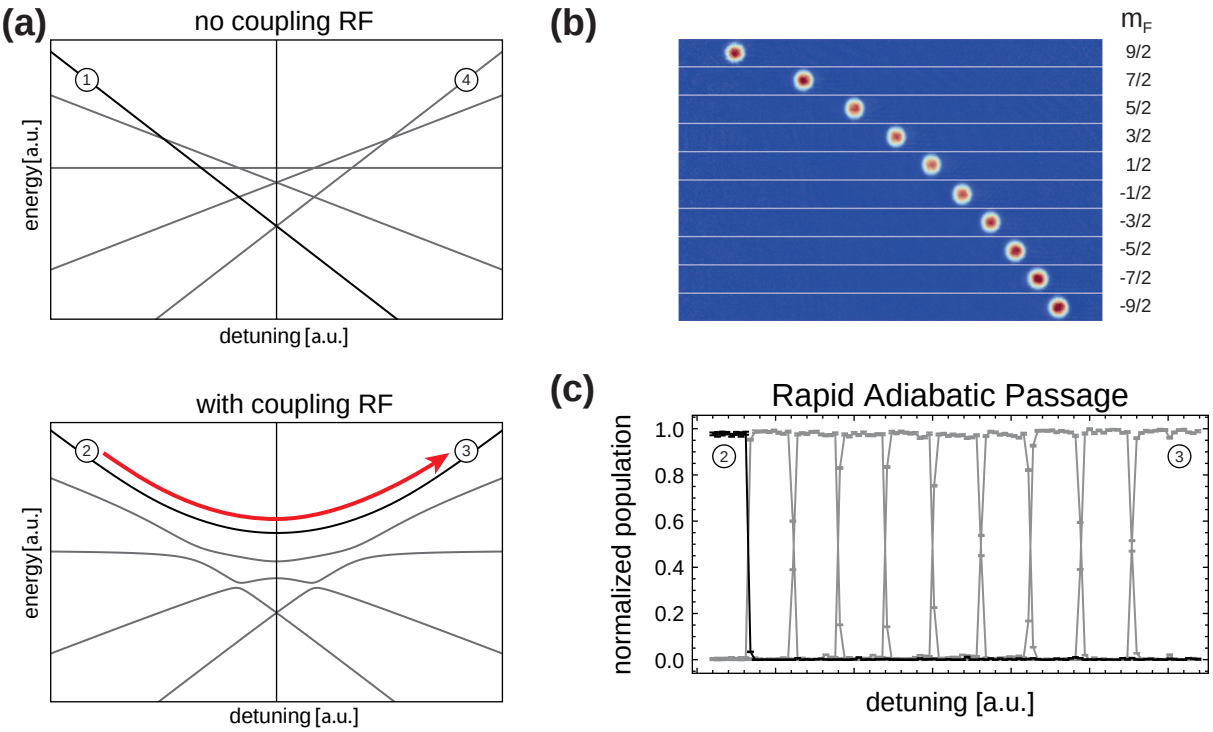

Figure 1.22: **Spin preparation - RAP:** **(a)** visualises the RAP process explained in the main text. For better visibility, the level scheme is plotted for the case of rubidium with only 5 levels instead of the 10 hyperfine states of potassium. **(b)** shows absorption images for different final detunings of the RAP, hyperfine state resolved with Stern-Gerlach separation during time-of-flight imaging. **(c)** shows the measured relative occupation of all 10 hyperfine states against the final detuning. As the ensemble is transferred across the resonance from (2) to (3), the relative occupation of the $|9/2, 9/2\rangle$ hyperfine state (black) drops to 0 and the ensemble is transferred into the $|9/2, -9/2\rangle$ hyperfine state.

field, which was chosen in this experimental protocol[26]. This procedure leads to the same qualitative behaviour, but circumvents specific technical caveats. Due to the limited bandwidth of an impedance matched antenna network, the radiated power depends on the applied radio-frequency, such that ramping the radio-frequency linearly over time leads to a Lorentzian shaped power of the RF field. By applying a fixed radio-frequency of 10.44 MHz, the available antenna power is kept at its maximal value and remains unchanged during the passage, which is ultimately performed by ramping the magnetic bias field ramp from 28.3 G to 37 G within 5 ms[Rie21]. The power of the radio-frequency throughout the RAP is chosen, such that on one hand the power broadening of the transitions is kept at a moderate level compared to the distance of neighbouring level crossings and on the other

26 One has to take care of the notion of negative and positive detuning, if the magnetic field is ramped. Depending of the state, the ramp direction has to be inverted.

hand the gaps are sufficiently large to prevent Landau-Zener transitions to other states. State selective imaging is achieved via Stern-Gerlach separation, where a magnetic field gradient is used to separate different Zeeman sublevels during the ballistic expansion. In Figure 1.22 (b), selected images for different final detuning of the RAP are shown and a full inversion of the sample is achieved. This is also seen in Figure 1.22 (c), where the relative occupation of different Zeeman sublevels is plotted against the final detuning. Here, the relative occupation was determined by fitting 2D Gaussian functions onto each individual Zeeman component and extracting the volume, which is directly proportional to the particle number and afterwards normalised. For a pure initial sample in the $|+9/2\rangle$ Zeeman sublevel, the transfer across the resonance is found to be very efficient and results in a final occupation of $(98.9 \pm 0.5)\,\%$ in the $|-9/2\rangle$ state with a residual occupation of $(0.52 \pm 0.01)\,\%$ in the $|-7/2\rangle$ state. The final slow ramp down instead of a sudden switch off of the antenna power is found to be crucial, to transfer the atoms into the unperturbed eigenstate[Rie21], which is in agreement with a theoretical analysis of the influence of the switching behaviour of the coupling in a RAP protocol[BM21].

Rabi pulse to prepare balanced mixture

Using the RAP protocol, the atomic ensemble was transferred into the $|m_F = -9/2\rangle$ state as explained above and the atoms can be prepared in a balanced incoherent mixture of $|m_F = -9/2\rangle$ and $|m_F = -7/2\rangle$ by applying an off-resonant Rabi-like pulse. Therefore the following protocol is used: After the magnetic field was swept to the final value of the RAP protocol and the radio-frequency power was ramped down within 300 µs, the magnetic bias field is ramped to 36 G. This magnetic field was chosen to be red-detuned to the $|m_F = -9/2\rangle \rightarrow |m_F = -7/2\rangle$-transition, which is done to reduce the coupling of the $|m_F = -7/2\rangle$ to its next neighbouring state $|m_F = -5/2\rangle$. In Figure 1.23 (a), the relative occupation of the relevant Zeeman sublevels is plotted against pulse duration. Due to the deliberately introduced detuning, the occupation of the $|m_F = -5/2\rangle$ state remains below 3.5 % for all pulse durations, such that the desired mixture ratio can be prepared by choosing the corresponding pulse duration, while keeping the residual occupation of the $|m_F = -5/2\rangle$ moderately low. In this case a balanced mixture is achieved after half a Rabi-cycle time. One additional, beneficial feature of the introduced detuning is the fact, that the preparation stability is experimentally found to be more stable. This might be a result of the fact, that the derivative of the population ratio with respect to the pulse duration is smaller for an carefully chosen, off-resonant π-pulse rather than a resonant $\pi/2$-pulse and hence fluctuations of the magnetic bias field or the power of the radio-frequency have a

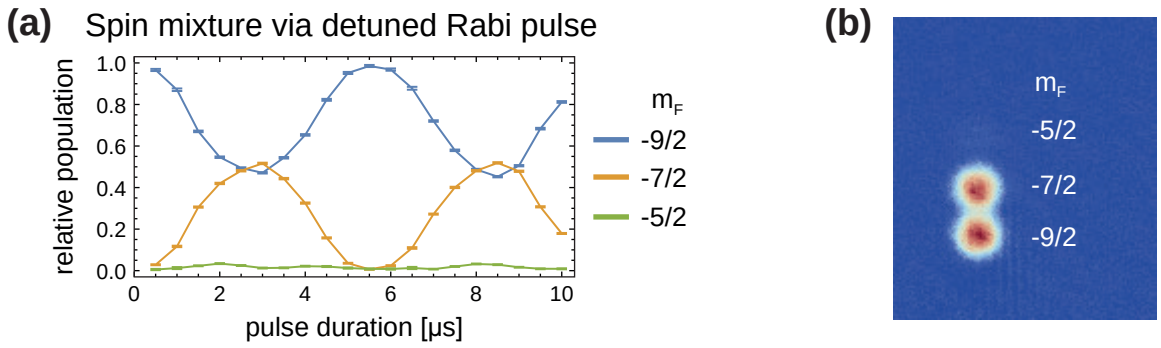

Figure 1.23: **Spin preparation - Rabi pulse:** **(a)** plots the relative occupation of different hyperfine states versus the Rabi pulse duration. Due to the slight overlap of the $|m_F = -9/2\rangle$ and $|m_F = -7/2\rangle$ components after Stern-Gerlach separation, the particle number is obtained by fitting a 2D Gaussian to all three Zeeman sublevels. **(b)** shows an absorption image for a Rabi pulse duration of 2.5 µs after Stern-Gerlach separation during time-of-flight imaging.

reduced impact. An absorption image of the balanced mixture is shown in Figure 1.23 (b). As using a Rabi-like pulse to create a spin mixture of fermionic atoms produces a coherent superposition of both involved states, scattering is still strongly suppressed, as all atoms occupy the same superposition state. Therefore an additional waiting time of 20 ms is introduced to ensure decoherence of the superposition state caused by collisions with the rubidium atoms and magnetic field fluctuations. Additional information about probing the coherence of the superposition with Ramsey spectroscopy can be found in [Rie21].

Using the scheme described above a balanced, incoherent mixture of the $|m_F = -9/2\rangle$ and $|m_F = -7/2\rangle$ is created and inter-particle interaction is restored resulting in a finite background scattering length of $a_{bg} = 176\, a_0$ for absent magnetic field between atoms in the two Zeeman sublevels[Reg05].

1.9 Summary

This chapter has presented the experimental setup for generating a Fermi gas. In particular, the extensions made to the apparatus that enable the cooling of potassium-40 atoms were discussed. A short summary is given in the following.

The implemented laser system for laser cooling of potassium-40 atoms allows stable operation of a potassium-40 MOT with around 5×10^7 trapped atoms. By simultaneously irradiating the D1 cooling light during the MOT phase, it was possible to increase the number of trapped potassium atoms by a factor of 3. Changing the spectroscopy setup to a modulation transfer spectroscopy scheme was an important step to ensure reproducibility

from day-to-day. The subsequent loading into a magnetic trap and the magnetic transport into the science cell is kept unaffected of these changes are remains in operation unchanged to the previous protocol[Büc17, Eic18].

RF-evaporation in the magnetic quadrupole trap, in which exclusively hot rubidium atoms are removed from the trap, allows the potassium to be efficiently precooled. It is then possible to load both atomic ensembles into an optical dipole trap and cool them via evaporation towards quantum degeneracy. Here, the fermionic species potassium-40 is cooled sympathetically via heteronuclear collisions with rubidium-87.

Incorporating the *tilt trick* into the evaporation process in the optical dipole trap (subsection 1.6.3) led to a significant increase in the particle number observed in the degenerate Fermi gas. This is done with a magnetic gradient, which tilts the trap potential and balances the gravity for potassium atoms, maximising the resulting trap potential depth. This made it possible to achieve the same minimum temperature of $T/T_F = 0.18$ with a tripling of the particle number to 2.5×10^5. Remarkably long DFG lifetimes of up to 220 s are observed.

Since 2016, it has been possible to generate a BEC at this experimental setup and to investigate physics in higher Bloch bands of an optical lattices. With the extensions to the experimental apparatus presented in this chapter, it is now also possible to investigate fermionic quantum gases in higher Bloch bands of an optical lattice. The following two chapters 2 and 3 report on the respective experimental investigations.

2 Fermions in higher bands of an optical lattice

This chapter describes the optical lattice used in the experimental apparatus and presents results of fermionic atoms in higher Bloch bands of a bipartite optical square lattice. The first section 2.1 discusses the optical lattice used in this experimental apparatus, while the second section 2.2 explains the experimental realisation. The following section 2.3 explains the excitation mechanism used to selectively populate higher bands of the optical lattice. In section 2.4 the experimentally realised occupation of higher bands is presented. In the final section 2.5 the results are summarised.

2.1 Bipartite optical square lattice

Optical lattices are formed by ultra cold atomic samples bound in periodic optical potentials. This section describes the optical lattice used in this experimental apparatus. For a more in-depth discussion of the lattice geometry used in this experimental apparatus see [Eic18, Büc17] as well as [Öls13, Wir13]. A comprehensive description of basic terms and definitions for the lattice geometry used in this experimental apparatus can be found in [Wir13].

A readily way to create periodic optical potentials is the usage of periodic intensity patterns resulting from interfering laser beams in conjunction with the AC stark shift. If a pair of two counter-propagating mode-matched Gaussian laser beams (see Equation 1.5) with same wavelength λ and parallel polarisation is used, the resulting intensity pattern $I(r, z)$ of the standing wave is time-independent. The resulting lattice potential $V_{\mathrm{lat}}(\mathbf{r})$ is then given by

$$V_{\mathrm{lat,1D}}(\mathbf{r}) = \widetilde{\alpha}\, I(\mathbf{r}) = \widetilde{\alpha}\, U_{0,1D}(\mathbf{r})\, \cos\Big(kz^2\Big), \tag{2.1}$$

where $\widetilde{\alpha}$ denotes the polarisability (cf. Equation 1.4) of the atoms, and $U_{0,1D}(\mathbf{r})$ labelling the lattice depth. For a laser red-detuned relative to the atomic transitions, this potential

becomes attractive and results in a force trapping the atoms in the local intensity maxima of the light field.

The two-dimensional lattice in this experimental apparatus is created by four laser beams arranged in two pairs of counter-propagating laser beams along the x- and y-axis. All four laser beams share the same wavenumber $k = 2\pi/\lambda$, waist and are linearly polarised along the z-direction, such that all four beams interfere and the resulting interference pattern is time-independent. The relative amplitudes of the laser beams are denoted by the anisotropy parameters ϵ_x, ϵ_y and η, where ϵ_i labels the intensity ratio of the counter-propagating beam pair and η the ratio between both pairs. For a given relative interference phase θ of the two standing waves, the resulting lattice potential $V_{\text{lat}}(\mathbf{r})$ is thus given by[27][Wir13, Eic18]

$$V_{\text{lat}}(\mathbf{r}) = -\frac{V_0}{4}\left| e^{-\left(y^2+z^2\right)/w_0^2}\left(e^{ikx} + \epsilon_x\, e^{-ikx}\right) + \eta\, e^{i\theta} e^{-\left(x^2+z^2\right)/w_0^2}\left(e^{iky} + \epsilon_y\, e^{-iky}\right)\right|^2. \quad (2.2)$$

For equal laser beam amplitudes, i.e. $(\epsilon_x, \epsilon_y, \eta) = (1, 1, 1)$, the potential simplifies to

$$\begin{aligned} V_{\text{lat}}(\mathbf{r}) = &- V_0 e^{-2z^2/w_0^2}\Big[e^{-2y^2/w_0^2}\cos(kx)^2 + e^{-2x^2/w_0^2}\cos(ky)^2 \\ &+ 2e^{-\left(x^2+y^2\right)/w_0^2}\cos(\theta)\cos(kx)\cos(ky)\Big], \end{aligned} \quad (2.3)$$

such that the resulting potential can be understood as a superposition of three lattices with a Gaussian envelope: Two standing-wave lattices along the x and y direction and one cross-dimensional interference term $\cos(kx)\cos(ky)$ scaling with $\cos(\theta)$. For distances from the centre much smaller than the beam waist w_0, the Gaussian envelope of the three lattices can be neglected and the potential from Equation 2.3 simplifies to

$$V_{\text{lat,centre}}(\mathbf{r}) = -V_0\left[\cos(kx)^2 + \cos(ky)^2 + 2\cos(\theta)\cos(kx)\cos(ky)\right]. \quad (2.4)$$

Figure 2.1 visualises the lattice potential given by Equation 2.4 for different selected values of the relative interference phase θ, also referred to as *time phase* in this thesis. For a *time phase* of $\theta = 0.5\,\pi$, both standing waves oscillate 90° out of phase and the cross-dimensional lattice term in Equation 2.4 vanishes. Values of $\theta \neq 0.5\,\pi$ lead to a

27 The Gouy phase and curvature of the Gaussian beams is neglected here, which is a good approximation for length scales much smaller than the Rayleigh length. For the lattice beam parameters of $\lambda_{latt} = 1064\,\text{nm}$ and $w_0 = 170\,\mu\text{m}$ the Rayleigh length is about 8.5 cm, while the atomic samples only covers around 30 µm.

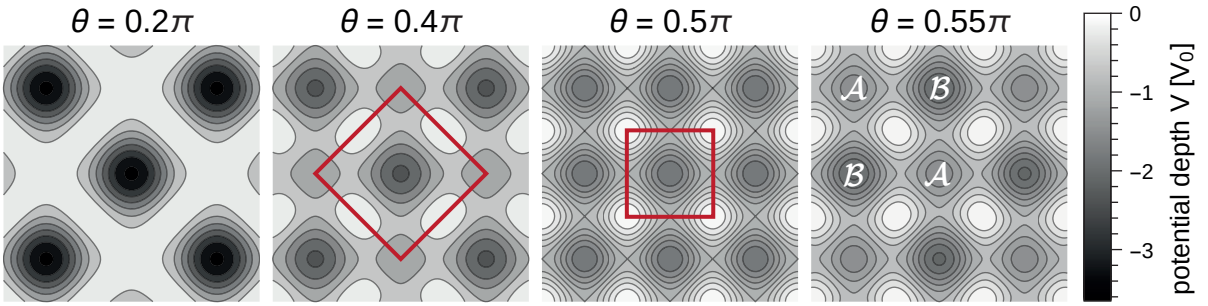

Figure 2.1: **Lattice potential for different *time phases* θ:** Cross-section through equipotential surfaces of the bipartite square lattice given by Equation 2.4 in the x-y-plane. The red squares indicate the Wigner-Seitz cell of the lattice, which is rotated by 45° and enlarged in the case of $\theta \neq 0.5\,\pi$ with respect to the Wigner-Seitz cell obtained for $\theta = 0.5\,\pi$.

non-vanishing cross-dimensional lattice term, which in turn results in the formation of a bipartite optical potential with two kinds of minima, arranged in a chequerboard-pattern. Throughout the thesis the definition of the lattice sites is as follows: For $\theta < 0.5\,\pi$ the potential features deeper $\mathcal{A}$- and shallower $\mathcal{B}$-sites, for $\theta > 0.5\,\pi$ the case is reversed and the potential possesses shallower $\mathcal{A}$-sites and deeper $\mathcal{B}$-sites. Calculating the potential energy difference $\Delta V = V_{lat}(\mathcal{A}) - V_{lat}(\mathcal{B})$ of both classes of minima yields

$$\Delta V(\theta) = -V_0\,(1+\epsilon_x)\,(1+\epsilon_y)\,\eta\cos(\theta). \tag{2.5}$$

Utilising the *time phase* it is thus possible to tune the relative depth of $\mathcal{A}$ and $\mathcal{B}$-sites, which is used to excite atoms into higher bands (see section 2.3).

Plotting the equipotential surfaces of the lattice potential given by Equation 2.2 against the x and z-direction reveals the tubular shape of the local minima. If in addition to the lattice potential the gravitational potential along the z-direction is taken into account, these local minima vanish below a given threshold lattice depth and the atoms are no longer trappable[28]. For this reason an additional confining potential has to be used, which holds the atoms against the gravitational potential as well as confines the atoms in the centre of the optical lattice potential. In this case an optical dipole trap is used (see section 1.6 and section 2.2) to provide additional confinement for all lattice depths.

In order to describe the motion of a particle in presence of a periodic potential, one has to solve the corresponding Schrödinger equation. According to Bloch's theorem[Blo29],

28 ab-initio calculation show a threshold lattice depth of $15E_{rec,K}$ (potassium-40 atoms) and $66E_{rec,Rb}$ (Rubidium-87 atoms) for solely trapping inside the lattice potential and holding the respective atomic species against the gravitational potential. The strong difference for both species stems from their different masses.

these eigenfunctions $\psi(\mathbf{r})$ take the form of so-called *Bloch functions* and can be expressed as the product of a plane wave $\exp(i\mathbf{qr})$ and a periodic function $u_{\mathbf{q}}(\mathbf{r})$ with the same periodicity as the lattice structure, where q denotes the quasi momentum. Since the same theoretical description is used to represent electron motion in a solid, it is possible to use concepts from solid state theory to describe atomic motion and dynamics within optical lattices. Since textbooks on solid state physics introduce the corresponding theoretical concepts and definitions, we will only refer to them here[Kit04, Ash76, Czy07].

The following theses present a comprehensive overview of the theoretical description of a bipartite optical square lattice, as used in this experimental apparatus. An extensive theoretical framework for describing interaction-free particles inside the bipartite optical square lattice potential used in this experimental apparatus can be found in [Wir13]. In addition, a mean-field description of a Bose-Einstein condensate with finite interaction inside this lattice geometry is given. Describing dynamics of a Bose-Einstein condensate in higher bands of the identical lattice geometry can be done by following [Roc20]. The calculation of the band structure in 2D assuming periodic boundary conditions can be performed as outlined in [Eic18]. For this reason, no further theoretical description of the lattice geometry used is given in this thesis, but only fermion-specific theory is added where necessary. This includes a calculation of the band structure in 1D including the harmonic confinement (see section 2.4).

2.2 Optical lattice in the set-up

This section focusses on the experimental realisation of the lattice potential given by Equation 2.2. In subsection 2.2.1 the optomechanical setup of the lattice is explained. Additionally, the routine to adjust the lattice and spatially overlap it with the dipole trap is sketched and the stabilisation of the lattice parameters is outlined. The calibration procedure of all physical quantities of the lattice is briefly summarised in subsection 2.2.2.

As this experimental lattice setup was first assembled by Raphael Eichberger and explored with Bose-Einstein condensates, an in-depth discussion of the experimental realisation of the lattice in this experimental apparatus can be found in [Eic18]. Additionally information is provided in [Büc17].

2.2.1 Experimental realisation

The experimental realisation of the lattice potential given by Equation 2.2 requires the superposition of two pairs of orthogonal standing waves. The necessary optical access is readily available in the appendix of the science cell.

Forming a time-independent interference pattern of multiple laser beams requires a fixed relative phase between those laser beams. If one of the beams involved differs slightly in frequency, the relative phase of the beams electric field change over time, the resulting interference pattern is no longer stationary and the resulting travelling wave moves with a velocity proportional to the difference frequency. Therefore a single laser beam is used to create all four lattice beams, which is done in the following way: A single laser beam is provided by an optical fibre, split into four independent beams each of which is guided via standard optical components onto the position of the atomic cloud. This is done by combining a Michelson interferometer with Sagnac-loops acting as retro-reflectors, as illustrated in Figure 2.2.

The optical lattice is realised as a Michelson-Sagnac interferometer, where a classical Michelson interferometer is used as a basis. Instead of using two retro-reflecting mirrors, as in a conventional Michelson interferometer, two Sagnac loops reflect the light back onto the Michelson beam splitter. In case of perfectly mode-matched beams within a Sagnac-loop, the output port of the Sagnac beam splitter becomes completely dark and the Sagnac loop acts as a retro-reflector. Using two such loops as retro-reflectors, the Michelson interferometer is completed. By matching the linear polarisation of counter-propagating beams within each Sagnac-loop, an optical standing wave within each loop is formed. If the two loops are arranged, such that the optical standing waves provide a crossing point inside the appendix of the glass cell and by choosing the linear polarisation for all four beams to be parallel along the z-direction, cross-dimensional interference between both standing waves is enabled. Here one optical standing wave defines the x-axis of the lattice coordinate system and the other standing wave encloses a small angle ζ with the y-axis, which is unavoidable in the experiment. Adjusting the relative optical path lengths of both Michelson interferometer arms allows to introduce an additional phase shift between both standing waves inside the Sagnac loops. With the relative interference phase θ as an experimentally accessible and tunable degree of freedom, the optical potential from Equation 2.2 is realised in the experiment.

In Figure 2.2 the optomechanical setup of the Michelson-Sagnac interferometer is shown, which is assembled on the same aluminium *lattice board* as the ODT. The beam height of the lattice and ODT is 25 mm above the board and all components are glued to the

surface. As residual mechanical vibrations caused by the cooling water and air condition result in a pointing instability of the laser beams of the optical lattice and ODT, additional lead plates were installed to damp those vibrations. Multiple of these lead plates are glued below the actual lattice board shown in Figure 2.2 to increase the weight, which resulted in a shift of the mechanical eigenfrequencies towards higher frequencies as well as in a reduced amplitude. Unlike the dipole trap with its $155 \times 40\,\mu m$ beam waists, the lattice beams feature a symmetrical beam profile with a $170 \times 170\,\mu m$ in each beam. This beam diameter was chosen as a compromise because it keeps the required optical powers within an experimentally manageable range and at the same time the effects of the harmonic envelope of the lattice potential across the size of the atomic ensemble are small. In order to avoid unwanted reflections of the lattice beams resulting in additional reflexes creating optical superlattices at the position of the atoms, two counter-measures have been

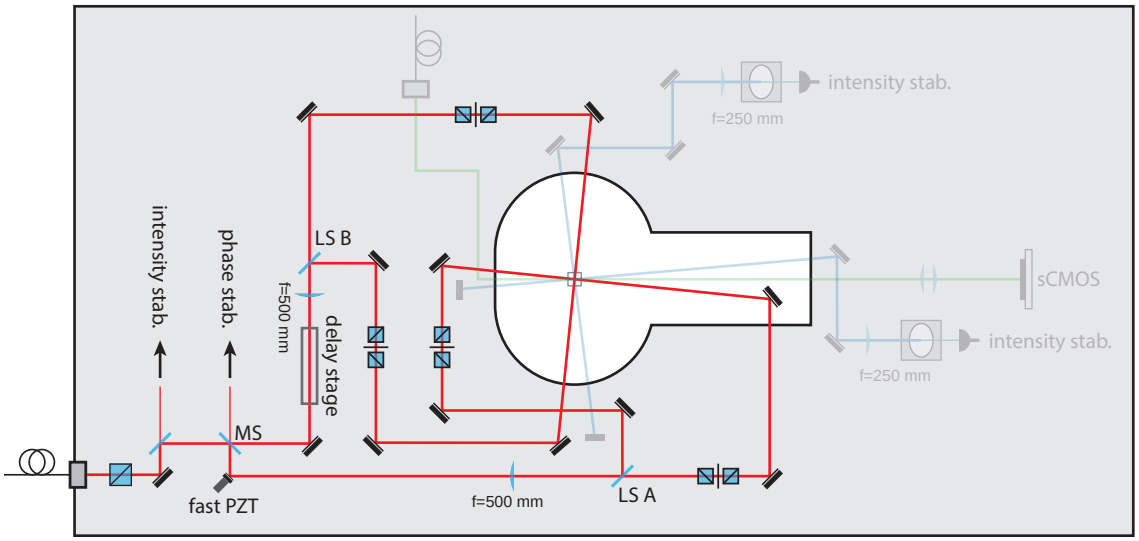

Figure 2.2: **simplified scheme of the *lattice board* - optical lattice:** The lattice beam is split into two power balanced beams at the Michelson beam splitter (MS), focussed with two +500 mm lenses and guided to both loop beam splitters (LS A and LS B). The standing waves formed inside the Sagnac-loops interfere inside the appendix of the glass cell and create the optical potential for the optical lattice. Within each beam inside the Sagnac-loops an optical attenuator stage consisting of two polarising beam splitters and a half-wave plate is used to individually tune the relative intensities of all beams. The piezo-ceramic (fast PZT) with a small mirror attached is used for fast adjustment of the time phase θ, while a second piezo-ceramic inside the delay stage is used for slow adjustment of the time phase, featuring a lower stabilisation bandwidth but larger travel distance. To hold the atoms against gravity, the ODT is overlapped at the crossing point of the interferometer (ODT setup is greyed out, for details see Figure 1.15).

employed: The first is the wedged nature of the glass substrate of the appendix of the glass cell, where the inner surface of the cell encloses a 2° angle to the outer surface; the second is the chosen angle of incidence of 15° of the lattice beam onto the outer surface, such that reflexes arise at even larger angles.

Laser system

Creating time-independent interference patterns requires laser sources with a narrow spectral linewidth and low intensity noise. Therefore the lattice laser light is taken from a solid state laser[29] with 25 W output power at $\lambda_{lat} = 1064\,\text{nm}$ and a specified linewidth of 100 kHz. The laser beam with a wavelength of λ_{stab}= 1083 nm used to stabilise the time phase θ is taken from an ECDL[30]. Both lasers are then diffracted with individual AOMs, frequency shifted, superimposed and subsequently coupled into a fibre[31]. Both AOMs are used for intensity stabilisation of the corresponding beam as well as in the case of the lattice beam the fast switching. Additionally one TTL-controlled mechanical shutter is used to block the lattice beam entirely during the rest of the experimental cycle. With this arrangement a lattice beam of up to 1.8 W at λ_{lat}= 1064 nm and a stabilisation beam with ≈100 µW at λ_{stab}= 1083 nm is provided and transferred to the experiment table and the optomechanical setup of the optical lattice shown in Figure 2.2. A calculation of the maximum lattice depth yields $V_{0,max,K} = 17.2\,\text{E}_{\text{rec,K}}$ for potassium atoms and $V_{0,max,Rb} = 41.7\,\text{E}_{\text{rec,Rb}}$ for rubidium atoms.

Stabilisation of the lattice - time phase θ and intensity

As the passive stability of the optical path lengths inside the interferometric setup is not sufficient and mechanical vibration of the lattice board result in a relative phase shift on the order of 2π within 500 ms between the both optical standing waves, the optical path length has to be actively stabilised. This is done by actively stabilising the Michelson interference fringe signal recorded at the output port of the Michelson beamsplitter (labeled MS in Figure 2.2) with a PID control loop.

Because the amplitude of the interference fringe signal depends on the total power of the lattice beam, it is not possible to use the Michelson signal of the lattice laser at $\lambda_{lat} = 1064\,\text{nm}$ directly as an input of the feedback loop. Instead an additional stabilisation laser at $\lambda_{stab} = 1083\,\text{nm}$ is used, which remains active and intensity stabilised at 100 µW

29 Mephisto MOPA from coherent
30 DLPro from Toptica
31 PMC-E-980-8.5-NA009-3-APC.EC-300-P from Schäfter + Kirchhoff

throughout the experimental cycle. Separating the Michelson signals of the lattice beam and the stabilisation beam behind the Michelson beamsplitter via optical interference edge filters allows to use the Michelson signal of the stabilisation laser as an input signal for the time phase stabilisation.

The relative optical path length difference of both arms of the Michelson interferometer is adjusted using two piezo ceramics, which move optical components inside the lattice setup. The first piezo with a large travel distance of 25 µm is included in the delay stage and moves a prism pair resulting in twice its travel distance in optical path length shift. Due to its low resonance frequency it provides stabilisation of the time phase with a bandwidth of 3 – 4 kHz but allows to compensate even larger drifts of the optical path length caused for example by slight temperature drifts over the course of several hours. For faster adjustment of the the interference phase a second piezo (labeled fast piezo in Figure 2.2) is used to move a small mirror and change the optical path lengths with a bandwidth of up to 30 kHz.

The interference fringe signal is recorded with a photodiode and used as an input signal for two PID controller[32]. The output of the two controllers is then amplified via two high-voltage amplifiers and used to adjust both piezo ceramics, such that the interference fringe signal corresponds to a setpoint entered via the experiment control software(see subsection 4.1.2). The PID controller settings are adjusted, such that the step response after an nearly instantaneous (<1 µs) change of the setpoint corresponding to a change of $\theta = 0.4\,\pi \rightarrow 0.53\,\pi$ features a rise time of <40 µs. This response time allows to change the time phase θ and thus the optical lattice potential faster than all other physical relevant time scales in the experiment, such that this can be used to address higher bands with the excitation scheme used in this experiment (see section 2.3). The achieved precision of $2 \times 10^{-3}\,\pi$ of the time phase θ is sufficient to use the lattice setup presented here to realise the optical potential given by Equation 2.2. Due to the wavelength difference of the stabilisation and the lattice laser, the actual realised and stabilised relative interference phase θ has to be measured spectroscopically with the atomic cloud as explained in subsection 2.2.2.

The intensity of the lattice beam is actively stabilised. Due to the fact, that the interference fringe signal of the stabilisation laser is used as an input signal for the time phase stabilisation of the lattice, its intensity has to be stabilised as well. Both stabilisations use a monitoring beam behind a 99 % reflectivity mirror, which is then separated with an interference edge filter, as an input signal for the corresponding feedback loop. In both

32 LaseLock from TEM

cases a PID controller is used to adjust the RF power for the AOM inside the laser system, such that the measured power behind the optical fibre is stabilised to the setpoint defined via the experiment control software.

Alignment of the lattice

To align the optical lattice, the beam path of all lattice beams has be adjusted, such that their mutual crossing point coincides with the position of the atomic samples held in the optical dipole trap. Therefore it is necessary to ensure that both pairs of counter-propagating beams are mode matched, their foci are aligned and the angle $90° + \zeta$ between both beams is as close as possible to 90°.

Due to the small optical densities of the DFG compared to the BEC, a more reliable and, caused by the shorter experiment cycle time, faster alignment procedure is achieved by observing the BEC instead of the DFG directly. The beam alignment procedure of the lattice beams is then performed as follows: The BEC is held in the dipole trap at an optical power 160 mW, which is the optical power used as the endpoint of the evaporation ramp. Then one of the four lattice beams is switched on with its counter-propagating and all other beams blocked with mechanical shutters. If the lattice beam axis is not aligned with the minimum position of the dipole trap, this causes an asymmetrical deformation of the total potential, such that the resulting force starts an oscillation of the BEC in the combined trap potential. If the lattice beam is switched on for a duration of $T/4$, where $T = 2\pi/\omega_i$ is the trap period of the dipole trap, the largest momentum transfer onto the atoms is observed, which is converted into a position deviation via time-of-flight imaging. Minimising the position offset caused by the lattice beam is thus sufficient to align the lattice beam to the dipole trap minimum position for the BEC. The lattice beam path is then adjusted with a piezo driven mirror mount (not the fast piezo used for time phase stabilisation, but mirror mounts inside the lattice loop), such that the position offset caused by a misaligned lattice beam is minimised. It is then possible to use the first beam, which was aligned to the atomic position as described above, as a reference beam and overlap the counter-propagating laser beam. This is done by observing the output port of the Sagnac-loop with a photodiode and minimising the optical power, while simultaneously maximising the power coupled back into the optical fibre. With this procedure all four lattice beams are aligned with the atomic position. So far there is no method available to measure the angle of the optical standing wave pairs directly. One method to use Bose-condensed atoms in the second band as a precise measurement of the angle ζ is presented in [Eic18, Hac+21].

Because the gravitational sag for potassium and rubidium atoms differ by 8.8 µm for an optical power of 160 mW used during alignment, the position of the lattice is aligned to the BEC centre position with the procedure described above and thus slightly shifted relative to the DFG rest position. Due to the large beam waists of the lattice beam of 170 µm this effect is negligible and no influence of this offset was observed during all measurements presented in this thesis.

Additionally to the beam path alignment, the relative intensities $\epsilon_x, \epsilon_y, \eta$ have to be adjusted via the optical attenuators inserted in each individual lattice beam, which is done by adjusting the intensities and performing the calibration of the lattice depth as explained in subsection 2.2.2. Repeating this procedure iteratively allows to match the relative intensities with a precision of $<1\,\%$. Because it is possible to counter-act the effect of a non-zero angle ζ with a defined mismatch of the lattice beam intensities they are chosen, such that the band structure of the second band features two degenerate minima at the X-points, as it is expected for a perfectly C4-symmetrical optical lattice potential.

More details on the experimental realisation of the lattice as well as calculations, characterisation of the lattice beam parameters and considerations about the lattice angle can be found in [Eic18].

2.2.2 Calibration of the lattice parameters

To connect experimental quantities with the physical relevant quantities of the lattice potential, a calibration procedure has to be performed. This subsection describes the calibration of the lattice depth and the time phase θ.

Calibration of the lattice depth V_0

To obtain the lattice potential depth V_0, it is necessary to measure the optical potential depth created by a given, experimentally measured, optical power. Although recently more elaborate and precise lattice depth calibration methods have been demonstrated[Zho+18], up to now the lattice depth is calibrated via parametric heating [Fri+98].

This method relies on measuring the resonance frequency, at which a resonant excitation to excited harmonic oscillator states can be driven by sinusoidally modulating the lattice depth. Therefore the total lattice power is ramped up to a given optical power within 150 ms and subsequently modulated by 1 % for 50 ms. When the modulation frequency is scanned across the resonance for a driven transition from the first to higher bands, a

distinct drop in the observed peak density of the 0 ħk-mode can be identified. A comparison with a 1D band structure calculation yields the realised optical potential depth V_0.

Because the optical densities of the DFG are on the order of 0.3 or lower even without parametric heating, a more reliable lattice depth calibration procedure is obtained by calibrating the lattice depth $V_{0,Rb}$ for rubidium-87 as explained above and calculate the corresponding lattice depth $V_{0,K}$ observed by the potassium atoms. Expressing both lattice depths $V_{0,Rb/K}$ in the respective recoil energies, the lattice depth $V_{0,K}$ for potassium-40 atoms is given by

$$V_{0,K} = 0.899 \cdot 0.459\,\mathrm{V_{0,Rb}} = 0.412641\,\mathrm{V_{0,Rb}}. \tag{2.6}$$

The two numeric factors in the first equality stem from differing species-dependent properties: The first factor is caused by the different polarisabilities of both atomic species and the second factor is a consequence of the difference in mass, resulting in different recoil energies.

Calibration of the interference time phase θ

The phase stabilisation of the lattice setup is carried out via the stabilisation laser with a wavelength of 1083 nm. However, since the relative interference phase of the lattice laser is only independent of the wavelength at the white light point of the interferometer, the interference phase of the lattice laser with a wavelength of 1064 nm does not necessarily correspond to that of the stabilisation laser. Since the interference phase of the two standing waves in the appendix cannot be measured directly, it is necessary to determine it spectroscopically with the atoms.

As shown in Figure 2.1, the realised lattice potential changes its periodicity for a time phase of $\theta = 0.5\,\pi$ indicated by the rotated and smaller Wigner-Seitz cell in this configuration. When a bosonic superfluid is prepared at a fixed interference phase θ of the lattice beams, the recorded momentum specta after time-of-flight imaging carry information about the realised potential. By tuning the stabilisation setpoint voltage of the time phase stabilisation, it is possible to identify the corresponding voltage for a $\theta = 0.5\,\pi$ interference phase of the lattice laser. In Figure 2.3, measured momentum spectra for two different realised fixed time phases are shown, and compared to simulated momentum spectra. The image on the right is used to identify the $\theta = 0.5\,\pi$-voltage setpoint for the stabilisation. Measuring the minimal and maximal interference signal obtained, while scanning the delay stage, allows to calculate realised time phases $\theta \neq 0.5\,\pi$[Eic18, Wir13].

By doing so, the time phase on the left is identified to realise a time phase of $\theta = 0.48\,\pi$, which is in good agreement with the simulated momentum spectra.

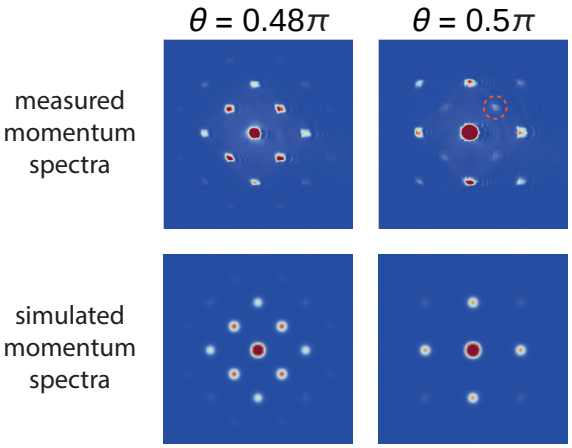

Figure 2.3: **Momentum spectra used for time phase calibration:** Comparison of measured and simulated momentum spectra for a bosonic superfluid prepared in the first band of the optical lattice potential for a fixed time phase θ. The disappearance of the $(\pm 1, \pm 1)$ $\hbar$k-mode (indicated in the orange dashed circle) in the case of $\theta = 0.5\,\pi$ is used to identify the $\pi/2$-voltage of the time phase stabilisation.

2.3 Loading of the optical lattice and excitation scheme

This section describes the loading procedure of the atoms into the lowest band of the optical lattice (subsection 2.3.1). In subsection 2.3.2 the excitation mechanism for selectively exciting higher bands of the optical lattice is described.

2.3.1 loading of the lattice

After the DFG is prepared in the dipole trap (see subsection 1.6.3) it is possible to apply the lattice potential created by the previously introduced optomechanical setup. This loading of the atomic ensemble into the optical lattice has to be performed such that the heating of the ensemble remains moderate and the system remains in its ground state, which means, that the loading has to be performed adiabatically[BF28, BM21].

Adiabaticity of the loading procedure implies, that the ramp up duration of the lattice optical power is slow compared to the tunnelling time[Den+02]. In presence of an external

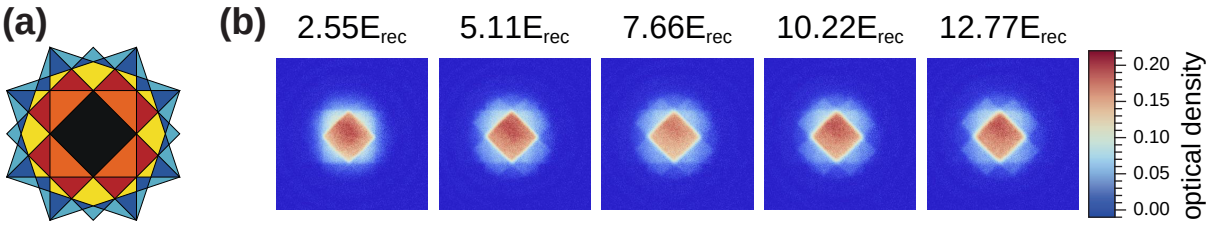

Figure 2.4: **Loading of the DFG into the lattice potential: (a)** visualises the first six Brillouin zones of the 2D square lattice. **(b)** Band mapping images of the DFG after transfer into the optical lattice via a linear increase to the final lattice depth in 150 ms.

harmonic confining potential, this adiabaticity criterion is more complicated. A discussion can be found in [Rom09, Ger+07].

In our experimental apparatus, the loading of the lattice is done by linearly increasing the optical power of the lattice beams in the x-y-plane within 150 ms to a lattice depth of $V_0 = 4-15\,\mathrm{E_{rec,K}}$. This ramp up duration has been empirically found observing the behaviour of the BEC, when loaded into the optical lattice and no excitation of the BEC is measured[33]. As the tunnelling times of potassium-40 are smaller compared to those obtained for rubidium-87, it is expected that this ramp up time exceeds the duration necessary to ensure adiabaticity throughout the loading procedure for the potassium-40 atoms into the optical lattice.

In Figure 2.4 (b), band mapping images for different final lattice depths V_0 are shown. A comparison to the Brillouin zones of the 2D square lattice (plotted in (a)) shows that for all lattice depths a finite fraction of ≈35 % of all atoms is not found in the lowest band, but rather occupies higher bands. Reducing the ramp up time of the lattice did not reduce the fraction of atoms observed in the second Brillouin zone, such that it is suspected, that the total number of atoms loaded to the lattice exceeds the number of states available in the first band (cf. discussion about halos in subsection 2.4.1).

Remark: During the loading of a BEC into our lattice geometry, an extremely useful experimental trick can be applied. Reducing the optical power of the dipole trap depth by a few percent during the increase of the lattice potential allows for a second evaporation, counteracting unwanted residual heating caused by the lattice ramp-up. Including this

33 We analysed the temperature of the BEC after being loaded into the optical lattice with an initial ramp up time of t_{ramp}, a variable hold time and a ramp down time of t_{ramp}. The observed temperature remained unchanged within the uncertainty of the measurement, which might be due to an additional loss and the corresponding evaporation. As long as the Fermi gas stays spatially overlapped to the BEC, thermal contact should be preserved and the fermionic ensemble should remain at its initial temperature as well during the loading procedure.

step in the experimental sequence, the visibility of Bragg peaks observed if a bosonic superfluid is loaded into an optical lattice of $\approx 7\,\mathrm{E_{rec,Rb}}$ was nearly doubled and the 1/e-time of the coherence measured via the width of the Bragg peaks was nearly trippled. This simple experimental trick could be used to lower the temperature of ensembles loaded into the optical lattice substantially, as long as thermalisation is ensured. As this trick was discovered after all measurement presented in this thesis were performed, all data sets shown here are taken without this second evaporation step. Further investigation of this additional evaporation step with fermionic samples is also considered.

2.3.2 Excitation scheme

The excitation scheme to populate higher bands of an optical square lattice presented here was developed at another experimental setup in our group [Öls13, Wir13] and implemented in this experimental apparatus. Like in the other experimental setup, this method has been used to transfer coherent ultracold bosonic ensembles into higher band, realising excitations up to the 22^{nd} band[Eic18, Büc17]. This section describes the method implemented to transfer potassium-40 atoms into higher bands of the bipartite optical square lattice.

The excitation scheme is based on the ability to change the potential depth difference ΔV of neighbouring lattice sites faster than the tunnelling rates. According to the adiabatic theorem this rapid change of the Hamiltonian leads to a projection onto the new eigenstates rather than keeping the ground state populated at all times[BF28, Ger18]. In Figure 2.5 the four-step excitation scheme is sketched and explained in the following:

Step 1: Before the lattice is ramped up, the initial time phase θ_i of the lattice is adjusted to a value of $\theta_i < 0.5\pi$. If subsequently the lattice is ramped up adiabatically, no excitation of the atomic ensemble is observed and the system is slowly transferred to its new ground state. This state is given by the Bloch function of the first band at the Γ-point, which can be approximated by local s-orbitals in the deep $\mathcal{A}$-sites, while the occupation of the $\mathcal{B}$-sites is negligible. In our case, the time phase is adjusted to a value of $\theta_i = 0.4\pi$ and subsequently the lattice optical power is ramped up in 150 ms to the desired lattice depth.

Step 2: Next, the time phase θ is quenched faster than the tunnelling time to a value of $\theta > 0.5\,\pi$, such that the potential depth difference ΔV (cf. Equation 2.5) changes its sign and the previously deeper $\mathcal{A}$-sites are now shallower than the $\mathcal{B}$-sites. Due to the fact, that this lattice potential change is faster than the tunnelling time, no redistribution to other lattice sites takes place and instead a projection of the

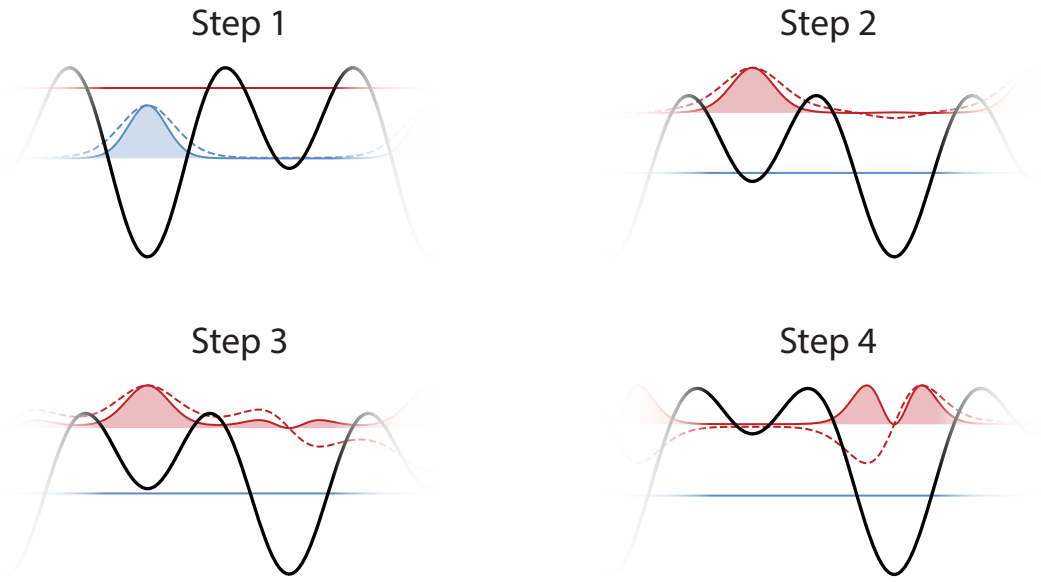

Figure 2.5: **Excitation Scheme:** Schematic illustration of the excitation protocol to higher bands in the optical lattice. The black curve visualises the bipartite potential as well as the first(blue) and second(red) band. For the populated band the absolute square of the Bloch function (solid filled line) and the real part(dashed) of the Bloch function is plotted. For an explanation of the four steps, see main text.

initial state in the first band onto the new eigenstates is observed. Because the initial distribution exclusively populated the $\mathcal{A}$-sites, this projection favours final Bloch states, which also show large amplitudes on these sites, which is the case for Bloch functions with higher band indices. Hence, the exact configuration of this non-adiabatic projection (in the following also called *quench*) regarding time scales, initial and final time phases θ and lattice depths V_0 define the transfer efficiency to higher bands, as well as their selectivity. The usual 1/e-quench times are chosen in the range of $30-100\,\mu s$, depending on the desired final state[34].

Step 3: Due to the fact, that the system is not in thermal equilibrium right after the quench, a thermalisation into the new many-body ground state takes place, as long the entropy introduced by the quench can be dumped in other available states. In the case of the BEC this thermalisation takes places via a pronounced particle loss along the z-direction (cf. remark in subsection 2.3.1) and the atoms condense at the

34 The settling time of the time phase stabilisation has to be adjusted, such that the fidelity of the transfer to the desired state is maximised. Thus, for an optimised experimental protocol to populate the desired final state, it might be necessary to adjust the PID controller settings, such that residual ringing of the time phase after the quench is minimised and the settling time is shorter than the tunnelling time.

band minima[35]. For this thermalisation a typical hold time of 5 – 250 ms is inserted after the quench, which results in maximal coherence for the BEC after 200 ms.

Step 4: After the thermalisation into the many-body ground state, it is possible to tune the relative occupation of the involved orbitals by adiabatically changing the time phase θ to its final value θ_f. This is typically performed in 5 – 50 ms. Due to the vanishing scattering cross section of spin polarised fermions at low temperatures this allows us to slowly vary the time phase across band crossings and access a variety of different final states (cf. Figure 2.11).

The band index selectivity of the quench process is readily understood by calculating the 2D band structure in dependence of the time phase θ, which is plotted in Figure 2.6. If the quench is performed, such that the energy difference to adjacent bands for the final time phase θ_f is maximised, the highest band selectivity is achieved. This is possible for bands with band index $n = 1 + N(N+1)/2$ with $N \in \{1, 2, 3, \dots\}$ in our case, which can be understood by recalling the degeneracy of the eigenstates of the 2D harmonic oscillator, which model the deep lattice sites quite well. The non-adiabaticity of the quench ensures, that band crossings are skipped and the population is transferred across.

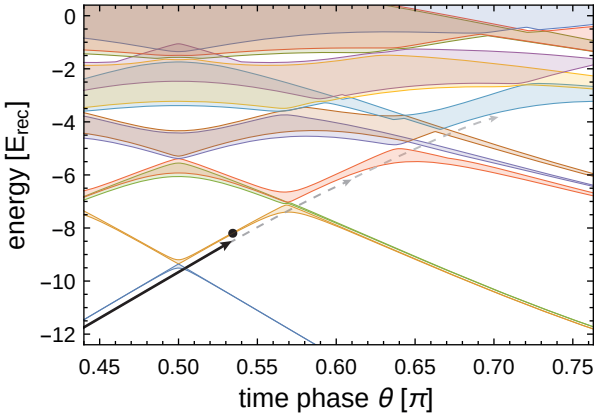

Figure 2.6: **Excitation scheme - band structure:** Calculated band structure for the 2D bipartite optical lattice against the time phase θ for a potential depth of $V_0 = 7\,\mathrm{E_{rec,K}}$. The black arrow indicates the excitation procedure to selectively populate the 2^{nd} band, performing a quench from the initial value of $\theta = 0.4\,\pi$ to its final time phase $\theta = 0.535\,\pi$. Grey arrows sketch the excitation to the 4^{th} and 7^{th} band respectively.

35 In case of the fermionic ensemble it is suspected, that the thermalisation takes place via collisions with the bosonic ensemble, in agreement with the observation, that the lowest temperature of the DFG is observed after a holding time of 3 s together with the BEC in the optical dipole trap(Figure 1.21). At the moment no substructure of the band filling was observed, which might be due to two reasons: 1) the particle number loaded into the lattice is too high and all available states are filled or 2) the temperature is larger than the band width, which results in a population of all states in the band.

2.4 Fermions in higher bands of the bipartite optical square lattice

In this section, the results of the selective population of higher Bloch bands with ultra cold spin polarised, fermionic ensembles are presented. In subsection 2.4.1, a characterisation of the realised states via the band mapping method is given. The momentum distribution is observed via time-of-flight imaging and discussed in subsection 2.4.2. A specific example of an occupied higher band is presented in subsection 2.4.3.

An overview over atoms excited to selected, in this experimental apparatus realised, higher bands is shown in Figure 2.7.

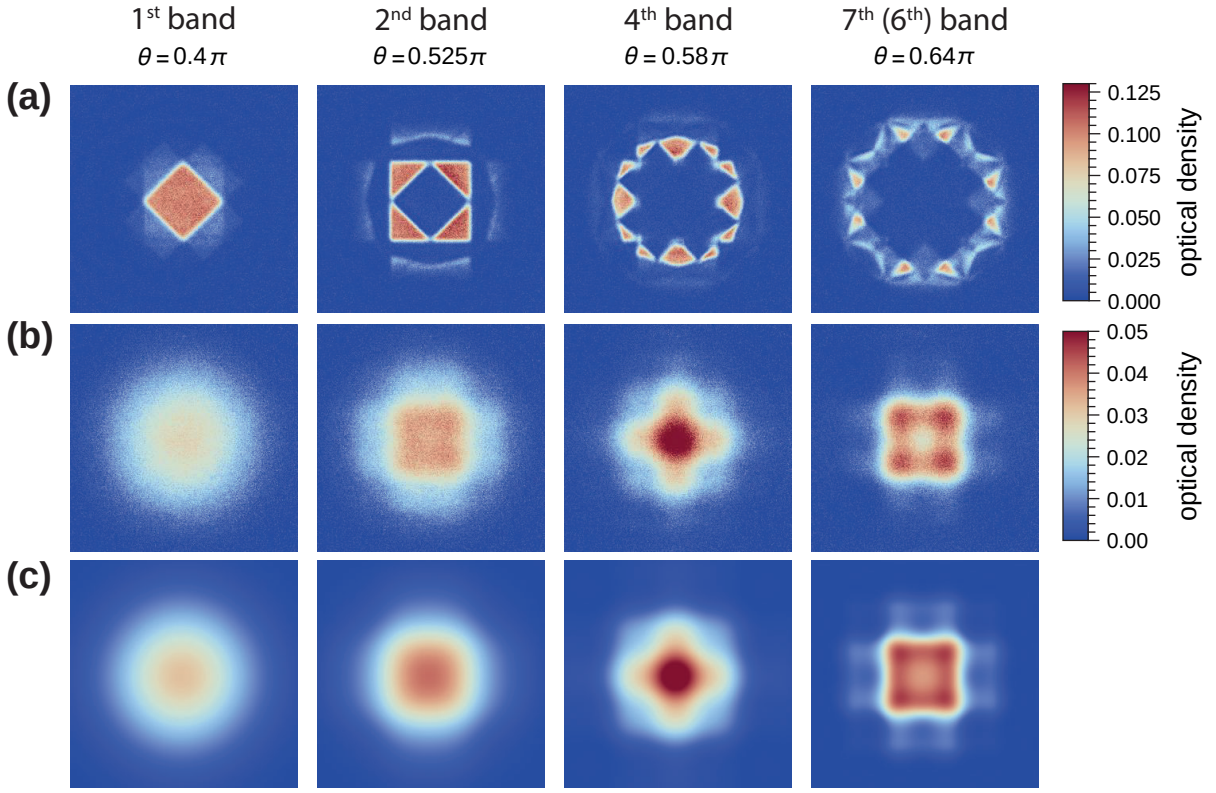

Figure 2.7: **selected higher bands - overview:** Absorption images of DFGs loaded into different Bloch bands of the optical lattice. All images are taken at a lattice depth of $V_0 = 12\,\mathrm{E_{rec,K}}$. **(a)** Band mapping images showing the population of the n^{th} band mapped onto the n^{th} Brillouin zone. **(b)** Momentum distributions recorded after 19 ms of time-of-flight.
(c) shows simulated momentum spectra assuming a homogeneously filled band and neglecting the influence of the harmonic confinement. The fixed colour scale applied to all four images was chosen for the best qualitative agreement with the momentum spectra measured in (b). All images shown for each individual parameter set are averaged over 50 experimental realisations for noise reduction.

2.4.1 Band population

An efficient method to probe the relative occupation of different energy bands is the band mapping method. By lowering the depth of the lattice potential adiabatically with respect to the motion within a single lattice site, the quasi momentum $\mathbf{q}$ of the Bloch function is mapped onto the momentum $\mathbf{k}$ of the free particle dispersion relation. After a subsequent shut-off of the external confining potential and a free ballistic expansion, the momentum distribution $n(\mathbf{k})$ is recorded via absorption imaging. With this detection protocol, atoms originating from the n^{th} band of the optical lattice are mapped onto the n^{th} Brillouin zone (abbr.: BZ). Extracting the particle numbers within regions of interest (abbr.: ROIs) corresponding to these Brillouin zones, the relative band occupation can be measured[BDZ08, Gre+01].

Directly after the DFG is loaded adiabatically within 150 ms into the optical lattice potential at a time phase of $\theta = 0.4\,\pi$, the atoms predominantly occupy the first band of the optical lattice, resulting in a major occupation of the first BZ in the band mapping image shown in Figure 2.7 (a). Nevertheless a finite fraction of ≈35 % of all atoms are already found in the 2^{nd} and 3^{rd} BZ, which was found to be the case independently of the lattice loading time, as long as adiabaticity is ensured. Ruling out this technical reason, two other physical reasons are accounted for this residual occupation: The finite temperature causes a distribution of the populated states around the Fermi energy. Hence, realising the desired filling of the entire first band, and consequently a Fermi level within the band gap between the first and the second band, the thermal distribution around the Fermi level leads to a finite occupation of states belonging to the second band. As a second reason of the residual occupation of higher bands after loading the lattice, the curvature of the bands due to the harmonic confining potential in conjunction with the quantum pressure of the fermionic atoms caused by Pauli's exclusion principle, has been identified. In agreement to this observation, it is possible to slightly tune the ratio of the occupation by changing the external trapping potential by varying the optical power of the dipole trap[Köh+05].

The relative band population was measured versus the final time phase θ_f and the lattice depth V_0. In Figure 2.8, the corresponding absorption images obtained after 19 ms ballistic expansion are shown. Note that in this measurement, the time phase θ has only been changed once during the quench from its initial value of $\theta = 0.4\,\pi$ to the stated final value θ_f and no adiabatic ramp was applied afterwards. As seen in Figure 2.8, parameter sets maximising the contrast of one target band don't resolve the substructure of the bands and the entire target band is filled (see i.e. the 2^{nd} band at $V_0 = 8-10\,\mathrm{E_{rec,K}}$ and

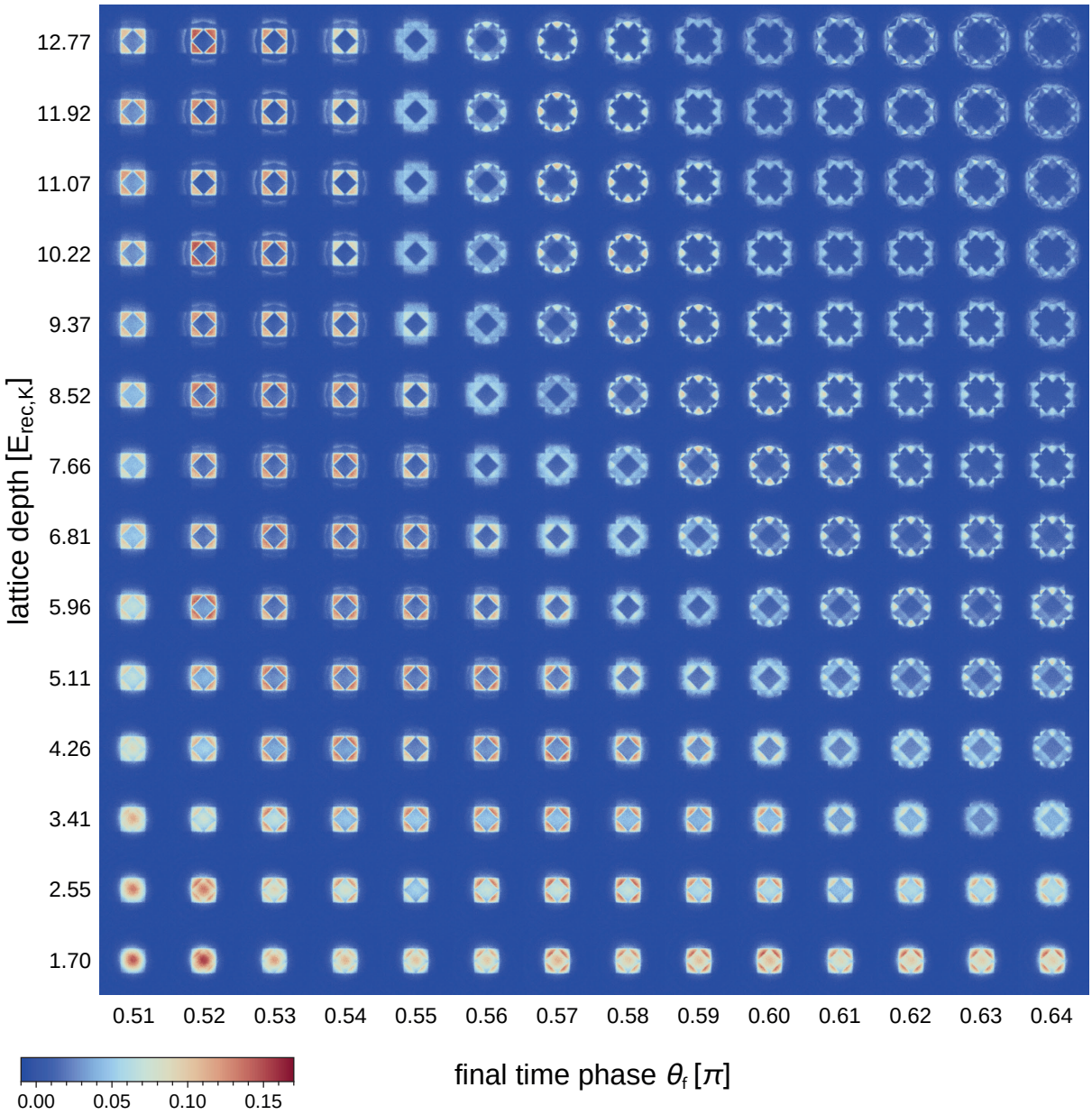

Figure 2.8: **Band populations measured via the band mapping technique:** Prior to loading the lattice, the BEC was removed from the dipole trap by applying a short pulse of resonant laser light. The DFG was then transferred into the lattice at $\theta = 0.4\,\pi$ and held for 10 ms, before the 100 µs quench was performed. After a dwell time of 50 ms, the lattice is adiabatically ramped down within 3 ms to map the quasi momentum $\mathbf{q}$ to the free particle momentum $\mathbf{k}$. The absorption images are then recorded after a ballistic expansion of 19 ms. Images shown for each individual parameter set are averaged over 10 experimental realisations for noise reduction.

$\theta_f = 0.52 - 0.53\,\pi$). This is somewhat expected, because Pauli's exclusion principle forces the atoms to differ in at least one quantum number, such that they have to occupy different Bloch functions with different quasi momenta. Because the number of accessible Bloch states in on the order of the particle number, the target band is entirely filled, which results in the observed, flat, filling of the corresponding BZ.

One additional feature of the band mapping images is the appearance of *halos* around some target bands, especially in the case of the 2^{nd} band (see Figure 2.8, for $V_0 = 10\,\mathrm{E_{rec,K}}$ and $\theta = 0.53\,\pi$). Two possible reasons were identified: the residual population of the 2^{nd} and 3^{rd} band, when loading the lattice at $\theta = 0.4\,\pi$, is transferred into even higher bands and found in the 4^{th} BZ after band mapping. Another possible reason is a suspected mode mismatch between the initial and final Bloch states caused by the external harmonic potential, which results in the occupation of other states, when projected onto the new eigenstates via the quench protocol. The latter of both potential explanations was identified by solving the 1D Schrödinger equation for the lattice potential with the external harmonic potential and creating an equal superposition of all states belonging to the first band[36]. A subsequent projection of this state onto the instantaneous eigenstates after the quench, shows a predominant overlap with states belonging to the second band with a small amplitude for states of the 4^{th} band and almost no overlap to states of the 3^{rd} band. As this result is only obtained by a simple toy model calculation, a more sophisticated calculation might be used to clarify the appearance of the halos for certain parameter sets.

2.4.2 Momentum distribution

The second analysis method, time-of-flight (abbr.: TOF) imaging, is based on the projection of the system's state onto a basis set of plane waves, followed by a free expansion. This is done, by abruptly switching off the lattice and confining potential, such that the system evolves according to the free-particle Hamiltonian[37]. After a sufficiently long time of flight t_{TOF}, the measured density distribution $\rho(\mathbf{r})$ is then directly proportional to the momentum density $\rho(\mathbf{k})$. Thus recording the particle density after time-of-flight expansion via absorption imaging is a direct measure of the momentum distribution of the system's

36 The PDE was solved with Mathematica using a spatial discretisation of 30 points per plaquette consisting of one $\mathcal{A}$- and one $\mathcal{B}$-site. The eigenvalue problem was first solved for a time phase of $\theta = 0.4\,\pi$. Using the gapped nature of the energy spectrum, states belonging to the same band were identified and used to create an unweighted, equal superposition of all states. The basis of the new eigenstates was then calculated by solving the eigenvalue problem for the time phase $\theta = 0.53\,\pi$ and performing a decomposition of the superposition within this basis.

37 The eigenfunctions of the free-particle Hamiltonian are given by plane waves, such that the projection of a Bloch function onto this basis set directly reveals the coefficients of its superposition.

state[BDZ08, Ger+08, Per19]. Note that this is only true for weakly or especially non-interacting particles, such that the interaction during time of flight is negligible, which is the case in this experiment unless the inter particle interaction is enhanced in the vicinity of a Feshbach-resonance[KM10].

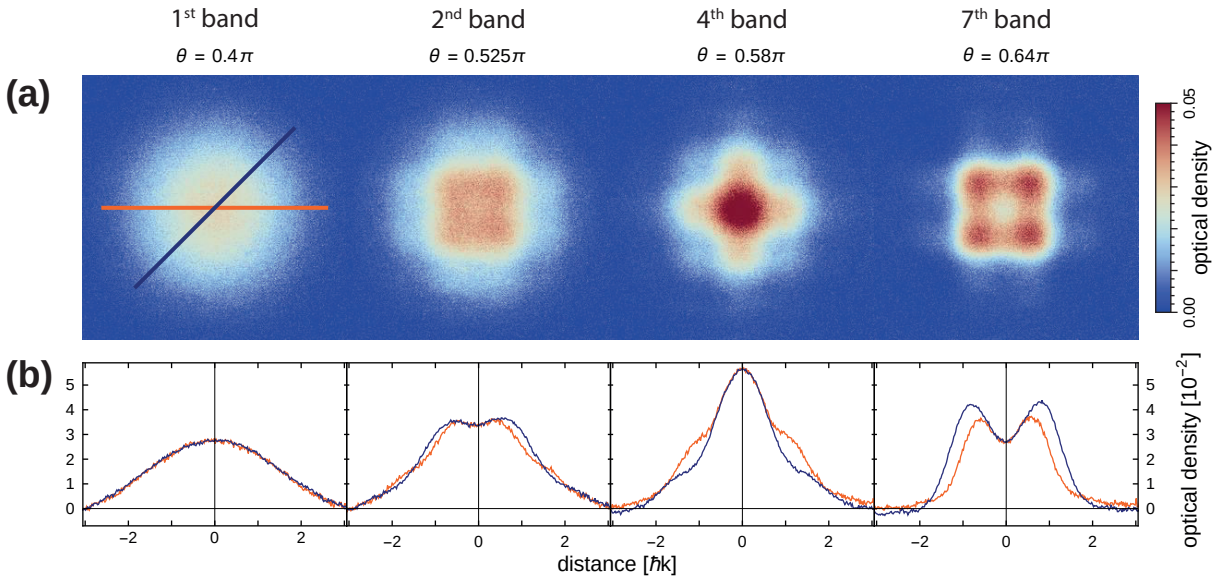

Figure 2.9: **momentum distribution of selected bands: (a)** shows absorption images after 19 ms of time-of-flight for a lattice depth of $12\,E_{rec,K}$. Coloured lines in the first image indicate the section axes. **(b)** an integration of 9 pixel rows along the horizontal (orange) and the diagonal (blue) axis reveals the orbital character of the populated higher bands.

Due to Pauli's exclusion principle, the fermionic atoms cannot occupy a single Bloch state, such the expected momentum distribution is not given by the typical Bragg-spectra observed for superfluid Bose-condensed ensembles in optical lattices. Instead the ultra cold fermionic atoms occupy different Bloch states and eventually fill the corresponding band, such that all quasi momenta $\mathbf{q}$ within the reduced Brillouin zone are occupied[38]. Thus the observed momentum spectrum is expected to only display the squared absolute value of the Fourier transform of the prevailing Wannier functions as an envelope without providing lattice related substructure.

The momentum spectra observed after time-of-flight imaging exhibit direct signatures of the orbital character of the higher bands, populated with the excitation mechanism presented in subsection 2.3.2. In Figure 2.9 (a), momentum spectra for selected final time phases θ are shown, which are recorded after a quench in 100 µs to the stated final time

38 The distribution of the band is dependent on the temperature of the sample as well as the total particle number.

phase and a subsequent 50 ms dwell time of the atoms in the optical lattice. In the 1^{st} band, the atoms reside in the local s-orbitals of the deep $\mathcal{A}$-sites of the lattice and the momentum spectrum shows an isotropic distribution. This is easily seen in the section views plotted in Figure 2.9 (b), which intersect the TOF images along the marked axes. In the 2^{nd} band, where the atoms populate s-orbital like wave functions of the deeper $\mathcal{B}$-sites and the p-orbitals in the shallow $\mathcal{A}$-sites, an increasing nodal structure deviating from the isotropic nature of the first band is observed. This can be seen in the section view observing a flat top, with a small dip in the centre, which can be decomposed in a large s-like component with a small fraction of a p-like orbitals reassembling a cloverleaf structure. The increase of the p-like orbital occupation for larger time phases θ_f can be clearly seen in the 7^{th} band, where the s-like orbital structure disappears and the p-like, cloverleaf structure starts to dominate.

In Figure 2.10, momentum spectra for different pairs of the lattice depths V_0 and the time phase are shown. Note, that in this benchmark measurement, the time phase was directly quenched to its final value, which is stated in the plot.

Remarks on the calculation of the expected momentum spectra

The calculation of the momentum distribution, neglecting the final size of the system as well as the harmonic confinement, is performed as explained in the following: The calculation of the momentum spectrum obtained after time of flight of a single Bloch state is done following [Wir13], section 2.2.7, equation 2.62 and 2.64. Hence, the momentum spectrum for a selected Bloch function is given by a periodic delta peak structure shifted by its quasi momentum, with an envelope given by the Fourier transform of the Wannier function of the corresponding band. The latter is found to be directly given by the absolute squared coefficients of the plane-wave expansion of the Bloch function. These coefficients can easily be calculated by a numeric 2D band structure calculation. An efficient way to display the momentum spectrum is then found to be just to arrange the entries of the eigenvector as a square array and upsample the array, inserting zeroes in between calculated values. Finally a Gaussian filter is applied to the array to emulate the effect of finite system size[39]. For a bosonic ensemble condensed at the band minimum, it is sufficient to consider only the corresponding Bloch function to obtain a good agreement with the

39 For an infinitely large, homogeneously filled periodic potential the momentum spectrum is given by an array of delta peaks. To simulate the effect of a finite coherence length in the case of a bose-condensed ensemble, the delta peaks are replaced by Gaussian peaks with a finite width, matching the experimentally observed coherence length. In the array representation this can be efficiently done by applying a Gaussian blur, after upsampling the array.

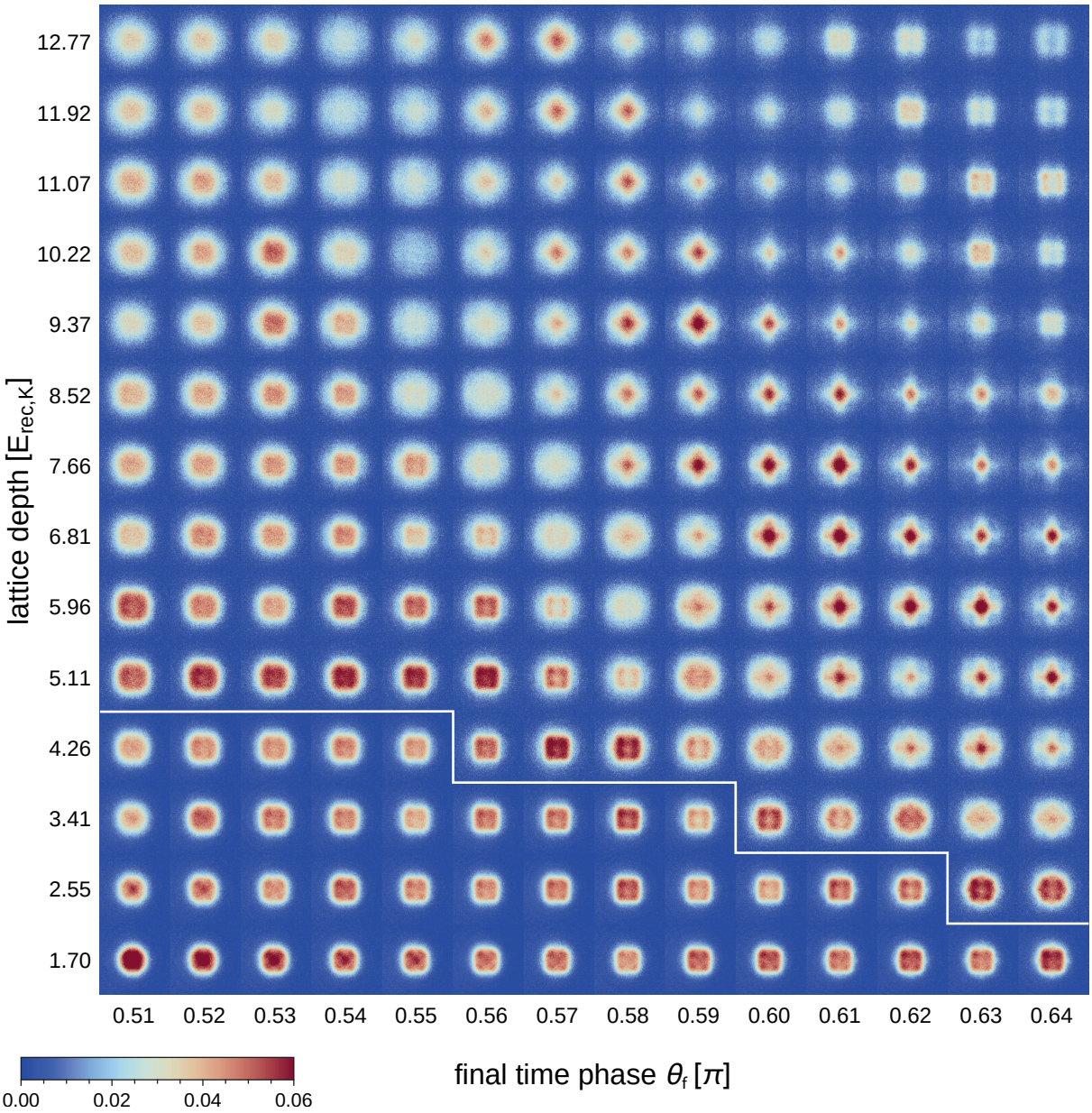

Figure 2.10: **Momentum distribution measured via TOF imaging:** Absorption images taken after 19 ms of free ballistic expansion, after the atomic samples were released form the optical lattice and confining potential by abruptly switching both off within <1 µs. The plotted optical density for images below the white line are downscaled by a factor of 1.5 in order to preserve details in images with higher densities, while retaining information for less dense parameter sets. Images shown for each individual parameter set are averaged over 10 experimental realisations for noise reduction.

momentum spectrum observed in the experiment. In case of the fermionic ensembles, a homogeneously filled band is assumed, resulting in the occupation of each quasi momentum $\mathbf{q}$ with equal weight. The momentum spectrum in this case is thus calculated as a direct sum of all involved Bloch functions. This is done by sampling the quasi momenta $\mathbf{q}$ over a 61×61 grid. A calculation of the fermionic momentum spectra involving over 3600 Bloch functions can be performed within 1 min.

2.4.3 More exotic states

Besides of enabling the population of higher bands, the possibility to change the band structure in situ allows for more complicated experimental protocols. Due to the vanishing interaction of spin polarised fermionic ensembles at low temperatures, they show remarkable long life times in the lattice (see chapter 3) and even slow ramps across otherwise lossy band crossings can be realised. Therefore, with fermionic samples, states can be addressed, that are inaccessible with bosons, like the 4^{th} band at $\theta = 0.535\,\pi$.

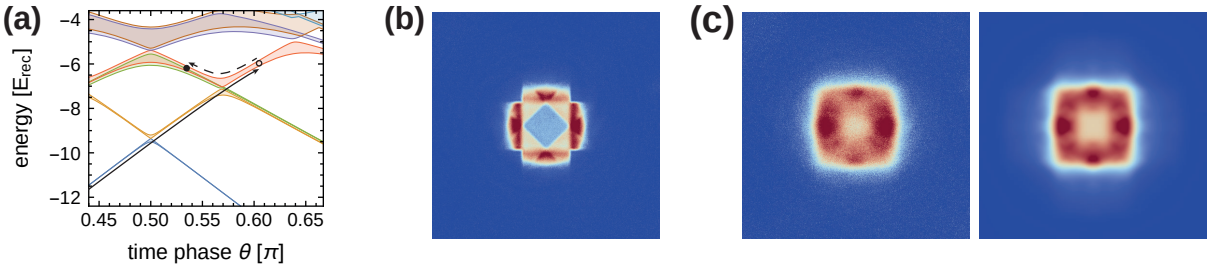

Figure 2.11: 4^{th} **band at** $\theta = 0.535\,\pi$ **- BM and TOF: (a)** sketches the two step excitation protocol used. The solid black arrow indicates the first quench to the 4^{th} band (open circle), the dashed arrow visualises the adiabatic ramp to the final state (filled disk). **(b)** Band mapping image used to extract relative band populations. **(c)** measured (left) and simulated (right) momentum spectrum.

In Figure 2.11 (a) a three-step excitation protocol is sketched, which was successfully used in the experiment to prepare a DFG in the 4^{th} band at $\theta = 0.535\,\pi$. After loading the lattice in 150 ms at $\theta = 0.4\,\pi$, the atoms dwelled in the lattice for 50 ms and were excited to the 4^{th} band via a 100 µs quench to $\theta = 0.605\,\pi$ and held for 10 ms. A subsequent adiabatic ramp of 10 ms transferred the ensemble across the band crossing to its final state at $\theta = 0.535\,\pi$ and was held for 10 ms. The state is then analysed by means of band mapping as well as time-of-flight imaging, shown in Figure 2.11 (b) and (c). From the band mapping image, the relative band occupation c_n of the n^{th} band was extracted and found to be $c_1 = 0.07, c_2 = 0.24, c_3 = 0.31, c_4 = 0.38$. Using these relative ratios, the momentum distribution is simulated as a weighted sum of the four momentum distributions obtained

for homogeneously filled bands. The experimentally recorded TOF image (left) is shown along with the simulated (right) momentum spectrum in Figure 2.11 (c). As clearly visible, the rotational C4-symmetry is slightly broken due to small imbalances of the lattice beam intensities, such that this has to be incorporated in the simulation. Despite the simplicity of the underlying assumptions, the simulated momentum spectra show a remarkably good agreement with the experimentally measured images. Note that even the small local maxima in between the four main maxima, visible in the simulation are reproduced in the experiment, especially in the lower halfs of the images in Figure 2.11 (c). The good agreement obtained between observations and theoretical simulations allows us to identify the state obtained, even in the case of involved multi-step excitation protocols.

2.5 summary

In this chapter, experiments with ultracold fermions prepared in selected higher Bloch bands were described. These experiments start with a quantum degenerate Fermi gas loaded to the lowest band of an optical square lattice with a bipartite unit cell hosting two lattice sites with different experimentally tunable well depths. Rapid tuning of the well depth difference allows for targeted excitation of the atoms to certain higher Bloch bands. A subsequent additional adiabatic change of the well depth difference lets one selectively populate any available band.

The analysis of the experimentally prepared fermionic many-body states is carried out using momentum spectroscopy and band mapping. Our observations are in excellent agreement with theoretical simulations, and clearly reveal the orbital character of the produced state. Even for intricate two-step excitation protocols, composed of a quench and a subsequent adiabatic adjustment of the unit cell, we may thus reliably identify the state obtained.

3 Band relaxation from the 2^{nd} band

This chapter discusses the band relaxation of atomic samples in the second band of the bipartite optical square lattice. The first section 3.1 presents the decay dynamics of a spin-polarised, non-interacting Fermi gas and introduces a phenomenological rate equation model to describe the identified inter-band processes. In section 3.2, the band relaxation of an interacting Fermi gas is discussed and analysed in terms of an extended rate equation model. The chapter is summarised in section 3.3.

Remarks on the band relaxation of bosonic samples from the second band

The band relaxation of coherent bosonic ensembles from higher bands of the bipartite optical square lattice has been studied for a broad range of experimental parameters in two experimental setups in our research group, partially using the experimental apparatus described here. The experimental results[Nus+20, Koc+16, WÖH10] as well as a theoretical framework are published in [Nus+20] and briefly summarised in the following.

In the bosonic case, a three-stage relaxation process from the second band was identified, where a transient coherent metastable state protects the sample from decay to the lowest band by destructive many-body interference. During the first stage, the incoherent excited state found directly after the quench to the second band condenses at the band minima, the phase coherence increases and a metastable coherent state is formed. The second stage shows a slower than exponential decay of the population in the second band, which arises as a consequence of the chiral phase pattern of the ground state in the second band. This results in a suppression of the decay of the condensed part, as the destructive many-body interference of two decay channels prohibits decay to the first band and only thermal atoms are allowed to decay. Collisions of heated atoms with the condensed part deplete the latter and overcompensate the exponential decay to the thermal ground state such that the total population of the second band decays slower than exponential. The third stage of the decay starts as soon all condensed atoms are heated into thermal atoms and an exponential decay from the thermal excited state in the second band to the thermal ground state in the first band is observed.

3.1 Decay dynamics of a non-interacting fermionic ensemble

In order to study complex quantum phases in higher bands, understanding and quantifying the involved band relaxation mechanisms plays a vital role. This section describes the lifetime measurement of a spin polarised Fermi gas excited to the second band of the optical lattice.

In the case of a BEC of rubidium atoms excited to the second band of the optical lattice, two-body s-wave collisions have been identified to limit the lifetime of atoms in higher bands. For a spin polarised fermionic sample, s-wave scattering is suppressed by Pauli's exclusion principle and only higher order scattering terms contribute. At sufficiently low temperatures below 30 µK, p-wave collisions are suppressed for potassium-40 atoms[DeM+99, DeM01, Gol05] unless enhanced via a Feshbach resonance (see section 5.2) and thus can be ruled out. The remaining scattering induced band relaxation process is therefore given by collisions with hot background gas atoms, which can be neglected on the few ten second time scales observed for the second band[40]. Hence, interaction is expected to be practically irrelevant for band relaxation of spin polarised Fermi gases in the case discussed here and results in band lifetimes exceeding those recorded in the bosonic case by around two orders of magnitude.

As a consequence of the absence of inter-atomic scattering, the main limitation of the lifetime is expected to be heating of the atomic sample caused by intensity fluctuations of the light potentials. This includes heating caused by intensity fluctuations and atom-light scattering (see Equation 1.13) of the crossed optical dipole trap as well as the standing waves providing the optical lattice potential. Justified by the long lifetime of the DFG in the ODT of over 200 s, the intensity fluctuations and heating processes purely caused by the ODT are assumed to be negligible on the time scales of interest here and thus the lattice potential is suspected to be mainly responsible for heating[41]. If the involved heating process is resonant to an interband transition, this results in a finite transition rate of atoms from one band to another and drives band relaxation. While the onsite trap frequencies in the plane are exclusively given by the lattice potential, the gaussian

40 see section 1.7, where the DFG lifetime of $\tau_{\mathrm{K,DFG,initial}} = (223 \pm 12)\,\mathrm{s}$ has been observed and identified with background gas scattering.

41 Besides of mechanical instabilities and noise effectively changing the optical path lengths in air due to density modulation, two stabilised quantities directly affect the lattice potential: laser intensity fluctuations result in a modulation of the overall lattice depth V_0 and fast fluctuation of the relative time phase θ changes the potential difference between neighbouring lattice sides. Both of which lead to a fluctuation of the onsite trap frequencies.

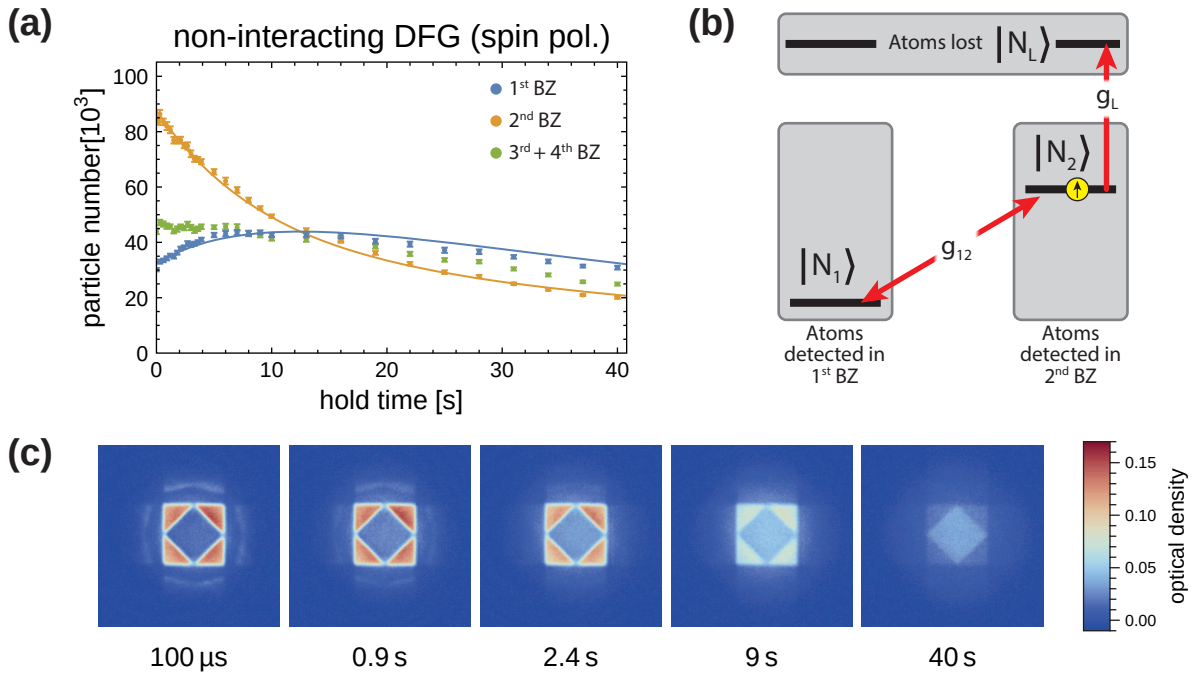

Figure 3.1: **Band relaxation dynamics for non-interacting Fermi gases from the second band:** **(a)** shows the population of the n^{th} band extracted via band mapping plotted against the hold time in the optical lattice. The solid lines result from simultaneously fitting N_1 and N_2 from the model to the recorded data. **(b)** visualises the rate equation model from Equation 3.1 used as a minimal model. **(c)** shows band mapping images after selected hold times, which were used to determine the band population.

envelope of the intensity profile of the lattice beams is only a small contribution to the onsite trap frequency in the z-direction, which is mainly given by the confining potential created by the ODT. Therefore fluctuations of the lattice potential predominantly result in heating in the lattice plane and cross-dimensional heating along the z-axis is expected to be small, due to the lack of collisions, as discussed above.

The lifetime measurement of a spin polarised ensemble in the second band is initialised by loading around 170×10^3 potassium-40 atoms with a temperature of around $0.18\,\mathrm{T_F}$ into an optical lattice with $V_0 = 7\,\mathrm{E_{rec,K}}$ at $\theta = 0.4\,\pi$ and transferring the population into the second band by quenching the relative time phase to $\theta = 0.535\,\pi$. In Figure 3.1 (a) the measured band occupation is plotted against the hold time in the optical lattice resolved with the band mapping technique. A selection of the corresponding band mapping images is shown in Figure 3.1 (c). From the 100 µs hold time absorption image it can be seen, that directly after the quench, a finite fraction of atoms are found in the first band and the halos indicate a population of the forth band. This can also be seen in Figure 3.1 (a),

where the first data points indicate a relative population of the second band of around 50 % of all atoms.

$$\begin{aligned} \dot{N}_1 &= g_{12}\,(N_2 - N_1) \\ \dot{N}_2 &= g_{12}\,(N_1 - N_2) \quad -g_L N_2 \\ \dot{N}_L &= \qquad\qquad\quad +g_L N_2 \end{aligned} \tag{3.1}$$

As a minimal model to describe the band decay dynamics, a coupled rate equation model is used, which is given by Equation 3.1. The absolute population of the first and second band is described by N_1 and N_2 respectively and coupled by a balanced bidirectional transition rate g_{12}. This coupling is associated to heating in the lattice plane and assumed to be bidirectional with identical rates between the first and second band in good agreement with the experimental data. Additionally the absolute number of atoms lost from the system is considered and labelled as N_L. As atoms no longer confined by the trapping potentials are either excited into higher bands and weakly bound or directly lost from the system, this is modelled by a unidirectional heating rate g_L resulting in a loss from N_2. In Figure 3.1 (b) this minimal rate equation model is visualised.

Using this simple rate equation model and simultaneously fitting the populations N_1 and N_2 to the experimental data, the heating rates g_{12} and g_L as well as the total number of atoms N_{tot} in the first and second band and their initial band occupation ratio r are determined. Therefore the initial condition is set to be $N_1(0) = rN_{tot}$ and $N_2(0) = (1-r)N_{tot}$. All four parameters were fitted without any parameter constraints and the results are found in Table 3.1. During the first 10 s, the development of the second band population is very well described by an exponential function with a $1/e$ decay time of (16.97 ± 0.21) s, whereas the full solution for N_2 reaches $1/e$ of the initial population after 21.21 s. The introduction of more bands and balanced heating rates between neighbouring bands as free system parameters could not be justified and did not yield better qualitative or quantitative results.

parameter	value
g_{12}	$(0.04316 \pm 0.00290)\,1/\mathrm{s}$
g_L	$(0.04229 \pm 0.00092)\,1/\mathrm{s}$
N_{tot}	$120\,287 \pm 587$
r	0.2715 ± 0.0037

Table 3.1: Fit results of the rate equation model

3.2 Decay dynamics of an interacting fermionic ensemble

This section describes the lifetime measurement of an interacting Fermi gas excited to the second band of the optical lattice.

If a two spin component Fermi gas is prepared, s-wave scattering is no longer prohibited by Pauli's principle and the atomic sample becomes interacting. For the balanced spin mixture of $|F = 9/2, m_F = -9/2\rangle$ and $|F = 9/2, m_F = -7/2\rangle$ realised in this experiment, the singlet scattering length is found to be $104\,a_0$ and the triplet scattering length $176\,a_0$. As these values are on the order of the s-wave scattering length found for rubidium-87 ($98\,a_0$)[Ego+13], the influence of collisional properties onto the band relaxation dynamics is assumed to be comparable. In the case of the bosonic sample, the main collisional loss channel, resulting in a depopulation of the second Bloch band, is associated with a transfer of pairs of atoms from the second band to the first band[Nus+20, PT13]. Therefore we assume a similar process for the two spin component Fermi gas, such that two collision partners, one spin up and one spin down particle are transferred to the first band. In accordance with energy and momentum conservation, for each of those particles a potential energy equal to the band gap between both bands is released and deposited as kinetic energy in the third dimension, perpendicular to the lattice plane. Due to the fact, that in the beginning a balanced spin mixture is created, it is assumed, that this behaviour is identical for both spin components. Because scattering between particles with the same spin is still forbidden due to Pauli's principle, the same description from section 3.1 can be used. In addition, the existence of a scattering channel, that can redistribute kinetic energy between the xy-plane and the z-direction, enables cross-dimensional heating.

The lifetime measurement of a two spin component Fermi gas in the second Bloch band is initialised by two steps. After the final evaporation in the ODT, the balanced spin mixture is prepared as described in section 1.8. After a hold time of 20 ms to ensure decoherence, the magnetic bias field used for spin preparation is ramped down to 1 G. In a second step, the spin mixed Fermi gas is loaded into the optical lattice with the identical protocol used for the spin polarised sample. No deviation of the optimal transfer protocol has been observed in this case, such that the population swap into the second band is performed with the same non adiabatic quench of $\theta = 0.4\,\pi$ to $\theta = 0.535\,\pi$ for a $7\,\mathrm{E_{rec,K}}$ deep lattice. In Figure 3.2 (a) the measured band occupation is plotted against the hold time in the optical lattice resolved via the band mapping technique. Five selected band mapping images are shown in Figure 3.2 (b). Compared to the band mapping images in

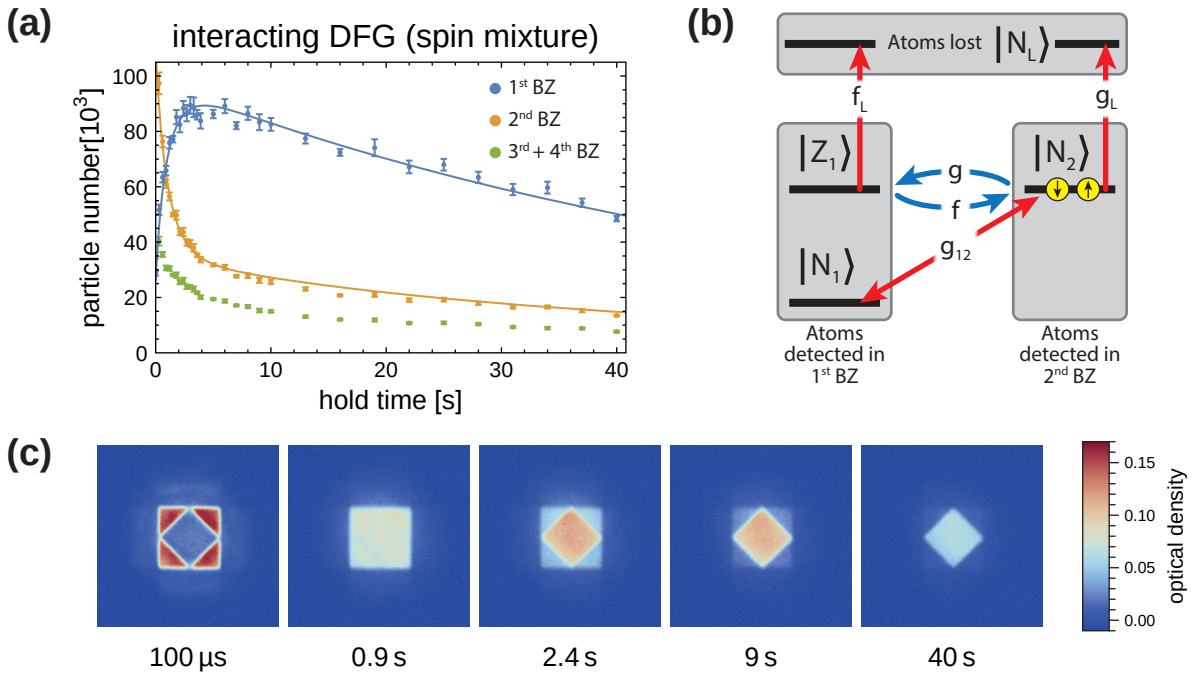

Figure 3.2: **Band relaxation dynamics for interacting Fermi gases from the second band:** **(a)** shows the population of the n^{th} band extracted via band mapping plotted against the hold time in the optical lattice. The solid lines are fit results for N_1 and N_2 from the extended rate equation model.
(b) visualises the extended rate equation model from Equation 3.2.
(c) band mapping images for selected hold times. Note that equal column density in the first and second BZ indicating equal population is recorded after only 0.9 s, which is an order of magnitude faster than in the spin polarised case.

Figure 3.1 (c) the halos in the region of the fourth Brillouin zone are less pronounced and slightly blurred. As this is already the case for very short hold times of only 100 µs, it is suspected, that this is not the result of a dynamical behaviour in the lattice but rather a change in the initial preparation of the first band. One possible mechanism might be the reduced Fermi pressure due to the lower particle number per spin state resulting in a smaller insitu size of the atomic sample, which in turn leads to a reduced distortion of the bands and hence a cleaner and more selective loading of the first band (see halos in Figure 2.4). Despite the impurities in the loading process, the relative population of the second band is still found to be around 50 % of all atoms detectable via absorption imaging.

For modelling the band relaxation and its time-dependence, only band index changing collisions have to be considered. Therefore only the previously mentioned pair relaxation process from the second band to the first band with simultaneous excitation along the z direction has to be included into the rate equation model (Equation 3.1) used to describe

the decay of a non-interacting sample. This is done by introducing a state Z_1 describing the part of the population of the first band, which is excited along the z direction. The extended rate equation model is then given by Equation 3.2 and visualised in Figure 3.2. The loss from the second band caused by collisions is modelled with a two-body collision term gN_2^2, with $g \equiv \beta/(2V_{N_2,eff})$. In this context β denotes the two-body collision parameter and $V_{N_2,eff}$ is the effective volume occupied by the atoms residing in state N_2[HH06, Wei+99]. As the opposite process, namely the collision of atoms in the Z_1 state resulting in a population of the energetically identical state N_2, is also possible, it is considered as well. This is done by the introducing another two-body collision term fZ_1^2, with $f \equiv \beta/(2V_{Z_1,eff})$, where $V_{Z_1,eff}$ denotes the effective volume of atoms in the Z_1 state. Similarly as N_2, the Z_1 state is also depopulated with a given rate f_L to the lost atom population modelled with N_L.

$$\begin{aligned}
\dot{N}_1 &= g_{12}\,(N_2 - N_1) \\
\dot{Z}_1 &= \qquad\qquad +gN_2^2 - fZ_1^2 - f_L Z_1 \\
\dot{N}_2 &= g_{12}\,(N_1 - N_2) \quad -gN_2^2 + fZ_1^2 \qquad\quad -g_L N_2 \\
\dot{N}_L &= \qquad\qquad\qquad\qquad + f_L Z_1 \quad +g_L N_2
\end{aligned} \tag{3.2}$$

Fitting the numerical solution to the coupled differential equations given in Equation 3.2 is done in the following way: Due to the fact, that the population of the states N_1 and Z_1 cannot be distinguished by means of band mapping, as they both are mapped to the first Brillouin zone, only the sum $N_1 + Z_1$ can be fitted to the first band population. The initial condition is set to be $N_1(0) = rN_{tot}$ and $N_2(0) = (1-r)N_{tot}$, with the addition of $Z_1(0) = 0$. By fixing the numerical values of the heating rates g_{12} and g_L to those found in Table 3.1, the only free fit parameters are the collision rates g and f, the heating rate f_L, the particle number in the first and second band N_{tot} and the occupation ratio r. The results of the unconstrained fit for these five parameters are found in Table 3.2.

parameter	value
f_L	$(0.01694 \pm 0.00152)\,1/\mathrm{s}$
g	$(6.40 \pm 0.29) \times 10^{-6}\,1/\mathrm{s}$
f	$(1.83 \pm 0.16) \times 10^{-6}\,1/\mathrm{s}$
N_{tot}	$135\,606 \pm 970$
r	0.1940 ± 0.0124

Table 3.2: Fit results of the extended rate equation model

The perceived difference in the scattering rates g and f is explained by the fact, that the effective scattering volumes $V_{N_2,eff}$ and $V_{Z_1,eff}$ are different. Assuming no imbalance of the two-body collision parameter β in the first and second band, the ratio of the two effective scattering volumes can be calculated and is given by $V_{Z_1,eff}/V_{N_2,eff} = g/f = 3.50 \pm 0.34$. This seems reasonable, because the population of Z_1 resides in a excited state resulting in a larger spread along the z direction. This could be further verified by faster expansion of the sample in this direction, but is not measured yet.

As previously mentioned, a collision channel opens the possibility of cross dimensional heating, such that atoms from N_1 could be transferred to Z_1 via heating. Due to the fact, that this term would contribute linearly in the particle number, it can not be absorbed into other transfer rates and should be distinguishable. Nevertheless, including such a term in the model could not be justified, as the experimental data available so far only detects the sum $N_1 + Z_1$ and a qualitative measure of the occupation of the Z_1 state using absorption imaging from the side has not been extracted to this point.

As there is no analytical solution to Equation 3.2 and the time-dependence is vastly different from an exponential decay, where a lifetime by means of the $1/e$ time constant can be extracted, the chosen method to define a lifetime is by extracting the time for the population N_2 to reach $N_2(0)/e$. In the case of this two spin component Fermi gas excited to the second Bloch band, the lifetime is found to be 2.61 s, which is about one order of magnitude less than found for the spin polarised sample.

3.3 summary

In this chapter, the lifetime measurement of non-interacting and interacting Fermi gases prepared in the second Bloch band were explained in detail. The role of s-wave scattering in the band relaxation is discussed and heating processes leading to interband excitations are elaborated.

A simple rate equation model was developed, describing the band relaxation due to heating in the case of a spin polarised sample and later successfully extended to capture the collision induced band relaxation dynamic in the case of a two spin component mixture. Using this model, heating and scattering rates linking different bands and excitation levels are extracted and a lifetime by means of a $1/e$ value of the initial population is defined. In the case of a spin polarised sample, remarkable long lifetimes in the second Bloch band of 21.21 s are observed, superseding those found for a two spin component gas by an order of magnitude, where a lifetime of 2.61 s is measured.

4 Experiment control, absorption imaging and data analysis

In typical quantum gas experiments a variety of different devices have to be addressed in real time. Therefore an experimental control system has to established, which is capable of handling the communication between different devices as well as computers. Such a hardware control system has to be complemented with a software environment to allow for convenient manipulation of experimental parameters and assistance for the experiment operator. One design guideline of this experiment control system was to be accessible via a network connection, such that the experiment can be controlled from anywhere, without the experiment operator being in the laboratory. Therefore additional safety measures have been established with an independent interlock system and monitoring of a multitude of relevant experimental parameters with a completely disconnected system.

section 4.1 describes the experiment control system with a heavy focus on the control software (subsection 4.1.2), as it was completely reworked by me during the work on this thesis. Section 4.2 presents the absorption imaging program used for reading data from the scientific cameras and saving it to the hard drive. In section 4.3 the post-processing of the data sets taken is explained and the fringe removal algorithm optionally used during the analysis is introduced. section 4.4 summarises the interplay of experiment control, imaging program and analysis used in this experimental apparatus.

4.1 Experiment control system

The experiment control system is composed by a sophisticated hardware setup which is complemented with a software environment capable of handling the communication between all devices. subsection 4.1.1 introduces the hardware used in the experiment, subsection 4.1.2 presents the experiment control software.

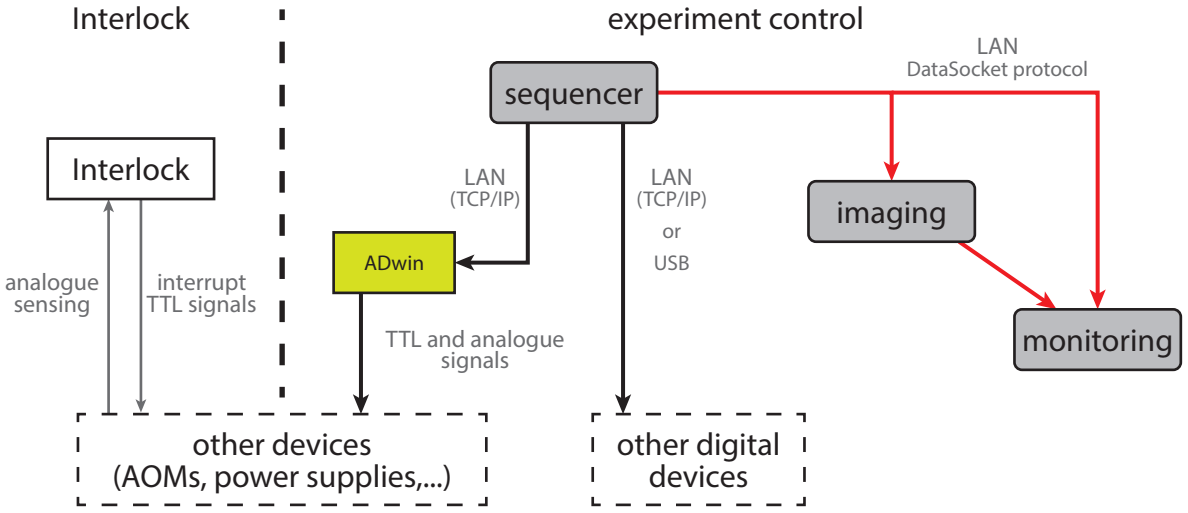

Figure 4.1: **Experiment control hardware flowchart:** The mutual dependencies of hardware systems involved to control the experimental apparatus presented in this thesis.

4.1.1 Experiment control hardware

The experimental control hardware consists of three main parts. The backbone of the real time communication is an ADwin Pro-II system[42], which is in turn programmed by the second important device, the sequencer computer. The read-out of the absorption images from the cameras is done with additional imaging computers, where an arbitrary number of imaging PCs can be used simultaneously. To protect the experimental apparatus from hardware or software failures, which might cause irreversible damage to the setup, an interlock system is used[43]. To safely operate the experiment in remote control a monitoring system for important experimental quantities was implemented as well. The mutual dependencies of all systems are diagramed in Figure 4.1.

ADwin Pro-II system

The ADwin Pro-II system is a real time environment based on a microprocessor[44], which controls digital and analogue input and output-modules (abbr.: IO-modules). In our case a total of 64 synchronised digital output channel can be used to create TTL signals. These signals are used to switch mechanical shutters, IGBTs and MOSFETs as well as provide

42 ADwin Pro-II from Jäger Computergesteuerte Messtechnik GmbH
43 The system was set up previous to the work on this thesis, Raphael Eichberger programmed the interupt logic during his PhD work.
44 T11 module from Jäger Computergesteuerte Messtechnik GmbH, 300 MHz clock frequency

various trigger signals for the camera exposure and radio-frequency generators. In addition 40 analogue output control voltages ranging between ±10 V can be generated by a 16-bit DA converter. These are for example used to remote control important optical parameters such as power and frequency of most lasers used in the experiment. Additionally the setpoint for the stabilisation of the optical lattice interference time phase θ (see section 2.1 and subsection 2.2.1) is controlled with such an analogue signal.

Sequencer computer

The *sequencer computer* is used to input the experimental sequence, calculating parameter ramps, adjusting timing offsets and translating it into commands for the ADwin Pro-II system. Subsequently, the sequence is transmitted to the ADwin system and executed. The ADwin system is therefore directly connected to the sequencer PC with a LAN cable, such that access to the ADwin system is only granted to the sequencer PC and all other device in the laboratory local network are prevented from interrupting the connection. The communication with other devices in the laboratory is either done directly via a USB cable[45] or by a network connection[46].

The software used to input the experimental sequence is a software written in LabVIEW. During the work on this thesis the software was completely rebuilt, only the core elements of the communication with the ADwin system date back to a code written by Christian Ospelkaus in 2003. The design of this modular software and the communication protocol is described in subsection 4.1.2.

Imaging computer

The *imaging computers* are used to run a LabVIEW software, which handles the communication to the cameras used for imaging. After an exposure of the camera has been initiated by a hardware trigger given by the ADwin system, the sensor read-out is handled by the software and saved as unprocessed raw images to the hard drive. In addition, the corresponding experimental sequence data is obtained from the *sequencer computer* and stored as text files. These data sets are then further processed as described in section 4.2 to obtain optical densities from the absorption images.

45 Both frequency generators VFG-150 and the frequency generator Agilent 33522A

46 All computers operated in the laboratory are connected to the same local network. This includes computers used for imaging, monitoring, laser locking as well as the sequencer computer

Interlock system

The *interlock system* is a completely independent commercial interlock system, which prevents damaging of the experimental apparatus caused by hardware or software problems due to the failure of devices or user error. Therefore multiple sensors are used to monitor important quantities in the apparatus, like the temperature of the coils for the magnetic trap or the cooling water flow rate, and shuts down certain parts of the experiments, if necessary. The shutdown logic is processed by a microcontroller and was programmed by Raphael Eichberger. This interlock system is used as a backup, if software side safety measures fail or the communication to the ADwin is stopped due to network connection issues.

Monitoring computer

The *monitoring computer* is used to independently sense multiple experimental quantities in real time to ensure safe remote operation of the experiment. Therefore an ADC[47] is used to monitor analogue signals from monitoring photodiodes and current sensors. For example, the power of the optical dipole trap and the current ramps during the transport procotol can be observed in real time during the experimental sequence, independent of the control value set by the ADwin system. Additionally a temperature data logger[48] is used to permanently log the temperature of important experimental parts, like the coils used for transport and the experiment and laser optical table. One auxiliary camera provides monitoring of the MOT loading curve by taking florescence images at a rate of 15 Hz during the experimental sequence, such that the MOT loading performance can be benchmarked even in remote operation.

4.1.2 Experiment control software with LabVIEW

The experiment control software used to input an experimental sequence is executed on the *sequencer computer*. It converts the commands entered into the graphical user interface, processes them internally, handles the communication with other software parts (like the imaging program) and transmits the corresponding processed experimental sequence data to all devices involved. Subsequently, the experimental sequence is executed.

This section describes the graphical user interface of the software and the internal structure of the program. Useful features include the automatic multi-dimensional param-

47 USB-6625 from National Instruments
48 TC-08 from Pico Technology

eter scans, the automatic processing of control measurements in between long continuous measurements as well as various tools to easily input experimental sequences. Additionally the possibility to implement a semi-automatic parameter optimisation was planned and can be implemented in the future.

graphical user interface

The LabVIEW control software features an graphical user interface (abbr.: GUI), which is shown in Figure 4.2. Experimental sequences are entered as a list of successively executed parameter sets. Each of these parameter sets is called *time slot* and contains one numerical value for the duration, 64 digital values, 40 analogue control values, as well as settings for two frequency generators used for RF-evaporation (section 1.5) and spin preparation (see section 1.8). As an intuitive visual representation these parameter sets are aligned in columns, such that simultaneously applied parameter sets appear vertically aligned. The following *time slot* is then arranged directly next to it, such that the time line is read from left to right. The collection of all time slots is also referred to as *sequence control array*. For convenience the analogue control values are entered in natural units (i.e. MHz for AOM frequencies) and later converted by corresponding transfer functions.

At the moment three execution modes are available in the experiment control software:

— the *single execution*, where the experimental sequence is executed exactly once and then stopped

— the *continuous execution*, where the experimental sequence is executed indefinitely with the experimental sequence data given at the point of execution, until this mode is stopped by the user.

— the *sequential execution*, where automatic parameter scans can be performed.

One important part of the GUI is the area to enter automatic parameter scans (see Figure 4.2, top left). Every numerical quantity in the array of *time slots* is accessible for automatic parameter manipulation in a given parameter range. The interface allows for two independently scanned parameters at a time, such that a 2D-parameter space can be scanned automatically (i.e. see Figure 1.7) and executed with a given repetition number for reduced statistical error. In addition the parameter sets can be shuffled in different randomised orders, such that slow drifts of experimental quantities like the particle number affect all measured parameter sets equally and systematic errors are distributed equally across all parameter sets. As this execution mode is executing different parameter sets sequentially (but not necessary in order), it is called *sequential execution*.

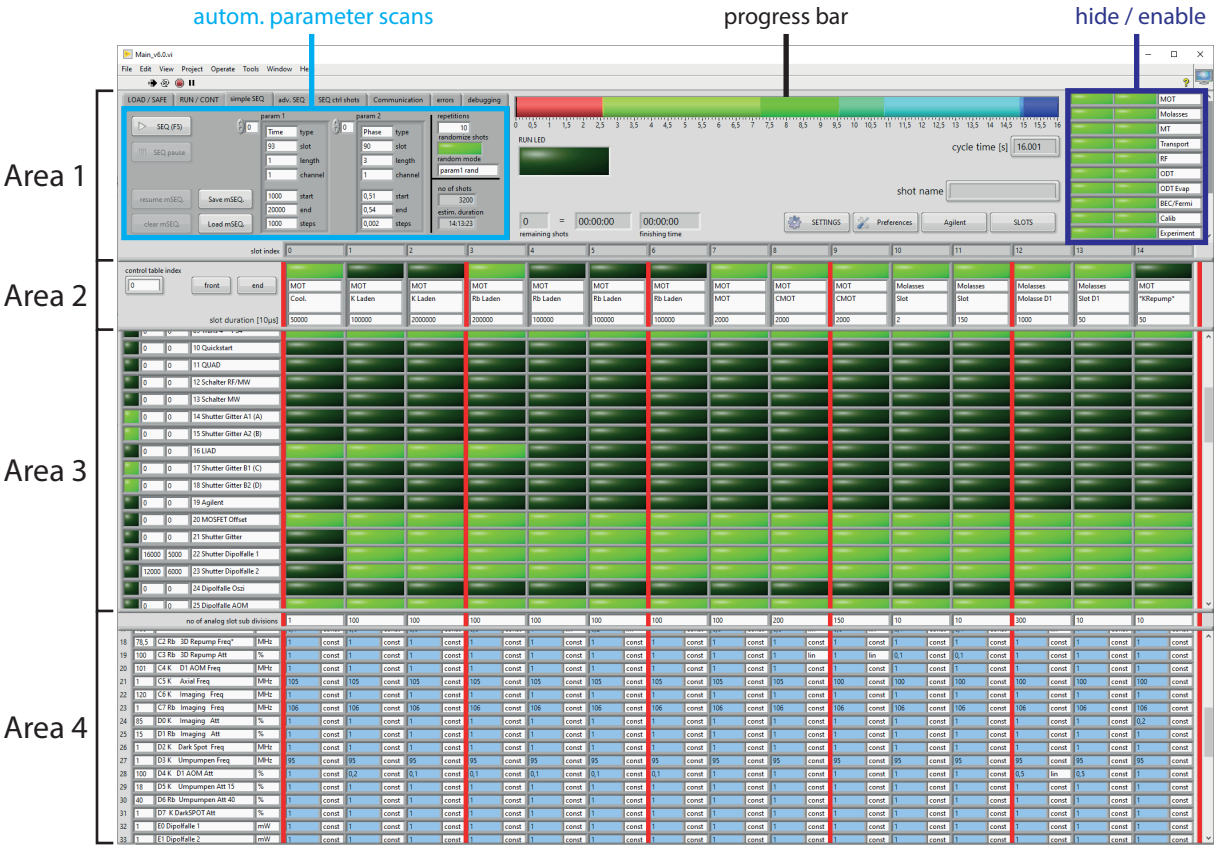

Figure 4.2: **Experiment control software - GUI:**
Area 1*:* general options and execution control. The controls in the light blue box on the left are the 'simple sequence control cluster' and are used to control the automatically executed parameter scans. The dark blue box on the right indicates the controls used for enabling and hiding the different slot types.
Area 2 – 4*:* actual experiment sequence data. Area 2 is used for time slot type definition and setting a slot duration. Area 3 controls the 64 TTL signals and area 4 defines the 40 analogue channels and their ramp types.
The successively executed *time slots* in area 2 – 4 are shown vertically aligned. For operational convenience area 3 – 4 can be scrolled up and down individually, therefore not all parameters are visible in this screenshot.

Another useful feature is the grouping of time slots to logical groups and their simultaneous manipulation (see Figure 4.2, top right). Each *time slot* is assigned to a type, which represents a certain part of the experimental sequence and can be adjusted globally. For instance, to observe the particle number in the MOT, the magnetic transport and subsequent sections of the experiment cycle have to be excluded, which can be done by switching off these entire groups of *time slots*. In addition the visibility of the logical groups of *time slots* can be toggled as a whole, such that only groups are visible that are

relevant to the experiment operator at that moment. This also enhances the responsiveness of the GUI significantly, as less front end elements have to be shown.

internal program design

The strict separation of GUI and internal program data flow in LabVIEW requires a sophisticated application internal communication, as each front end indicator is the internal representation of a variable. In this experimental control software this is realised via multiple simultaneously executed loops, which are designed to handle different tasks and communicate between each other. At its core it is a combination of three loops: the user interface (abbr.: UI) loop, the processing loop and the operation loop. The communication between all loops is realised by sending messages via various queues, which successively dequeue messages from this message queue and act accordingly. The design of these messages follow a simple rule: Each message is comprised of a message specifying enumerator and a variant, which is an abstract LabVIEW representation of any possible data type. Due to this abstraction, this general message structure can be used to transfer any type of data between all types of loops involved.

The *user interface loop* uses an event structure to catch the user interaction with the UI, i.e. button presses or changes in the experiment sequence data. By using such an event structure, the CPU load during idle operation is reduced and no execution takes place, if no user interaction is detected. Using a separate loop for detecting user interaction is useful, as it keeps the experiment control software responsive at any time during runtime and the program is not caught in processing internal loops, during which the UI is not responding. Information and data gathered from the UI is then send to the processing loop via a 'Enqueue element' VI[49], which wraps all relevant information into a single message and inserts the message at the end of the queue. This is important, as it ensures the order of commands given to the UI.

The *processing loop* handles messages created by the UI loop and evaluates which actions have to be performed. A 'Dequeue element' VI is waiting for a message to be queued by the UI loop, dequeues the message, unwraps the transmitted data from the variant and processes it accordingly to the message specifier. All data is then stored in internal variables of the processing loop and displayed on the GUI. Hidden *time slots* are stored in internal variables stored in the processing loop as well. If the experiment sequence is executed, all data is collected and sent to the operation loop.

49 A *virtual instrument* (abbr.: VI) is the basic building block of the visual programming language LabVIEW

The *operation loop* handles the communication with all devices and performs calculations of the experimental sequence data. Unlike both other loops, the operation loop is built as a state-machine and not always waiting for direct commands given by the queue. This allows independent operation of this loop, reacting to possible error messages obtained in the communication with other hardware. In this state-machine setup, the operation loop can enter multiple states, which perform different tasks. In the beginning the state-machine is executing the initialising routine and connects to all devices. Afterwards the loop enters the idle state and waits for commands given by the processing loop. When the processing loop sends an 'Change execution state' message, the operation loop enters a list of sequentially executed states, which perform calculations on the sequence data, apply transfer functions to each analogue channel, insert delays for compensating timing offsets, and calculate ramp patterns between consecutive *time slots*. The last state reads the execution state and returns to the idle case or continues the execution as defined in the beginning of the execution.

One example *single execution* of the experiment sequence can therefore be understood in the following steps.

1. An execution of the experiment sequence is issued by the user via the user interface. The UI loop sends a command to the processing loop.
2. The processing loop gathers information about the current execution state of the sequence. After that, a corresponding 'Change execution state' command is queued in the communication queue for the operation loop. Additionally some UI features are disabled momentarily, for example other execution modes are disabled, during a running execution.
3. If the operation loop is at the end of the execution of a run, or in the idle state, the operation loop is reading queued elements from the processing loop. If the queued message issues an execution state change, the state is altered accordingly. After that, a message is sent back to the processing loop, that the execution was stopped and the UI has to be reset to its initial state.
4. The UI is brought into its normal state and all execution states are enabled again. The UI is now able to start another execution.

Remarks on the implementation of automatic parameter scans: The automatic parameter scans are implemented by writing a program internal data type of a 'sequence change command'. This command contains information about which channel has to be adjusted and which numeric value has to be inserted, overwriting the previously defined value. As

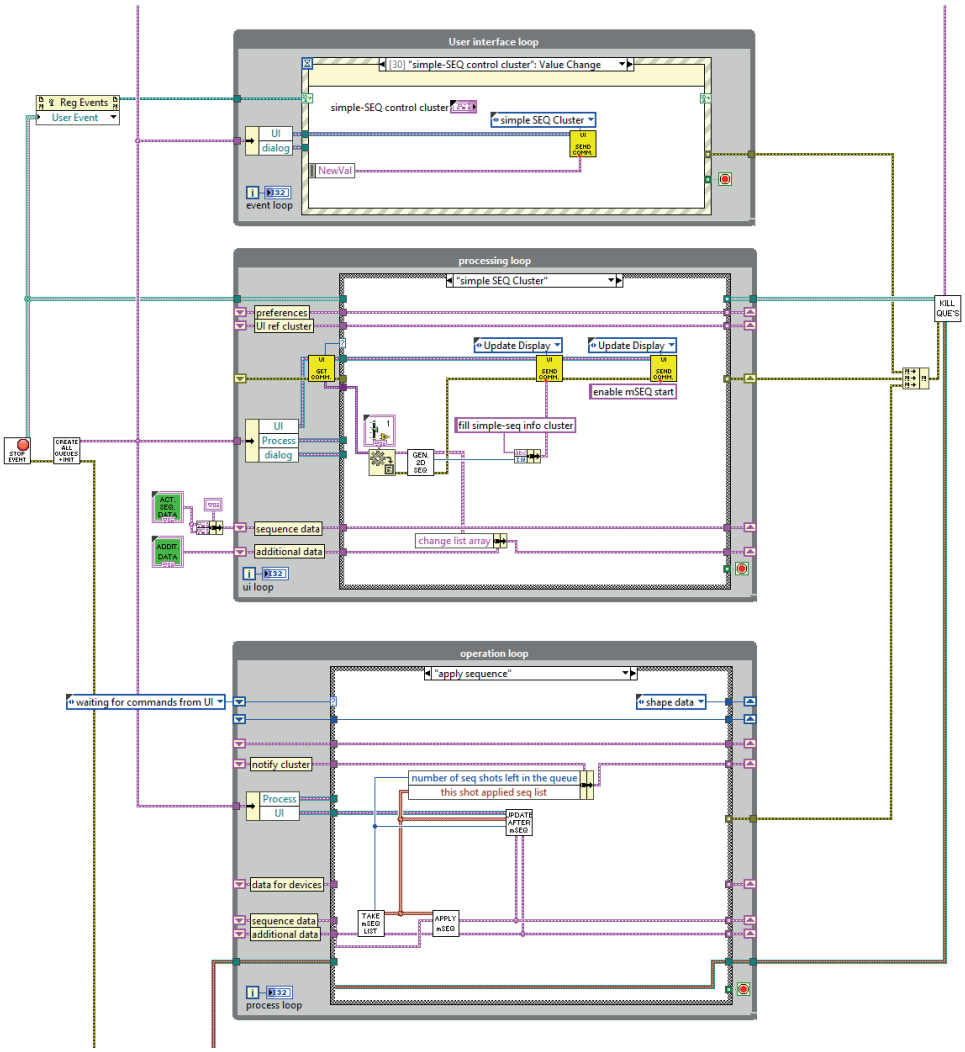

Figure 4.3: **Experiment control software - internals:** exemplary the internal implementation of the parameter scans is shown.
The *UI loop* sends the 'simple SEQ control cluster' (see Figure 4.2) to the processing loop. In the *processing loop* the message gets dequeued (yellow box) and processed, by unwraping the data from the variant, generating a 2D-sequence and creating the set of lists containing 'chance list commands' (see main text for details). The state-machine in the *operation loop* handles the communication with all devices. In the state 'apply sequence' one list of 'sequence change commands' is taken and applied to the control table. Afterwards information about the parameter set executed at that moment is displayed via the processing loop. Additionally, these information are packed into the 'notify cluster' send to the imaging and monitoring program in the following states of the state machine.

an arbitrary number of sequence change commands can be applied to the list of *time slots*, arbitrary high dimensional parameter scans can be performed. Every time the user

is starting a sequential execution the information about the measurement sequence are translated into a set of lists of change commands. During each consecutive execution of the experimental sequence, one list of sequence change commands is taken and removed from the set, applied to the experiment sequence and executed. The top level of implementation for the automatic parameter scans can be seen in Figure 4.3.

The same technique is used to insert automatic control shots scattered in between long automatic parameter scans. For doing so, special sequence change commands are queued, which enable or disable entire groups of slots and remove them temporarily from the sequence control array. This way it is possible to periodically check various quantities, i.e. the atom number prepared in the DFG or BEC. These 'control shots' are automatically separated from the actual measured data sets by the analysis routine and evaluated separately. A not yet implemented idea is to use these control shots during the measurement to adjust the voltages to steer the time phase θ (cf. section 2.1) and compensate for drifts. This can be done by measuring the voltage U_{90° after a defined number of experimental executions and adjust accordingly, such that effectively the set point of the phase stabilisation is tuned automatically.

Implementing a semi-automatic parameter optimisation is planned in the exact same way: A future extension of the program should be able to scan a defined set of parameters automatically in a given physical reasonable range and finds a local optimum. Therefore different possible algorithms might be chosen:

— a *hill climber algorithm* optimising one parameter at a time, choosing the local optimum as a set point and then adjusting other parameters.

— a *simplex algorithm* varying multiple experimental quantities at a time and therefore optimising in a higher dimensional parameter space.

— a *gradient descent algorithm* searching a local maximum by estimating the local gradient against all optimised parameters, then performing a step with all parameters given by the gradient and repeat.

As all three algorithms might show different converging behaviour (if they converge at all) some of the algorithms proposed above might be unfeasible for semi-automatic parameter optimisation. Testing and benchmarking these various options is a subject of future investigation.

communication with other programs

The communication with other programs, namely the imaging and monitoring program, is done via network connection over the DataSocket (abbr.: DS) transfer protocol provided by National Instruments and natively usable within LabVIEW programs. This is done via an so-called DataSocket server, which runs on the sequencer computer and hosts variables, written and read from different LabVIEW programs via a network connection. To reduce the possibility of conflicts during writing and reading these variables, our experiment control software environment uses multiple DataSocket servers at the same time.

1. One 'single write, multiple read' DS server is running on the sequence computer, which provides information about the sequence executed at that moment. All other programs read this 'notify cluster' variable hosted on the DS server on the sequencer computer.
2. Every computer used for imaging and operating cameras hosts its own DS server, hosting variables containing the last picture, time past since the last image was taken, as well as parameters used in the automatic parameter scans. These servers are then queried by programs used for monitoring.

This modular design with multiple DS servers decouples necessary program communication from communication used for convenience and monitoring the experiment. The easy implementation of the DS protocol in every LabVIEW software makes this a well suited solution to easily implement the transfer of different data types over a network connection at a high level, without the need to implement low level routines managing the network traffic. Additionally this solution scales well with the number of programs and routines involved in controlling a typical quantum gas experiment.

4.2 Absorption imaging software with LabVIEW

After the scientific cameras were hardware triggered via a TTL signal, the image data is stored in a camera internal buffer. To handle the read-out procedure a program written in LabVIEW is used to gather the data from the camera after an exposure, collect the corresponding sequence data from the sequencer computer and store everything on a local hard drive. This subsection briefly describes the tasks performed by the *absorption imaging program* and gives an overview of the internal structure of the program.

Like in the case of the experiment control software (see subsection 4.1.2) multiple simultaneously executed loops are used to separate tasks performed by the imaging

program. A pair of UI and processing loop handle the user interaction with the program in the same way it is implemented in the experiment control software. Three loops performing different tasks complement the internal structure of the imaging program. The *camera loop* is handling the communication with the camera, the *communication loop* handles communication with other software used (i.e. the experiment control and monitoring software) and the *quick analysis and save loop* performs immediate analysis and manages the saving of the data sets to the hard drive.

image read-out - *camera loop*

For absorption imaging in our experimental apparatus, the scientific cameras[50] are triggered three times via TTL signal with intermediate read-out handled by the absorption imaging program. With this procedure one absorption image (abbr.: ABS) of the atomic ensemble is taken, one reference image (abbr.: REF) of the corresponding imaging beam and a dark frame (abbr.: DARK) are recorded. As these cameras only contain a single internal buffer to store data, the capture rate of images is limited by the read-out rate of the chip and results in a temporal delay between successive images of 200 ms in our case. To do so, the imaging program repeatedly reads the cameras internal buffer status and initiates the data transfer, once an exposure is finished.

After all three images are received by the imaging program, they are bundled and send to the *quick analysis and save loop*.

collection of sequence data - *communication loop*

The communication loop is reading information from the DS-server running on the sequencer computer and obtains the sequence data at the beginning of the execution. Once this data package is received it is send to the *quick analysis and save loop* and processed.

Choosing this separation of data receiving and image capturing from analysis and saving avoids desynchronisation between sequence data sets and images potentially caused by delays in the analysis and storage procedure. In future an extension of this procedure is planned to automatically detect images, which are unintentionally recorded by the cameras due to an exposure being initiated by switching strong magnetic fields, and separate them from the images intentionally recorded for absorption imaging.

50 pco.pixelfly usb from pco

saving data - *quick analysis and save loop*

The quick analysis and save loop combines experimental sequence data sent by the communication loop, with the three images sent by the camera loop and saves them onto the local hard drive. The saving routine automatically detects the start of a new automatic parameter scan started by the experiment control software and creates a new measurement folder, containing a data folder with the raw data stored. For each individual execution of the experiment sequence one folder inside this data folder is created containing the following files

1. ABS, REF and DARK-image as three individual files in a binary format (as unsigned 16bit integer)
2. experimental sequence data in string representation. These files can be loaded as experimental sequence input for the experiment control software.
3. details of the executed automatic parameter scans. This allows fast access to the relevant automatically varied parameter sets during the analysis.

On the top level measurement folder one comment file is stored, with a description of the measurement. Additionally one file with immediate quick analysis results is stored, which were generated by the imaging program (see below).

immediate quick analysis - *quick analysis and save loop*

The imaging program provides an immediate analysis of the image data by calculating optical densities and derived quantities like particle number and temperature. Therefore multiple fit models for both atomic species are implemented and can be fitted to the 2D column density or integrated 1D line profiles. The histogram of the images is used to determine optimal exposure settings avoiding too low SNR or saturation of the camera pixels. Numerical results directly calculated from the optical densities or obtained by the fit routine are stored in an additional file on the hard drive.

interference fringe patterns in absorption images

Due to mechanical vibrations and slight frequency shifts in the imaging light during the read-out of the ABS-image, interference fringes in the ABS and REF-image might not be aligned and therefore cause problems in the analysis afterwards. Studying the temporal correlation of the fringe patterns on a different experimental setup with similar imaging

technique showed a significant reduction of the correlation between images takes more than 50 ms apart[Bri05, Kro07]. This translates to the fact, that it is beneficial to take the ABS and REF-images in as quick succession as possible. At the moment this is limited by the read-out time of the sensor, which takes ≈180 ms. In order to dramatically improve the imaging quality, a future extension of the imaging program should use the double-shutter mode offered by the cameras used in this experiment, where a pixel shift is used to take two images within 1 ms. Optionally, software side fringe removal algorithms described in section 4.3 can be used to reduce the effect of the interference fringe patterns for measured data sets with the read-out time limited imaging protocol used so far.

4.3 analysis routine and fringe removal algorithms

The analysis routine for absorption images taken in this experimental apparatus consists of several successive steps. As a first step optical column densities are calculated from the absorption images. In a second step it is then possible to determine particle numbers in predefined regions of interest (abbr.: ROI). For this purpose two scripts written in Mathematica[51] are used, which output an analysis report file. This file can be further processed by any other software, in our case Mathematica routines specifically tailored to extract the desired quantities are used to evaluate the data set. The following section summarises tasks performed by the first two analysis scripts.

calculating optical column densities and interference fringe reduction

To extract optical column densities via absorption imaging two images are recorded: the absorption image containing a shadow cast of the atomic cloud being illuminated with a (near-)resonant laser beam, and a reference image without an atomic ensemble placed inside the imaging beam. To determine the dark current of the sensor, which produces an offset in the signal recorded in the absorption and reference image, an additional dark frame is recorded after the reference image. The optical column density n_{OD} is then pixel-wise given by[Erh04, Bri05, KDS99, Kro07]

$$n_{\mathrm{OD}} = -\ln\left(\frac{I_{abs} - I_{dark}}{I_{ref} - I_{dark}}\right) \tag{4.1}$$

where $I_{abs}, I_{ref}, I_{dark}$ denote the intensities recorded in the corresponding images. In the ideal case, the absorption image and reference image capture the same light distribution

51 Mathematica is a computer algebra system developed and maintained by Wolfram Research

(with the exception of the shadow of the atomic cloud) and interference fringes, such that the optical column density obtained via Equation 4.1 is free of interference fringes and show a homogeneous background with a mean optical density of zero. However, in the case of intensity variations of the imaging beam between successive images or a relative shift of the interference patterns this is no longer the case.

The first problem can be compensated quite easily in the case of small image intensity variations on the order of a few percent, by using a ROI for normalisation of the image intensity of the reference image (the ROI for normalisation has to be chosen with care, enclosing a region where no atoms are expected). The effect of skewing the noise pattern is found to be negligible in this case. The second problem is much harder to resolve and requires the usage of a reference image with aligned intensity distributions (with the exception of the shadow of the atomic ensemble), which might not be available. Therefore the first analysis script implements two different methods to calculate the optical densities according to Equation 4.1, which are briefly explained in the following:

1. *the standard method:* the simplest way of calculating the optical densities is given by the direct evaluation of Equation 4.1 and therefore ignoring the likely appearances of interference fringes. In order to reduce background offsets, the signal recorded in the reference image is scaled by the quotient of the mean intensity in the normalisation ROI of the absorption and reference image.

2. *the recovery method:* In order to reduce the effects of interference patterns, it is necessary to use a reference image that has an optimal overlap with the absorption image to be analysed. As this might not be available in the measurement series, its necessary to obtain an optimised reference image by a method presented in [Erh04, Bri05] (further remarks can be found in [Kro07, Bec08]). This recovery method is based on the formation of an orthonormal basis from a selection of all reference images and the subsequent decomposition of the absorption image in this basis. Therefore each reference image is interpreted as a real vector and normalised. Defining a scalar product by the component-wise product of pixel values within the reference ROI allows for the calculation of an orthonormal basis with a previously defined number of basis images/vectors. If the selection of reference images used for this process is optimised by selecting images, which are most orthogonal to the images already selected for the basis, a quite small basis of $\approx$50 reference images is sufficient to reach a quite remarkable reduction of interference fringes obtained in the final image[Bri05]. Example images for both imaging systems used in this experimental apparatus are shown in Figure 4.4.

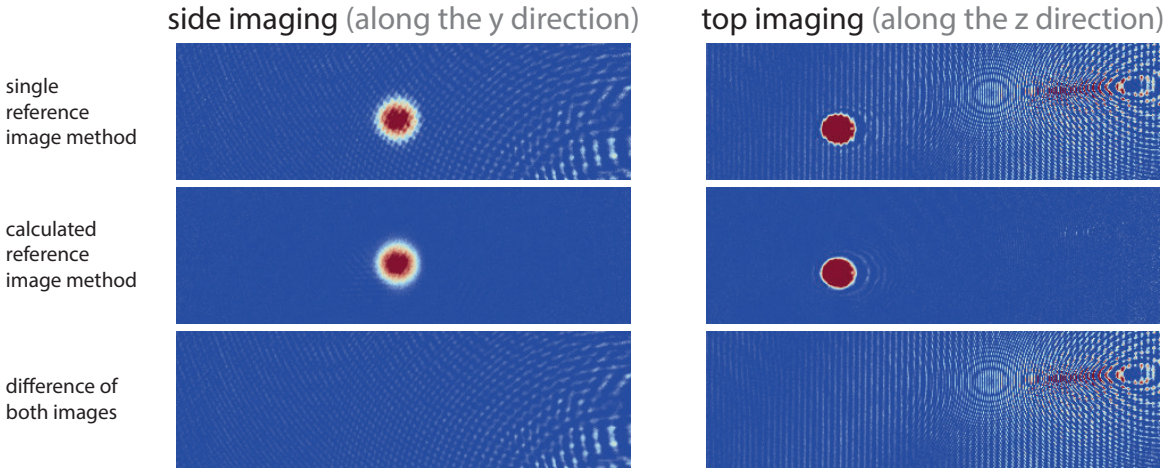

Figure 4.4: **Fringe reduction algorithm examples:** Comparison of both implemented analysis methods to determine optical column densities. Images of the DFG (Left, imaged along the y direction) and the BEC (right, images from the top, along the z direction) are shown. The first row shows results using the standard method to calculate optical densities with a single reference image, while the second row shows results obtained with the recovery method for the same absorption images. The last row shows the difference of the two images above, verifying no visible (nor measurable) recovery artefacts can be observed and only interference fringe patterns are removed. In this example, for each imaging system, a total of 100 reference images were used as a basis for decomposition. Images of the same imaging system are shown using a fixed color scale.

As both of these methods can be subject of potentially unconsidered problems arising in a measurement series, the first analysis script implements either of them and calculates the optical densities with both methods. After the execution of the script, two folders are created, each of which containing one file per absorption image with calculated optical densities stored as binary data (as single-precision floating point numbers in Real32 format).

calculating particle numbers and evaluate ROIs

As recorded optical column densities n_{OD} of atomic clouds depend on the imaging system properties, i.e. the detuning of the imaging light to the imaging transition, the time-of-flight duration and the optical magnification, it is desirable to convert optical densities into independent quantities, like absolute particle numbers. The particle number N in a given ROI obtained by absorption imaging is given by[Erh04, KDS99]

$$N = \frac{A}{\sigma_0} \sum_{\text{pixels} \in \text{ROI}} n_{\mathrm{OD}}, \tag{4.2}$$

where A denotes the imaged area per pixel, σ_0 the resonant scattering cross section and the sum is taken over all pixels within the given ROI. For very high optical column densities ($n_{\mathrm{OD}} > 4$) almost no transmitted light is recorded resulting in a reduced SNR and particle numbers extracted from these images differ from the real particle number by a significant amount[Erh04, Rom09, KDS99]. One way to counteract this problem is to use imaging light with a fixed detuning δ relative to the resonant transition and calculate a corrected particle number N_{corr} using

$$N_{corr} = N \cdot (1 + I/I_{sat}) \cdot (1 + 4(\delta/\Gamma)^2), \tag{4.3}$$

where I and δ are the imaging beam intensity and detuning, and I_{sat} and Γ label the saturation intensity and natural linewidth of the imaging transition.

In order to define the ROIs for the particle number calculation a LabVIEW program is used to conveniently enter an arbitrary number of ROIs, which are then read by the second analysis script. After the first step of calculating the optical column densities for each absorption image as described above, these ROIs are applied to the images and particle numbers for each ROI are calculated and written into a text file. This analysis report file is now readable by any other program, and further analysis can be conducted, including post-selection and averaging of data sets with the same experimental data set, performing statistical analysis and calculating derived quantities like ring contrasts and life times.

4.4 Summary

This chapter presented the control, monitoring and analysis capabilities of the experiment control software used in the experimental apparatus. Specifically the front- and backend of the experiment control software is described in detail and functionalities are explained. Additionally the imaging software and analysis routines used to further analyse the data sets acquired were explained.

The newly developed experiment control software descriped in subsection 4.1.2 is capable of conveniently entering an experimental sequence, handling the corresponding communication with all hardware devices involved and executing the experiment cycle. With the inclusion of multiple features, for instance the automatic multidimensional parameter scans, the software allows for an easy optimisation of experimental parameters and even complex measurement series protocols can be executed automatically.

The absorption imaging program described in section 4.2 handles the readout and control of the scientific cameras, ensures data integrity and manages the automatic organisation of data sets within a measurement series and stores recorded data onto a local harddrive.

Section 4.3 sketches the analysis routine used to evaluate the absorption images and extract particle numbers within user defined ROIs. Additionally an interference fringe removal algorithm is introduced, which dramatically improves the image quality of the absorption images taken.

5 Summary and outlook

Throughout the work of this thesis, upgrades to an existing quantum gas machine have been made to create and subsequently prepare degenerate Fermi gases in higher Bloch bands of an orbital optical lattice. This chapter recaps the main results of the previous chapters in section 5.1 and presents future research perspectives in section 5.2.

5.1 Summary

Creation of a degenerate Fermi gas: The experimental apparatus has been extended to cool potassium-40 atoms to quantum degeneracy. Therefore, upgrades to the laser system have been made, enabling simultaneous laser cooling on the D1- and D2-line. A lambda-enhanced grey molasses scheme has been implemented, which lowered ensemble temperatures before magnetically transporting the sample into the science chamber. After using radio frequency evaporation in a magnetic quadrupole trap, the ensemble is loaded into an optical dipole trap, where sympathetic evaporation of the potassium-40 atoms via heteronuclear collisions with rubidium-87 atoms is utilised to cool both ensembles to quantum degeneracy. The efficiency of this last evaporative cooling step has been greatly improved by the inclusion of a magnetic levitation mechanism that was, to the best of our knowledge, first pioneered during the work on this thesis. After these additions, degenerate Fermi gases of 250×10^3 atoms with temperatures as low as $0.18\,\mathrm{T_F}$ are produced. Richer physics can be explored by adding interactions using two spin component mixtures scattering via s-wave scattering.

Fermions in the orbital optical lattice: A degenerate Fermi gas held in the optical dipole trap can be loaded into the first Bloch band of an optical square lattice by adiabatically increasing the intensity of the superimposed light potential formed by interfering standing waves. Using a technique called *population swapping*, which was up to now only applied to bosonic samples, was successfully applied to Fermions resulting in an efficient population of selected higher Bloch bands of the bipartite

orbital optical square lattice. This method relies on the possibility of experimentally tuning the energy difference of neighbouring lattice sites faster than the tunnelling times. An analysis of the states prepared in the optical lattice is performed with band mapping and time-of-flight imaging, extracting band populations and momentum distributions. The broken rotational symmetry of the momentum distributions directly reveals the orbital character of the states prepared in higher bands, reproducing the results of theoretical predictions based on single-particle band structure calculations remarkably well. During the work on this thesis, degenerate Fermi gases were for the first time loaded into selected higher bands, namely the 2^{nd}, 4^{th} and 7^{th} Bloch band.

Lifetime measurement in the second Bloch band: The lifetime of fermionic samples excited to the second Bloch band has been measured for interacting and non-interacting Fermi gases. Therefore, spin polarised as well as two spin component mixtures have been excited to the second Bloch band and band occupations have been extracted via the band mapping method. A minimal coupled rate equation model has been developed and applied to the experimental data found in both cases, capturing both the behaviour of heating and the collisional induced band index changing processes. The lifetime found for a non-interacting Fermi of 21.2 s exceeds the result for the interacting case by roughly an order of magnitude, where a lifetime of 2.6 s was measured.

Experiment control software: A completely reworked software control environment for controlling the laboratory equipment has been developed, enabling arbitrary dimensional parameter scans for conveniently piloting the apparatus. For this purpose, a LabVIEW based software architecture was employed connecting multiple hardware devices over LAN, which can be easily scaled up, if additional and more complex control flows have to be incorporated. To analyse absorption images, an image defringing algorithm was adapted and implemented, substantially enhancing the image quality while lowering the residual noise to the shot-noise limit. With this addition, even faint optical densities on the order of 0.02 can be detected and reliably used to extract particle numbers.

5.2 Outlook

Despite the progress made throughout this thesis in loading Fermions in higher Bloch bands and observing the orbital degree of freedom, some questions remain open. The following section outlines further interesting research perspectives.

Interaction strength

In order to properly use optical lattices for simulation of various condensed-matter problems, the inter-particle interaction has to be included as an additional tuning knob. If the interaction of Fermi gases can be precisely tuned, it becomes possible to drive the system continuously between the two limiting cases: a BCS-type superfluid or a Bose-Einstein condensate. In case of sufficiently low temperatures and attractive interaction, fermionic atoms can be paired into bound molecular states obeying Bose-Einstein statistics, which has been achieved in 2003[GRJ03]. Studying the behaviour of strongly correlated fermions in higher Bloch bands is of particular interest, as it might allow to examine high-Tc superconductivity observed in cuprates[LNW06].

Tuning the interaction between fermionic particles can be readily done by addressing a Feshbach resonance. In the case of potassium-40 atoms, a common choice is to use a Feshbach resoance between the $|F = 9/2, m_F = -9/2\rangle$ and $|F = 9/2, m_F = -7/2\rangle$ spin component located at $B_0 = 202.1\,\mathrm{G}$, which is easily accessible with reasonable experimental

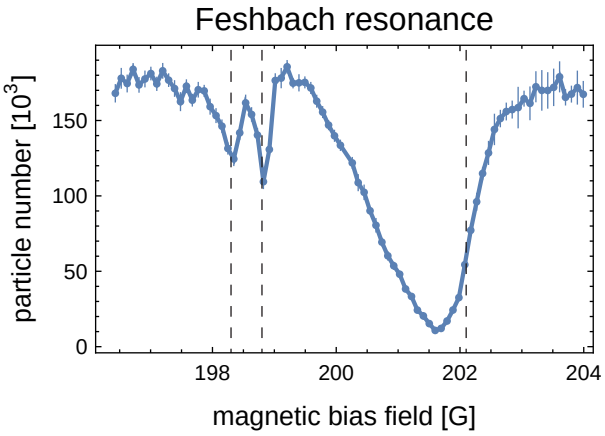

Figure 5.1: **Particle loss in presence of a Feshbach resonance:** The main particle loss due to inelastic three-body collisions is observed at the s-wave Feshbach resonance for $|m_F = -9/2\rangle + |m_F = -7/2\rangle$ scattering located at 202.1 G. Additionally, two loss channels are measured at slightly lower magnetic bias field in good agreement with the positions of p-wave resonances. Dashed lines indicate positions of the Feshbach resonances found in the literature.

effort[RGJ04]. If the initial temperature of the atomic gas is sufficiently low, adiabatically tuning the magnetic bias field across the Feshbach resonance results in the formation of bound molecules[GRJ03]. As this protocol should also be applicable to atoms captured in the optical lattice, possibly also in higher Bloch bands, this offers access to diverse and rich physical questions. As a first step in this direction, all experimental requirements have been met to produce precise and stable magnetic bias fields. In Figure 5.1, the particle number recorded after 2 s hold time in the optical dipole trap is plotted against the magnetic bias field. Here, a pronounced particle loss due to the increased interaction is found for magnetic bias fields around 201.5 G. The slight deviation of the maximal particle loss recorded from the position of the Feshbach resonance is unclear at this point, but does match early measurements of the Feshbach resonance via cross dimensional heating[Lof+02]. Additionally, the p-wave resonance located at 198.8 G[Reg+03] can be clearly resolved as well and is found to be separated into two resonances belonging to different angular momentum components of the scattering problem with l=1[Tic+04].

The next step is to tune the magnetic bias field across the Feshbach resonance such that molecules are formed. If these are observed in the ODT, a clear distinction is made from the fermionic density distribution given by Equation 1.11 and a bimodal density distribution typical of bosons is observed. Subsequently, these molecules can be loaded into the optical lattice and examined.

Effective system dimensionality

The effective dimensionality of the system plays an important role for emulating lattice physics. Creating a 3D optical lattice, fermionic band[Rom09] and Mott insulators[Jör+08] have been observed and studied in the lowest band. Extending this work and incorporate higher Bloch bands is an interesting path, which can be followed in the future.

Another unanswered question is the importance of the weak confinement along the z axis acting as an entropy reservoir for condensation of bosonic samples at the band minimum of the second band. According to the theoretical work in [Nus+20], freezing out the motion along the z direction by adding a third lattice axis should result in a suppression of condensation. As shown in section 3.2, the possibility to store excess energy corresponding to a band transition from the second to the first Bloch band in an excitation along the z direction enables band relaxation. Hence it is suspected, that an additional confinement restricting motion along the z axis suppresses band decay and results in increased lifetimes. Using this approach, an interacting Fermi gas in higher Bloch bands might be stabilised enabling experimental access to even richer physical parameter regimes.

Bibliography

[Abo+01] J. R. Abo-Shaeer et al. "Observation of Vortex Lattices in Bose-Einstein Condensates". In: *Science* 292.5516 (Apr. 2001), pp. 476–479.

[Ada+95] Charles S. Adams et al. "Evaporative Cooling in a Crossed Dipole Trap". In: *Physical Review Letters* 74.18 (May 1995), pp. 3577–3580.

[Aid+11] M. Aidelsburger et al. "Experimental Realization of Strong Effective Magnetic Fields in an Optical Lattice". In: *Physical Review Letters* 107.25 (Dec. 2011), p. 255301.

[Aid+13] M. Aidelsburger et al. "Realization of the Hofstadter Hamiltonian with Ultracold Atoms in Optical Lattices". In: *Physical Review Letters* 111.18 (Oct. 2013), p. 185301.

[Aid+14] M. Aidelsburger et al. "Measuring the Chern number of Hofstadter bands with ultracold bosonic atoms". In: *Nature Physics* 11.2 (Dec. 2014), pp. 162–166.

[And+95] M. H. Anderson et al. "Observation of Bose-Einstein Condensation in a Dilute Atomic Vapor". In: *Science* 269.5221 (July 1995), pp. 198–201.

[Ash76] Neil Ashcroft. *Solid state physics*. New York: Holt, Rinehart and Winston, 1976.

[BDZ08] Immanuel Bloch, Jean Dalibard, and Wilhelm Zwerger. "Many-body physics with ultracold gases". In: *Reviews of Modern Physics* 80.3 (July 2008), pp. 885–964.

[Bec08] Christopf Becker. "Multi component Bose-Einstein condensates". PhD thesis. Universität Hamburg, 2008.

[BF28] M. Born and V. Fock. "Beweis des Adiabatensatzes". In: *Zeitschrift für Physik* 51.3-4 (Mar. 1928), pp. 165–180.

[BHE00] I. Bloch, T. W. Hänsch, and T. Esslinger. "Measurement of the spatial coherence of a trapped Bose gas at the phase transition". In: *Nature* 403.6766 (Jan. 2000), pp. 166–170.

[Bjo+83] G. C. Bjorklund et al. "Frequency modulation (FM) spectroscopy". In: *Applied Physics B Photophysics and Laser Chemistry* 32.3 (Nov. 1983), pp. 145–152.

[Blo05] Immanuel Bloch. "Ultracold quantum gases in optical lattices". In: *Nature Physics* 1.1 (Oct. 2005), pp. 23–30.

[Blo29] Felix Bloch. "Über die Quantenmechanik der Elektronen in Kristallgittern". In: *Zeitschrift für Physik* 52.7-8 (July 1929), pp. 555–600.

[BM21] Albert Benseny and Klaus Mølmer. "Adiabatic theorem revisited: The unexpectedly good performance of adiabatic passage". In: *Physical Review A* 103.6 (June 2021), p. 062215.

[Bri05] Martin Brinkmann. "Optimierung der Detektion und Auswertung von ^{87}Rb-Spinor-Kondensaten". MA thesis. Universität Hamburg, 2005.

[Bru+17] G D Bruce et al. "Sub-Doppler laser cooling of ^{40}K with Raman gray molasses on the D2-line". In: *Journal of Physics B: Atomic, Molecular and Optical Physics* 50.9 (Apr. 2017), p. 095002.

[Büc13] Robert Büchner. "Aufbau einer Magnetfalle für Kalium-40 und Rubidium-87". MA thesis. Universität Hamburg, 2013.

[Büc17] Robert Büchner. "Aufbau einer Apparatur zur Untersuchung ultrakalter Quantengase mit Spin-Freiheitsgrad in höheren Bändern eines optischen Gitters mit zweiatomiger Basis". PhD thesis. Universität Hamburg, 2017.

[Cas06] Yvan Castin. "Basic theory tools for degenerate Fermi gases". In: *Ultra-cold Fermi Gases, M. Inguscio, W. Ketterle, C. Salomon (Ed.) (2007) 289-349* (Dec. 2006).

[Chu+85] Steven Chu et al. "Three-dimensional viscous confinement and cooling of atoms by resonance radiation pressure". In: *Physical Review Letters* 55.1 (July 1985), pp. 48–51.

[Czy07] Gerd Czycholl. *Theoretische Festkörperphysik*. Springer-Verlag GmbH, Dec. 2007. 498 pp.

[Dav+95a] K. B. Davis et al. "Bose-Einstein Condensation in a Gas of Sodium Atoms". In: *Physical Review Letters* 75.22 (Nov. 1995), pp. 3969–3973.

[Dav+95b] Kendall B. Davis et al. “Evaporative Cooling of Sodium Atoms”. In: *Physical Review Letters* 74.26 (June 1995), pp. 5202–5205.

[DC89] J. Dalibard and C. Cohen-Tannoudji. “Laser cooling below the Doppler limit by polarization gradients: simple theoretical models”. In: *Journal of the Optical Society of America B* 6.11 (Nov. 1989), p. 2023.

[DeM+99] B. DeMarco et al. “Measurement of p-wave threshold law using evaporatively cooled fermionic atoms”. In: *Physical Review Letters* 82.21 (May 1999), pp. 4208–4211.

[DeM01] Brian DeMarco. “Quantum Behavior of an Atomic Fermi Gas”. PhD thesis. 2001.

[Den+02] J Hecker Denschlag et al. “A Bose-Einstein condensate in an optical lattice”. In: *Journal of Physics B: Atomic, Molecular and Optical Physics* 35.14 (July 2002), pp. 3095–3110.

[Don+05] E. A. Donley et al. “Double-pass acousto-optic modulator system”. In: *Review of Scientific Instruments* 76.6 (June 2005), p. 063112.

[Dub+12] R. Dubessy et al. “Rubidium-87 Bose-Einstein condensate in an optically plugged quadrupole trap”. In: *Physical Review A* 85.1 (Jan. 2012), p. 013643.

[Dut+15] Omjyoti Dutta et al. “Non-standard Hubbard models in optical lattices: a review”. In: *Reports on Progress in Physics* 78.6 (May 2015), p. 066001.

[Eck17] André Eckardt. “Colloquium: Atomic quantum gases in periodically driven optical lattices”. In: *Reviews of Modern Physics* 89.1 (Mar. 2017), p. 011004.

[Ego+13] M. Egorov et al. “Measurement ofs-wave scattering lengths in a two-component Bose-Einstein condensate”. In: *Physical Review A* 87.5 (May 2013), p. 053614.

[Eic18] Raphael Eichberger. “Ultrakalte Quantengase in höheren Bändern eines optischen Gitters mit präziser Bandstrukturkontrolle”. PhD thesis. Universität Hamburg, 2018.

[Ein25] Albert Einstein. “Quantentheorie des einatomigen idealen Gases”. In: *Sitzungsberichte der preussischen Akademie der Wissenschaften* (Dec. 1925), 1:3–10.

[Erh04] Michael Erhard. “Experimente mit mehrkomponentigen Bose-Einstein-Kondensaten”. PhD thesis. Universität Hamburg, 2004.

[ES07] J.F. Eble and F. Schmidt-Kaler. "Optimization of frequency modulation transfer spectroscopy on the calcium 4^1S_0 to 4^1P_1 transition". In: *Applied Physics B* 88.4 (Aug. 2007), pp. 563–568.

[Eve16] Arne Everbeck. "Aufbau und Charakterisierung eines Zwei-Spezies-Experiments zur Erzeugung ultrakalter Quantengase". PhD thesis. Universität Hamburg, 2016.

[Fer+12] D. Rio Fernandes et al. "Sub-Doppler laser cooling of fermionic ^{40}K atoms in three-dimensional gray optical molasses". In: *EPL (Europhysics Letters)* 100.6 (Dec. 2012), p. 63001.

[Fer+99] Gabriele Ferrari et al. "High-power multiple-frequency narrow-linewidth laser source based on a semiconductor tapered amplifier". In: *Optics Letters* 24.3 (Feb. 1999), p. 151.

[Fis+89] Matthew P. A. Fisher et al. "Boson localization and the superfluid-insulator transition". In: *Physical Review B* 40.1 (July 1989), pp. 546–570.

[Fri+98] S. Friebel et al. "CO2-laser optical lattice with cold rubidium atoms". In: *Physical Review A* 57.1 (Jan. 1998), R20–R23.

[GBZ16] N. Goldman, J. C. Budich, and P. Zoller. "Topological quantum matter with ultracold gases in optical lattices". In: *Nature Physics* 12.7 (June 2016), pp. 639–645.

[Ger+07] T. Gericke et al. "Adiabatic loading of a Bose–Einstein condensate in a 3D optical lattice". In: *Journal of Modern Optics* 54.5 (Mar. 2007), pp. 735–743.

[Ger+08] F. Gerbier et al. "Expansion of a Quantum Gas Released from an Optical Lattice". In: *Physical Review Letters* 101.15 (Oct. 2008), p. 155303.

[Ger18] Fabrice Gerbier. *Quantum gases in optical lattices*. Mar. 2018.

[Gol+04] J. Goldwin et al. "Measurement of the interaction strength in a Bose-Fermi mixture with ^{87}Rb-^{40}K". In: *Physical Review A* 70.2 (Aug. 2004), p. 021601.

[Gol05] Jonathan Michael Goldwin. "Quantum Degeneracy and Interactions in the ^{40}K - ^{87}Rb Bose-Fermi Mixture". PhD thesis. University of Colorado, 2005.

[Goz+93] A. Gozzini et al. "Light-induced ejection of alkali atoms in polysiloxane coated cells". In: *Il Nuovo Cimento D* 15.5 (May 1993), pp. 709–722.

[GPS08] Stefano Giorgini, Lev P. Pitaevskii, and Sandro Stringari. “Theory of ultracold atomic Fermi gases”. In: *Reviews of Modern Physics* 80.4 (Oct. 2008), pp. 1215–1274.

[Gre+01] Markus Greiner et al. “Exploring Phase Coherence in a 2D Lattice of Bose-Einstein Condensates”. In: *Physical Review Letters* 87.16 (Oct. 2001), p. 160405.

[Gre+02] Markus Greiner et al. “Quantum phase transition from a superfluid to a Mott insulator in a gas of ultracold atoms”. In: *Nature* 415.6867 (Jan. 2002), pp. 39–44.

[Gri+13] Andrew T. Grier et al. “Λ-enhanced sub-Doppler cooling of lithium atoms in D_1 gray molasses”. In: *Phys. Rev. A* 87.6 (June 2013), p. 063411.

[GRJ03] Markus Greiner, Cindy A. Regal, and Deborah S. Jin. “Emergence of a molecular Bose–Einstein condensate from a Fermi gas”. In: *Nature* 426.6966 (Nov. 2003), pp. 537–540.

[GWO99] Rudolf Grimm, Matthias Weidemüller, and Yurii B. Ovchinnikov. “Optical dipole traps for neutral atoms”. In: *Advances in Atomic, Molecular and Optical Physics Vol. 42, 95-170 (2000)* (Feb. 1999).

[Hac+21] M. Hachmann et al. “Quantum Degenerate Fermi Gas in an Orbital Optical Lattice”. In: *Physical Review Letters* 127.3 (July 2021), p. 033201.

[Hac17] Max Hachmann. “Aufbau eines Lasersystems zum Kühlen von Kalium-40 auf dem D1-Übergang”. MA thesis. Universität Hamburg, 2017.

[Hän11] Sylvi Händel. “Experiments on ultracold quantum gases of ^{85}Rb and ^{87}Rb”. PhD thesis. Durham University, 2011.

[Hes86] Harald F. Hess. “Evaporative cooling of magnetically trapped and compressed spin-polarized hydrogen”. In: *Physical Review B* 34.5 (Sept. 1986), pp. 3476–3479.

[HH06] Dirk Hansen and Andreas Hemmerich. “Observation of Multichannel Collisions of Cold Metastable Calcium Atoms”. In: *Physical Review Letters* 96.7 (Feb. 2006), p. 073003.

[HH93] A. Hemmerich and T. W. Hänsch. “Two-dimesional atomic crystal bound by light”. In: *Physical Review Letters* 70.4 (Jan. 1993), pp. 410–413.

[HS75] T.W. Hänsch and A.L. Schawlow. “Cooling of gases by laser radiation”. In: *Optics Communications* 13.1 (Jan. 1975), pp. 68–69.

[Jak+98] D. Jaksch et al. “Cold Bosonic Atoms in Optical Lattices”. In: *Physical Review Letters* 81.15 (Oct. 1998), pp. 3108–3111.

[Jer14] Dylan Jervis. “A Fermi Gas Microscope Apparatus”. PhD thesis. University of Toronto, 2014.

[Jin+21] Shengjie Jin et al. “Evidence of Potts-Nematic Superfluidity in a Hexagonal sp2 Optical Lattice”. In: *Physical Review Letters* 126.3 (Jan. 2021), p. 035301.

[Jör+08] Robert Jördens et al. “A Mott insulator of fermionic atoms in an optical lattice”. In: *Nature* 455.7210 (Sept. 2008), pp. 204–207.

[Jot+14] Gregor Jotzu et al. “Experimental realization of the topological Haldane model with ultracold fermions”. In: *Nature* 515.7526 (Nov. 2014), pp. 237–240.

[KDS99] W. Ketterle, D. S. Durfee, and D. M. Stamper-Kurn. “Making, probing and understanding Bose-Einstein condensates”. In: (Apr. 1999).

[Kit04] Charles Kittel. *Introduction to Solid State Physics*. WILEY, Nov. 2004. 680 pp.

[Kle+06] C. Klempt et al. “Ultraviolet light-induced atom desorption for large rubidium and potassium magneto-optical traps”. In: *Physical Review A* 73.1 (Jan. 2006), p. 013410.

[KM10] Joern N. Kupferschmidt and Erich J. Mueller. “Role of interactions in time-of-flight expansion of atomic clouds from optical lattices”. In: *Physical Review A* 82.2 (Aug. 2010), p. 023618.

[Koc+16] T Kock et al. “Orbital optical lattices with bosons”. In: *Journal of Physics B: Atomic, Molecular and Optical Physics* 49.4 (Jan. 2016), p. 042001.

[Köh+05] Michael Köhl et al. “Fermionic Atoms in a Three Dimensional Optical Lattice: Observing Fermi Surfaces, Dynamics, and Interactions”. In: *Physical Review Letters* 94.8 (Mar. 2005), p. 080403.

[Kro07] Jochen Kronjäger. “Coherent Dynamics of Spinor Bose-Einstein Condensates”. PhD thesis. Universität Hamburg, 2007.

[KZ08] Wolfgang Ketterle and Martin W. Zwierlein. “Making, probing and understanding ultracold Fermi gases”. In: (Jan. 2008).

[Let+88] Paul D. Lett et al. “Observation of Atoms Laser Cooled below the Doppler Limit”. In: *Physical Review Letters* 61.2 (July 1988), pp. 169–172.

[Li+18] Yongqiang Li et al. “Rotation-Symmetry-Enforced Coupling of Spin and Angular Momentum for p -Orbital Bosons”. In: *Physical Review Letters* 121.9 (Aug. 2018), p. 093401.

[LL15] Xiaopeng Li and W. Vincent Liu. “Physics of higher orbital bands in optical lattices: a review”. In: *Rep. Prog. Phys. 79 (2016) 116401* (Aug. 2015).

[LNW06] Patrick A. Lee, Naoto Nagaosa, and Xiao-Gang Wen. “Doping a Mott insulator: Physics of high-temperature superconductivity”. In: *Reviews of Modern Physics* 78.1 (Jan. 2006), pp. 17–85.

[Lof+02] T. Loftus et al. “Resonant Control of Elastic Collisions in an Optically Trapped Fermi Gas of Atoms”. In: *Physical Review Letters* 88.17 (Apr. 2002), p. 173201.

[Mad+00] K. W. Madison et al. “Vortex Formation in a Stirred Bose-Einstein Condensate”. In: *Physical Review Letters* 84.5 (Jan. 2000), pp. 806–809.

[Mat+99] M. R. Matthews et al. “Vortices in a Bose-Einstein Condensate”. In: *Physical Review Letters* 83.13 (Sept. 1999), pp. 2498–2501.

[Met99] Harold Metcalf. *Laser cooling and trapping*. New York: Springer, 1999.

[Mig+85] Alan L. Migdall et al. “First Observation of Magnetically Trapped Neutral Atoms”. In: *Physical Review Letters* 54.24 (June 1985), pp. 2596–2599.

[ML12] Jani-Petri Martikainen and Jonas Larson. “Multiorbital bosons in bipartite optical lattices”. In: *Physical Review A* 86.2 (Aug. 2012), p. 023611.

[MLF18] Zhi-Xin Meng, Yu-Hang Li, and Yan-Ying Feng. “Two-frequency amplification in a semiconductor tapered amplifier for cold atom experiments”. In: *Chinese Physics B* 27.9 (Sept. 2018), p. 094201.

[Mod+03] M. Modugno et al. “Mean-field analysis of the stability of a K-Rb Fermi-Bose mixture”. In: *Physical Review A* 68.4 (Oct. 2003), p. 043626.

[Mod+99] G. Modugno et al. “Sub-Doppler laser cooling of fermionic ^{40}K atoms”. In: *Physical Review A* 60.5 (Nov. 1999), R3373–R3376.

[Nus+20] M. Nuske et al. “Metastable order protected by destructive many-body interference”. In: *Physical Review Research* 2.4 (Nov. 2020), p. 043210.

[Öls+13] M Ölschläger et al. “Interaction-induced chiral $p_x \pm ip_y$ superfluid order of bosons in an optical lattice”. In: *New Journal of Physics* 15.8 (Aug. 2013), p. 083041.

[Öls13] Matthias Ölschläger. "Ultrakalte Quantengase in höheren Bloch-Bändern optischer Gitterpotentiale". PhD thesis. Universität Hamburg, 2013.

[Ono17] Roberto Onofrio. "Cooling and thermometry of atomic Fermi gases". In: *Physics Uspekhi 59 (2016) 1129 [Uspekhi Fizicheskikh Nauk 186 (2016) 1229]* (Oct. 2017).

[Osp+06] C. Ospelkaus et al. "Interaction-Driven Dynamics of ^{40}K-^{87}Rb Fermion-Boson Gas Mixtures in the Large-Particle-Number Limit". In: *Physical Review Letters* 96.2 (Jan. 2006), p. 020401.

[ÖWH11] Matthias Ölschläger, Georg Wirth, and Andreas Hemmerich. "Unconventional superfluid order in the F Band of a bipartite optical square lattice". In: *Physical Review Letters* 106.1 (Jan. 2011), p. 015302.

[Pau40] W. Pauli. "The Connection Between Spin and Statistics". In: *Phys. Rev.* 58 (8 Oct. 1940), pp. 716–722.

[Per19] Hélène Perrin. *Optical lattices*. Oct. 2019.

[PS08] C. J. Pethick and H. Smith. *Bose–Einstein Condensation in Dilute Gases*. Cambridge University Press, 2008.

[PT13] Saurabh Paul and Eite Tiesinga. "Formation and decay of Bose-Einstein condensates in an excited band of a double-well optical lattice". In: *Physical Review A* 88.3 (Sept. 2013), p. 033615.

[Reg+03] C. A. Regal et al. "Tuning p-Wave Interactions in an Ultracold Fermi Gas of Atoms". In: *Physical Review Letters* 90.5 (Feb. 2003), p. 053201.

[Reg05] Cindy Regal. "Experimental realization of BCS-BEC crossover physics with a Fermi gas of atoms". PhD thesis. University of Colorado, 2005.

[RGJ04] C. A. Regal, M. Greiner, and D. S. Jin. "Lifetime of Molecule-Atom Mixtures near a Feshbach Resonance in ^{40}K". In: *Physical Review Letters* 92.8 (Feb. 2004), p. 083201.

[Rie21] Jasper Riebesehl. "Hyperfine spin state preparation of ultracold ^{87}Rb and ^{40}K atoms with radio-frequency techniques". MA thesis. Universität Hamburg, 2021.

[Roa+02] G. Roati et al. "Fermi-Bose Quantum Degenerate ^{40}K-^{87}Rb Mixture with Attractive Interaction". In: *Physical Review Letters* 89.15 (Sept. 2002), p. 150403.

[Roc20] Jose Antonio Vargas Roco. “Non-equilibrium dynamics of ultracold quantum gases in higher bands of an optical lattice”. PhD thesis. Universität Hamburg, 2020.

[Rom09] Tim Rom. “Bosonische und fermionische Quantengase in dreidimensionalen optischen Gittern”. de. PhD thesis. 2009.

[Ros+17] Sara Rosi et al. “Λ-enhanced grey molasses on the D_2 transition of Rubidium-87 atoms”. In: *Scientific Reports 8, (2018) 1031* (Sept. 2017).

[Sad+00] H R Sadeghpour et al. “Collisions near threshold in atomic and molecular physics”. In: *Journal of Physics B: Atomic, Molecular and Optical Physics* 33.5 (Feb. 2000), R93–R140.

[Sie+15] Franz Sievers et al. “Simultaneous sub-Doppler laser cooling of fermionic ^6Li and ^{40}K on the D_1 line: Theory and experiment”. In: *Physical Review A* 91.2 (Feb. 2015), p. 023426.

[Slo+19] M. R. Slot et al. “p -Band Engineering in Artificial Electronic Lattices”. In: *Physical Review X* 9.1 (Jan. 2019), p. 011009.

[Str+11] J. Struck et al. “Quantum Simulation of Frustrated Classical Magnetism in Triangular Optical Lattices”. In: *Science* 333.6045 (Aug. 2011), pp. 996–999.

[Str+12] J. Struck et al. “Tunable Gauge Potential for Neutral and Spinless Particles in Driven Optical Lattices”. In: *Physical Review Letters* 108.22 (May 2012), p. 225304.

[Str+13] J. Struck et al. “Engineering Ising-XY spin-models in a triangular lattice using tunable artificial gauge fields”. In: *Nature Physics* 9.11 (Sept. 2013), pp. 738–743.

[Tar15] Matthias Tarnowski. “Implementation and characterization of a gray molasses and of tunable hexagonal optical lattices for ^{40}K”. In: (2015).

[Tic+04] C. Ticknor et al. “Multiplet structure of Feshbach resonances in nonzero partial waves”. In: *Physical Review A* 69.4 (Apr. 2004), p. 042712.

[TS18] Leticia Tarruell and Laurent Sanchez-Palencia. “Quantum simulation of the Hubbard model with ultracold fermions in optical lattices”. In: *Comptes Rendus Physique* 19.6 (Sept. 2018), pp. 365–393.

[Wal96] Joannes Theodorus Maria Walraven. “Atomic hydrogen in magnetostatio traps”. In: *Quantum dynamics of simple systems*. G-L Oppo, SM Barnett,E Riis, and M Wilkinson, 1996.

[Wan+21] Xiao-Qiong Wang et al. "Evidence for an atomic chiral superfluid with topological excitations". In: *Nature* 596.7871 (Aug. 2021), pp. 227–231.

[Wei+99] John Weiner et al. "Experiments and theory in cold and ultracold collisions". In: *Reviews of Modern Physics* 71.1 (Jan. 1999), pp. 1–85.

[Wie19] Phillip Wieburg. "A Novel Fermionic Quantum Gas Microscope: Concept, Design and Construction". In: (Jan. 2019).

[Win13] Hannes Winter. "Aufbau eines Lasersystems zur Präparation ultrakalter Kaliumatome". MA thesis. Universität Hamburg, 2013.

[Wir13] Georg Wirth. "Orbital superfluidity in excited bands of an optical lattice". PhD thesis. Universität Hamburg, 2013.

[WÖH10] Georg Wirth, Matthias Ölschläger, and Andreas Hemmerich. "Evidence for orbital superfluidity in the P-band of a bipartite optical square lattice". In: *Nature Physics* 7.2 (Dec. 2010), pp. 147–153.

[WS21] Christof Weitenberg and Juliette Simonet. "Tailoring quantum gases by Floquet engineering". In: *Nature Physics* 17.12 (Aug. 2021), pp. 1342–1348.

[Zho+18] Tianwei Zhou et al. "High precision calibration of optical lattice depth based on multiple pulses Kapitza-Dirac diffraction". In: *Optics Express* 26.13 (June 2018), p. 16726.

[Zwi+05] M. W. Zwierlein et al. "Vortices and superfluidity in a strongly interacting Fermi gas". In: *Nature* 435.7045 (June 2005), pp. 1047–1051.

[ZZL15] Zhenyu Zhou, Erhai Zhao, and W. Vincent Liu. "Spin-Orbital Exchange of Strongly Interacting Fermions in the p-Band of a Two-Dimensional Optical Lattice". In: *Physical Review Letters* 114.10 (Mar. 2015), p. 100406.

List of Figures

List of abbreviations

Abbreviation	Full name
BEC	Bose-Einstein condensate
BZ	Brillouin zone
DFG	degenerate Fermi gas
DS	DataSocket (Labview programming)
ECDL	external-cavity diode laser
FD	Fermi-Dirac
GUI	graphical user interface
IGBT	insulated-gate bipolar transistor
IO	input-output
MOPA	master-oscillator power amplifier
MOSFET	metal-oxide-semiconductor field-effect transistor
MOT	magneto-optical trap
MQT	magnetic quadrupole trap
OD	optical density
ODT	optical dipole trap
PSD	phase space density
RF	radio-frequency
RAP	rapid adiabatic passage
ROI	region of interest
SNR	signal-to-noise ratio
TA	tapered amplifier
TOF	Time-of-flight
UHV	ultra-high vacuum
UI	user interface
VI	virtual instrument (LabVIEW programming)

Table 5.1: List of abbreviations used throughout this thesis

Acknowledgements

At the end of a project, one always looks back on dear companions who have played a significant role in its success. I would like to take this opportunity to thank them!

First and foremost I would like to thank Andreas Hemmerich. Reducing his contribution to the role of being the supervisor of my doctoral thesis would not do justice to his part in its success, as I have seen him much more like a mentor. His approach to discuss and dissect physical questions into smaller pieces, think about toy models and combine microscopic, mesoscopic and macroscopic aspects into one consistent image has been very instructional and has shaped my way of thinking about problems not only related to physics. I am eager to continue to return the favour by giving *expert advice in mathematica* questions.

Additionally I want to thank Henning Moritz for being the second reviewer of this thesis. Further, I want to thank the review committee of my disputation, namely Prof. Dr. Ludwig Mathey, Prof. Dr. Daniela Pfannkuche and Dr. Juliette Simonet.

Working on an experimental machine, developing new ideas, carrying out long measuring shifts and running into the laboratory in the middle of the night in case of a critical failure is not a one-man-operation. A very special thanks therefore goes to my dear colleagues who have suffered, rejoiced, endured and celebrated successes with me over the past years. First of all, I would like to thank Yann Kiefer for all the funny moments we shared together. The dedication to experimentation and the desire to develop good and solid solutions has often united us both by complementing each other's skills. Last but not least, our common passion for chess has brought us together as friends and I thank you for gently pushing me across the finish line. Following in the footsteps of the two postdocs Raphael Eichberger and Robert Büchner with all their experimental experience has taught me a lot and I have been able to take a lot away from the mistakes and successes you have made. Jasper Riebesehl, thank you for the wonderful time in the lab.

A research group does not only consist of the supervisor and the experiment team, but there are so many more people to thank. Discussions in lunch breaks, social activities and coffee breaks brought me closer to you all and I am grateful for this time. Hans, with his open ear for all kinds of issues, has become a central part of the research group for me. I thank Jose for fruitful discussions. I would also like to thank the Calcium team consisting of Hannes, Torben and David, as well as the Cavity team around Christoph and Popla.

Besides the work in the lab, working on a doctoral thesis can also be mentally and physically exhausting. I would like to take this opportunity to thank my dear friends Lena, Torben, Jakob and Marius. I have always been able to rely on you over the years. Whether you have ensured my physical well-being by spending evenings together, have stopped me at the right moments to pause and ponder, or have simply offered joy and distraction; I have always been able to rely on you! In particular, I would like to mention your psychological support, which has contributed significantly and played a major role in the completion of this work. If it weren't for you, I probably wouldn't have made it.

The journey of writing a doctoral thesis does not begin in a laboratory, but often much earlier. My parents, Sylvia and Gerd, also deserve special thanks at this point. You encouraged my curiosity and enthusiasm for sciences from an early age and never lost sight of my creative streak as well. Throughout the duration of my studies, you have had my back in every conceivable way and I thank you for your patience and perseverance. I thank my sister Hannah for all the wonderful moments, for the brotherly banter and the conversations that bring us closer together every time.

A very special thank you also goes to those who remain hidden here. To those who are simply the way they are and thus support me incredibly. With what you are for me and what you mean to me, you give me new energy and joy every day. You have played a decisive role in this success.

Eidesstattliche Versicherung / Declaration on oath

Hiermit versichere ich an Eides statt, die vorliegende Dissertationsschrift selbst verfasst und keine anderen als die angegebenen Hilfsmittel und Quellen benutzt zu haben.
Die eingereichte schriftliche Fassung entspricht der elektronisch eingereichten.
Die Dissertation wurde in der vorgelegten oder einer ähnlichen Form nicht schon einmal in einem früheren Promotionsverfahren angenommen oder als ungenügend beurteilt.

I hereby declare upon oath that I have written the present dissertation independently and have not used further resources and aids that those stated.
The submitted printed version corresponds to the digital version.
The presented dissertation has not been submitted in this or a similar form and was not accepted in a previous doctoral procedure or judged to be insufficient.

Hamburg, 11.04.2022 _____

Max Hachmann